

**Thermomechanical Properties and Performance of
Microfabricated Solid Oxide Fuel Cell (μ SOFC)
Structures**

by

Namiko Yamamoto

Submitted to the Department of Aeronautics and Astronautics
in partial fulfillment of the requirements for the degree of

Master of Science in Aeronautics and Astronautics

at the

MASSACHUSETTS INSTITUTE OF TECHNOLOGY

September 2006

© Massachusetts Institute of Technology 2006. All rights reserved.

Author

Department of Aeronautics and Astronautics

August 25, 2006

Certified by

Brian L. Wardle

Boeing Assistant Professor of Aeronautics and Astronautics

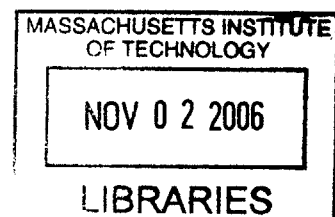
Thesis Supervisor

Accepted by

Jaime Peraire

Chairman, Department Committee on Graduate Students

AERO



Thermomechanical Properties and Performance of Microfabricated Solid Oxide Fuel Cell (μ SOFC) Structures

by

Namiko Yamamoto

Submitted to the Department of Aeronautics and Astronautics
on August 25, 2006, in partial fulfillment of the
requirements for the degree of
Master of Science in Aeronautics and Astronautics

Abstract

The mechanical properties of a ceramic electrolyte, sputtered yttria-stabilized zirconia (YSZ), in thin film ($<1\mu\text{m}$) form were studied in order to design and fabricate thermomechanically stable microfabricated SOFCs (μ SOFCs) at high operation temperature. YSZ films of 70–600nm thickness were deposited at either room temperature or high temperature (500/600°C) on substrates of either silicon, or silicon nitride. The residual film stresses varied from -700 to -100MPa as-deposited, and exhibited tensile hysteresis reaching stresses of -300 to $+400\text{MPa}$ with post-deposition annealing to 500°C. Mechanisms controlling the residual stress trends include tensile stress evolution with grain growth and compressive stresses due to "atomic peening". Young's modulus was obtained by center deflection measurement of square membranes for films in mild compression, and from bulge tests for films in tension. The modulus (24–105GPa) was found to be highly dependent on deposition conditions, and was less than half the bulk value (200GPa). Meanwhile, CTEs ($\sim 10.5 \times 10^{-6}/^\circ\text{C}$) extracted from wafer curvature measurement during thermal cycling were independent of deposition conditions. Based on these properties, maximum in-plane stresses in the films were assessed with nonlinear plate theory, and used for μ SOFC design. Tri-layer (Pt-YSZ/YSZ/Pt-YSZ) membranes designed in this way for operation in the post-buckling regime were fabricated with sidelengths up to 200 μm and with total thickness of 450nm. These large-area membranes buckled, but were structurally viable during repeated thermocycles to 625°C. These devices functioned and produced power of $\sim 0.1\text{mW}/\text{cm}^2$ at 500°C, less than estimated ($0.25\text{W}/\text{cm}^2$) due to lack/leakage of gases and other test set-up issues. This work experimentally verified the post-buckling design regime for functional electrolyte-supported μ SOFCs. Future work includes refinement of thermomechanical property characterization, optimal design of other μ SOFC systems, and controlled testing of μ SOFCs.

Thesis Supervisor: Brian L. Wardle

Title: Boeing Assistant Professor of Aeronautics and Astronautics

Acknowledgments

I could not have been completed this thesis work, my first actual research work, without generous support from all the people around me who constantly encouraged and enlightened me with their great knowledge and personalities. The first person I mention is, of course, Professor Brian Wardle, my advisor who guided me through this work ranging in the vast area with his great insights and cheerful encouragement. I am so lucky to have Brian as an adviser. I also greatly thank the other PIs in the MURI project, Professor Klavs Jensen, Prof. Martin Schmidt, and Prof. Harry Tuller, and the MURI project teammates, especially David Quinn, Dr. Nathaniel Wicks, Jianyi Cui, Joshua Hertz, Dr. Ole Nielsen, and Dr. Kishori Deshpande for their patience and support. Their guidance was essential for me to jump in the projects that initiated four years ago. I truly enjoyed the opportunity to work and share thoughts with them. All the lab work was not possible without the generous help by John Kane from TELAMS, and by all the MTL staffs, especially Kurt Broderick. I appreciate much the help from Dr. Yong Xiang, Han Li, and Professor Joost Vlassak for kindly letting me use their bulge test facility. I also would like to thank the graduate students of Prof. Tuller group who encouraged me a lot when I spent much time in the the sputtering machine room. Dilan Seneviratne and Dr. Woosik Kim were the best teachers to consult about the processes and the best company. Thank you so much for being there for me when I broke my hand bone.

As for more personal side, I could not have survived some challenging days without my TELAMS people. I thank Professor Paul Lagace to guide us always in the right work ethics direction in the high level. I greatly appreciate all the labmates and the Professor Raul Radovitzky's group students who share the hidden pent house office in building 41. Occasional spitball fights that we had to have in the office were such great breaks on one of those bad days. Japanese Association was and will be a big part of my social life at MIT grad school. I thank all the officers, especially Satoshi Takahashi for sharing the precious enjoyable time and more. I also thank the friends I have always shared the best time, who are sadly now away from MIT,

Jenny Lee, Christine Yang, Ram Woo, and Ian Bliss. The great memories and basic survival abilities at MIT that I acquired together with them, are my bare bones to keep my passion and motivation towards my life goal. I also thank my best friends and teachers from Oin high school, Yoko Yamada, Noriko Iwai, Ms. Setsuko Okusa, President Keiko Zen, who are like my sisters and mothers in our proud girls' school, for their significant existence in my heart. I should never forget about Mary Thompson and Harold Weintraub, for being my "mom and dad" in Boston and for their best care over the past six years. Finally I want to mention two most important people that I met at MIT grad school. I cannot thank too much Yoshiaki Kuwata for his constant technical and mental support. With the role model like him who share the same passions in Aero/Astro, I can keep moving. I also greatly appreciate Ryu Yoshida for being my best friend at all the time.

Finally, everything, the opportunity to start research, to meet all the great people I mentioned above, and to at all come to MIT, was not possible without my family: Mama, Papa, and my sister, Akiko. Thank you very much for your constant encouragement, understanding, and love.

Contents

1	Introduction and Motivation	19
1.1	Motivation for Microfabricated SOFCs (μ SOFCs)	19
1.2	Motivation of Thesis Work	22
1.3	Objectives and Scope of Thesis	23
2	Background and Prior Work	27
2.1	Material Property Characterization of Thin Film Materials	27
2.2	Mechanical characterization of YSZ Thin Membranes	30
2.2.1	Microstructure of Thin Films	30
2.2.2	Residual Stress of YSZ Sputter-Deposited Thin Films	34
2.2.3	Coefficient of Thermal Expansion and Biaxial Modulus of YSZ Thin Films	39
2.3	Prior Work on Achieving μ SOFCs	40
3	Thin Film Fabrication	45
3.1	Sputtering	45
3.1.1	Sputtering Mechanism	46
3.1.2	Sputtering Deposition Apparatus and Conditions	47
3.2	Microfabrication of Free-Standing Thin Membranes	50
4	Mechanical Property Characterization of a μSOFC Electrolyte	59
4.1	Overview of Characterization Procedure	59
4.2	Residual Stress by Wafer Curvature Measurement	62

4.2.1	Theory and Experimental Procedures	62
4.2.2	Results and Discussion	66
4.3	Modulus-CTE Product Extraction by Wafer Annealing	69
4.3.1	Experimental Procedures	69
4.3.2	Results and Discussion	70
4.4	Modulus Extraction by Square Membrane Buckling of Compressive Membranes	73
4.4.1	Theoretical Background	74
4.4.2	Experimental Procedures	76
4.4.3	Results and Discussion	80
4.4.4	Implications for Design of Thermally Stable Thin Membranes	84
4.5	Young's Modulus Extraction by Bulge Test on Tensile Membranes . .	87
4.5.1	Theoretical Background	88
4.5.2	Sample Fabrication and Experimental Procedures	89
4.5.3	Results and Discussion	90
4.6	Comparison of Measured YSZ Material Properties	91
4.7	Conclusions	92
5	μSOFC Device Fabrication and Testing	117
5.1	Design and Fabrication of Fuel Cell Device	117
5.1.1	Structural Design	118
5.1.2	Fabrication	120
5.1.3	Statistical Characterization of Electrical Shorting of Power Test Samples	122
5.2	Membrane Stress Evolution under Thermocycling	123
5.3	Power Test	126
5.3.1	Test Setup and Calibration	126
5.3.2	Results	130
5.3.3	Conclusions	131

6	Conclusions and Recommendations for Future Work	149
6.1	Summary of Results and Contributions	149
6.2	Implications	155
6.3	Recommendations for Future Work	156

List of Figures

1-1	Electrochemical reaction of solid oxide fuel cells.	25
1-2	Failure modes of thin membranes, from [1].	26
2-1	Film deposition mechanism of sputtered polycrystalline films: side and top views of grain growth, from [2].	42
2-2	Microstructure types determined by deposition conditions, after [2].	43
2-3	Crystalline structure of zirconia with lattice sites occupied by the cations (Zr, Y).	44
3-1	Angular emission distributions for sputtered atoms with different energies, from [1] after [3].	53
3-2	Schematic view (side and top) of Kurt J. Lesker sputtering system, modified from [1].	54
3-3	Thickness distribution of a 150-nm-thick YSZ film across a Si_3N_4 (300nm)/Si / Si_3N_4 (300nm) wafer.	56
3-4	Summary of microfabrication processes for free-standing thin films.	57
4-1	Testing flow for key thermomechanical properties of thin membranes.	94
4-2	A picture (<i>top</i>) and schematic (<i>bottom</i>) of the Tencor FLX curvature measurement system, from [4, 1].	96
4-3	Total residual stresses of the YSZ films deposited at room temperature; measured as deposited and after post-deposition annealing.	97
4-4	Residual stress evolution of an 87-nm thick YSZ film deposited at room temperature during post-deposition annealing.	98

4-5	Total residual stresses of the YSZ films deposited at high temperature; measured as deposited and after post-deposition annealing.	99
4-6	Residual stress evolution of a 657-nm thick YSZ film deposited at 500°C during post-deposition annealing.	100
4-7	Buckling evolution of thin square YSZ membranes deposited at room temperature with film thickness of 368 μm	102
4-8	Chrome mask design to pattern silicon nitride to release square membranes for center buckling height measurement; wafer view (<i>top</i>) and enlarged die view (<i>bottom</i>).	104
4-9	Extracted Young's modulus on the sample sq05 by center deflection measurement of square buckled membranes by die.	105
4-10	Extracted Young's modulus on the sample sq06 by center deflection measurement of square buckled membranes: by die in inner ~ 40 -mm-radius area (<i>top</i>), by distance from the wafer center (<i>bottom</i>)	106
4-11	Extracted Young's modulus on the sample sq07 by center deflection measurement of square buckled membranes by die.	107
4-12	Comparison of extracted Young's moduli from dies that are radially ~ 40 mm away from the wafer center with calibrated (by -10%) and measured (at 60mm away from the wafer center) thicknesses.	108
4-13	Cross-sectional view of microstructure of sputter-deposited YSZ films with mixed amorphous and columnar crystalline phases, from [1]. . .	110
4-14	Simulated maximum (tensile) and minimum (compressive) stresses in the YSZ film (150nm) deposited at 500°C when annealed to 625°C. . .	111
4-15	Simulated maximum (tensile) and minimum (compressive) stresses in the YSZ film (250nm) deposited at 500°C when annealed to 625°C. . .	112
4-16	Schematic of the bulge test setup at thin film mechanics laboratory at Harvard University, from [5].	113
4-17	Chrome mask design to pattern silicon nitride to release bulge test samples.	114

4-18	Stress-strain slopes on bilayer of YSZ (125nm, deposited at room temperature) and silicon nitride (~300nm) film, just silicon nitride (~300nm) film, and subtracted slope for YSZ stiffness estimation.	115
5-1	Cross sectional view of the fuel cell device with electrical outputs (top Pt-YSZ and Pt contact pad).	133
5-2	Layer layout of the fuel cell device and the die layout on a wafer.	134
5-3	Typical dust defect in the electrolyte YSZ layer observed with SEM.	135
5-4	Chrome mask design to pattern silicon nitride to release fuel cell tri-layer membranes; wafer view (<i>top</i>) and enlarged die view (<i>bottom</i>).	136
5-5	Edges of the films deposited through a silicon shadow mask (<i>top</i>) and a metal shadow mask (<i>bottom</i>) by SEM.	137
5-6	XRD SEM signals on a fuel cell tri-layer membrane on the KOH etch side after plasma etching	138
5-7	Diesawed cross section of the tri-layer stack (Pt-YSZ/YSZ/Pt-YSZ) inspected by SEM with thicker YSZ (~1 μ m) than in the tested fuel cell device (YSZ thickness of 150 nm).	139
5-8	Fuel cell stack (~450-nm thick) buckling behavior under thermocycles observed with Zygo surface profiler. All images taken at room temperature.	142
5-9	Fuel cell stack (~750-nm thick) and bi-layer (~500-nm thick) buckling behavior under thermocycles observed with Zygo surface profiler.	143
5-10	Comparison of simulated in-plane stresses with two different film thickness (250 nm and 750 nm) deposited at 500°C when annealed up to 625°C.	144
5-11	Illustration of power test fixture [6].	145
5-12	Nitrogen signal history during the first curing cycle of silica-based bonding, provided by Cui [6].	146
5-13	Power output from the tri-Layer (Pt-YSZ/YSZ/Pt-YSZ, each 150-nm thick) at 450°C and 500°C (<i>top</i>), and at 350°C and 400°C (<i>bottom</i>).	147

5-14 Ratio of oxygen and nitrogen signals during the thermocycle for power
test. 148

List of Tables

3.1	Sputtering conditions and deposition rates of YSZ, Pt, Ti, and Pt-YSZ.	55
4.1	Bulk modulus of YSZ and silicon with (100) orientation, from [7, 8, 9].	95
4.2	Measured slopes of temperature-total stress plots of YSZ films to extract "modulus-CTE" products: $\frac{E_f}{1-\nu_f}(\alpha_s - \alpha_f)$.	101
4.3	Deposition and annealing conditions for test samples for center height measurement, and their measured residual stresses.	103
4.4	Extracted Young's modulus and CTE from center height measurement of square buckled membranes.	109
5.1	Statistics of electrical shortage between the anode and cathode layers on power test samples (small 1.25mm×2.5mm, middle 1.25mm×3.75mm, and large 2.5mm×3.75mm).	140
5.2	Statistics of square released tri-layer (Pt-YSZ/YSZ/Pt-YSZ) and bi-layer (YSZ/Pt-YSZ) membranes that survived thermal cycles.	141

Nomenclature

a	Width of released square or rectangular membranes
C	Compliance matrix
$c_1, c_2, c_3, c_4, c_5, c_6$	Coefficients of the function of normalized center deflection in terms of normalized difference between residual strain and first critical buckling strain
c_{11}, c_{12}, c_{44}	Compliance matrix components of cubic single crystal
$\mathbf{e}_1, \mathbf{e}_2, \mathbf{e}_3$	Unit vectors of <100> axis system
E_f	Young's modulus of film
\overline{E}_f	Biaxial modulus of film
E_l^*	Longitudinal stiffness after axis transformation
E_s	Young's modulus of substrate
E_t^*	Transverse stiffness after axis transformation
$g_{mn}^s(x, y)$	Trial displacement function with the axes and rotation symmetries
h_f	Film thickness
h_s	Substrate thickness
$l_1, l_2, l_3, m_1, m_2, m_3, n_1, n_2, n_3$	Coefficients that relate unit vectors of <100> axis system and the system after axis transformation
P, Q, R	Coefficients in the out-of-plane displacement (ω) function
q	Pressure applied to membranes in bulge test
q_1	Pressure that balances tensile residual stress
q_2	Pressure that stretches membranes
S	Stiffness matrix
s_{11}, s_{12}, s_{44}	Stiffness matrix components of cubic single crystal

s_{11}^*, s_{12}^*	Stiffness matrix components of cubic single crystal after axis transformation
$\mathbf{u}_1, \mathbf{u}_2, \mathbf{u}_3$	Unit vectors of system after axis transformation
ΔT	Temperature change
U	Strain energy
u, v, w	Displacements
ω_0	Center deflection of buckles membranes
$\Delta\alpha$	Difference between coefficient of thermal expansion of substrate and film
α_f	Coefficient of thermal expansion of film
α_s	Coefficient of thermal expansion of substrate
ε	Strain tensor
ε_0	In-plane strain caused by residual film stress; residual strain
$\Delta\bar{\varepsilon}_0$	Normalized difference between residual strain and first critical buckling strain
ε_{cr1}	Critical strain of first buckling mode
$\varepsilon_{thermal}$	In-plane thermal strain
ε_{total}	In-plane total strain include mechanical, thermal, and residual strains
κ	Curvature
κ_f	Curvature of substrate deposited with film
κ_s	Curvature of substrate
$\Delta\kappa$	Curvature difference before and after film deposition
ν_f	Poisson's ratio of film
ν_s	Poisson's ratio of substrate without film
σ_0	Residual stress
$\sigma_{0beforeanneal}$	Residual stress before post-deposition annealing
$\sigma_{0afteranneal}$	Residual stress after post-deposition annealing
$\sigma_{thermal}$	Thermal stress

Chapter 1

Introduction and Motivation

The scientific understanding and engineering technology to develop portable micro-chemical power devices have been investigated by an interdisciplinary team at Massachusetts Institute of Technology (MIT) as part of a Multidisciplinary University Research Initiative (MURI) sponsored by the Army Research Office (ARO). Development of a microfabricated solid oxide fuel cell (μ SOFC) is one of the MURI team's research efforts. Due to their its high fuel power density and optimized efficiency due to micro scale structure, μ SOFCs can potentially achieve higher power output with lighter weight than existing batteries. MURI project work involves design of all the components to generate electricity, and includes micro-reactor development, SOFC and catalyst development, material/structural/packaging studies, and system level analysis. Among all these topics, this thesis focuses on thermomechanical characterization of μ SOFC materials and structures in order to successfully fabricate thermomechanically stable fuel cells with optimized efficiency. The remainder of this chapter establishes the motivation behind development of this particular micro-chemical power device, followed by an overview of this thesis.

1.1 Motivation for Microfabricated SOFCs (μ SOFCs)

This section presents key factors that make microfabricated SOFCs competitive portable micro power devices. Fuel cell operation and advantages over other existing technolo-

gies will be illustrated, as well as their major disadvantages. Then, the section ends with an explanation of how fabrication in micro scale can counter many of these disadvantages.

Fuel cells have been rigorously investigated as alternative power generation devices in recent years. Fuel cells are electrochemical devices that directly transform chemical energy of oxidants and fuels into electrical current and heat. A typical fuel cell structure consists of three layers, an ion-conducting electrolyte sandwiched by a fuel electrode (anode) and an oxidant electrode (cathode). The electrochemical reaction of general SOFCs is illustrated in Figure 1-1. At the anodic electrocatalyst, hydrogen fuel is decomposed into hydrogen ions and electrons. These electrons are transferred through outer electric connections and through the load (or storage device) to the cathodic electrocatalyst side, and react with oxygen fuel generating oxygen ions. These oxygen ions conduct through insulating electrolyte layer, and react with the hydrogen ions at the anode to form water. The resultant voltage is theoretically low on the order of volts, and practical voltage is lower due to polarizations (activation, concentration, or ohmic) and irreversibilities. As for a structural effort to reduce polarization, the anode and cathode materials are often highly porous in order to increase phase boundary lengths and thus to improve reaction rates.

Fuel cells have three essential advantages over other existing power generation devices such as fossil-fuel power generation or traditional battery technology. First, fuel cells have achieved energy conversion efficiency as high as 60–80% [10], while higher-heating value (HHV) efficiency of most fossil-fuel power plants is 35–40% due to Carnot cycle limitations. Besides, this high efficiency can be maintained over a wide range of operating load conditions, and is independent of the cells' size scale. Second, some types of fuel cells, including SOFCs, can accommodate various hydrocarbon fuels in addition to pure hydrogen, though minimum purification is often required to reduce carbon dioxide production. For example, SOFCs can run on steam-reformed natural gas, light petroleum distillates, or steam-reformed alcohols. These fuels have significantly higher power densities ($\sim 5\text{--}35$ MJ/kg) than those of traditional battery technologies (~ 5 MJ/kg). Third, fuel cells are rather clean and

safe technology with low-emission of carbon dioxide, less waste heat, and/or less noise. With the advantages listed above, all types of fuel cells are potentially effective alternatives to other power generation devices.

SOFCS were particularly chosen for this research work to create a "portable" power device, on account of additional advantages to be explained below. So far, five prominent fuel cell technologies have been explored, and these are categorized by their electrolytes: phosphoric acid, molten carbonate, solid oxide, alkaline, and solid polymer. Choice of electrolyte decides the current carrier through the electrolyte, fuel and oxidant, operating temperature, performance, stability, cost and other factors. For instance, alkaline and solid polymer electrolytes require purified hydrogen as fuels because they react with carbon dioxide derived from carbonaceous fuels. Meanwhile, characteristics of solid oxide electrolytes qualify the SOFC as a satisfactory candidate for microfabricated fuel cells with high efficiency. First, solid oxide electrolytes are solid, and thus SOFC structures are compatible with microfabrication. Design or fabrication in micro scale are not possible with aqueous electrolytes. Second, SOFCs require high operation temperature (600–1000°C) to achieve high ionic conductivity. The extra energy introduced by the high temperature state can increase fuel efficiency up to 80–85% without expensive precious metal catalyst. The heat also reforms fuels internally, removing the need for additional reformers. Third, SOFCs are not poisoned by carbon monoxide, and thus can accommodate various, even inexpensive fuels again with minimum fuel purification. SOFCs are great materials to start investigation on microfabricated power devices due to their structural flexibility, fuel versatility, and relatively low cost [11, 12, 13].

With all these strong points listed above, SOFCs still have three major drawbacks: high temperature operation, cost, and efficiency. For portability of fuel cells, heat management (supply, control, and retainment) are key restrictions for efficiency and safety. In addition, the high temperature operation results in slow startup. The cost of the completed SOFC power generation setup can be reduced thanks to SOFCs' characteristics by removing reformers or fuel purifiers and by using inexpensive hydrocarbon fuels with high power density. But, the cost may still need to be reduced.

As for efficiency, SOFCs substantially achieve higher efficiency than most of other fuel cell types. Efficiency is critical to produce reasonable power levels because SOFCs' power is limited by the low voltage output determined by the electrolyte materials.

Here, microfabrication comes in as a solution to counteract these difficulties imposed by SOFC characteristics. As for heat management, micro scale helps to reduce heat amount required to operate cells, while it still requires thermal management to adjust start-up speed or thermal cyclability. Microfabrication also reduces the cost with its mass production nature. In addition, microfabrication could have a large influence on performance. To improve performance, methods such as electrode sintering and interfacial layer formation have been investigated in the past. In this research project, electrochemical performance was planned to be improved by reducing electrolyte thickness. The electrical/ohmic resistance should be significantly reduced by thinning the electrolyte down to a couple of hundred nanometers, which process is possible uniquely by microfabrication [13, 14, 15].

1.2 Motivation of Thesis Work

To successfully fabricate μ SOFCs in micro scale, thermal stability of fuel cell structure at high operation temperature is essential along with several other requirements. Traditional fuel cell configuration consists of stacked multiple layers made of various materials. Due to differences of stress state and material properties in each layer, significant stresses can be introduced and might eventually cause failures at elevated temperatures of operation. In macro scale, a tubular structure with concentric layers is the most efficient design to even out such mismatches with axisymmetry. However, since most of microfabrication processes are planar, the μ SOFC structure in this research work was designed to be released a tri-layer (anode, electrolyte, and cathode) planar membranes. Stresses in the tri-layer stack evolve as follows: Originally, each membrane in the stack has a residual stress state as deposited, and this stress is a function of the film fabrication conditions. As the temperature increases, stresses develop under the influence of coefficient of thermal expansion (CTE) mismatches,

its biaxial modulus, and boundary conditions imposed by adjacent layers and supporting structure. At the high temperature that the SOFC operation requires, the mismatch of CTEs in each layer can introduce significant stresses in layers, causing failure modes such as buckling, delamination, fracture, or cracking as shown in Figure 1-2. To avoid failure modes and to assure structural thermal stability at high temperature, studies of thermomechanical properties of each layer, including residual stresses, CTEs, and biaxial modulus, in micro scale is needed. Mechanical characterization in micro scale introduces another level of difficulty in sample preparation, testing, data interpretation, and other aspects, which will be explained in Chapter 2. Based on measured thermomechanical properties, the design of μ SOFC fuel cell stacks can be optimized in terms of efficiency by thinning its electrolyte while maintaining thermomechanical stability of the whole structure under the large thermal excursions that SOFCs experience during operation.

1.3 Objectives and Scope of Thesis

The objectives of this thesis work are to experimentally characterize material properties and residual stress state of μ SOFC materials, and to design, fabricate, and test tri-layer fuel cell stacks based on this mechanical study. In this thesis work, mechanical characterization of fuel cell structural components was limited only to that of the electrolyte, assuming porous anode/cathode layers have significantly small structural effects. The electrolyte investigated was yttria-stabilized zirconia (YSZ), one of the most common SOFC electrolytes. YSZ was selected as the μ SOFC electrolyte in the MURI project based on its advantages supported by experimental data [16] to be explained in Chapter 2. Mechanical characterization in micro scale involves higher complexity and is differentiated from that in macro scale, which will also be discussed in detail in Chapter 2. The main objectives of this thesis are:

- Characterize the residual stress state in sputtered YSZ films as deposited and stress evolution under thermal cycling.

- Develop and experimentally complete a thermomechanical characterization flow that is independent of residual stress state (tensile or compressive).
- Extract material properties, particularly CTEs and biaxial modulus, of sputtered YSZ in thin membrane form using the thermomechanical characterization flow from above.
- Identify microstructural and compositional factors influencing YSZ film properties, including mechanisms where possible.
- Design and build thermomechanically stable fuel cell structures based on the mechanical properties obtained above and nonlinear in-plane stress analysis.
- Test the μ SOFCs to validate improved efficiency through electrolyte thinning.

The approach taken to achieve these goals is primarily experimental. The details will be described in the rest of the thesis chapters. In Chapter 2, background work on mechanical characterization of thin films and YSZ, and existing work on μ SOFCs are presented. Microfabrication procedures to fabricate thin membranes are presented in Chapter 3. This chapter is followed by a completed thermomechanical characterization flow chart and its application to the fabricated YSZ thin films (Chapter 4). The characterization results are compared with the previous work in the same chapter. With the material properties characterized, maximum in-plane stresses under thermocycling were estimated by energy minimization method with von Karman nonlinear plate theory. Based on this stress analysis, fuel cell stacks were designed, built, and tested as explained in Chapter 5. In Chapter 6, results from this thesis, major contributions, implications for further improvement of μ SOFCs, and suggestions for future work are discussed.

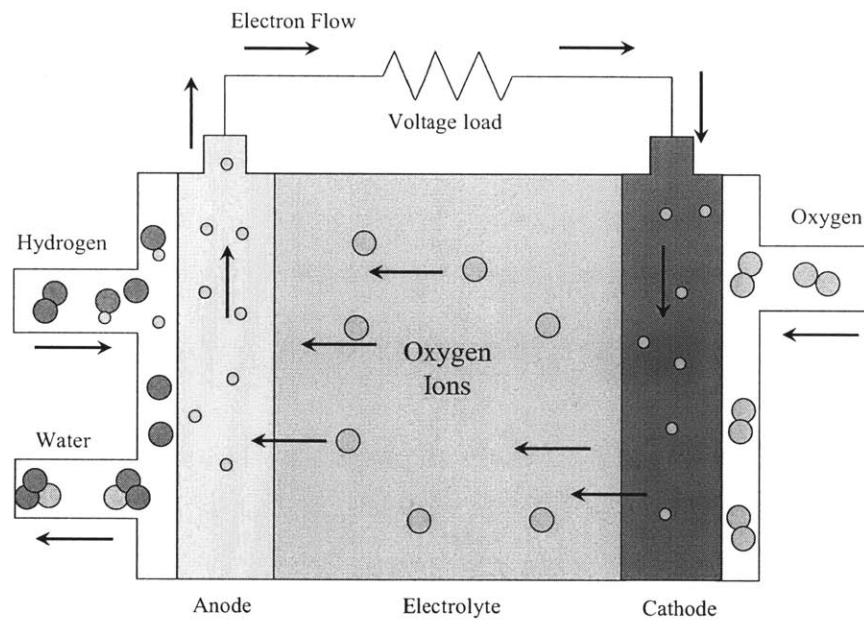


Figure 1-1: Electrochemical reaction of solid oxide fuel cells.

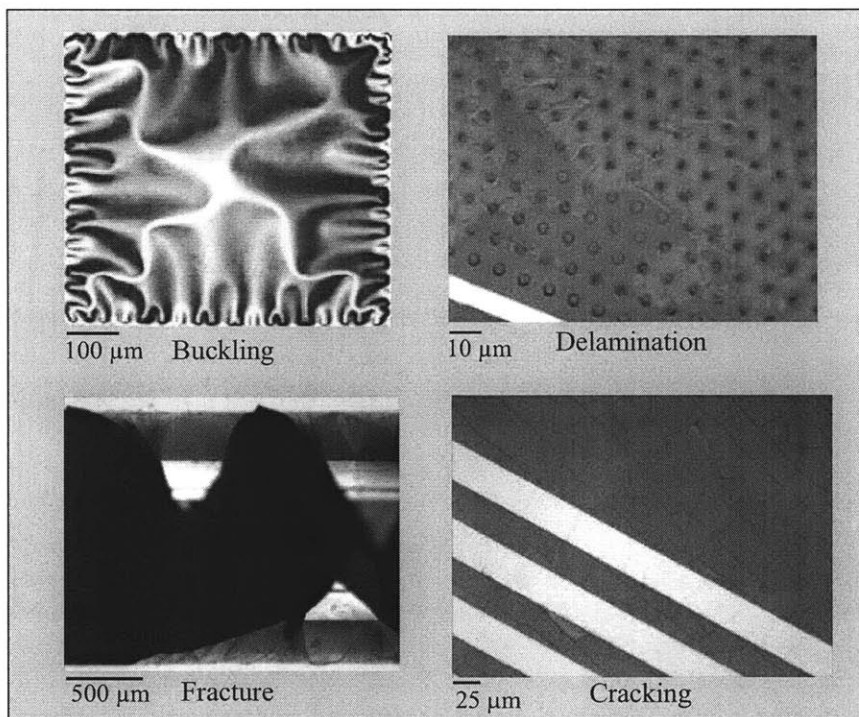


Figure 1-2: Failure modes of thin membranes, from [1].

Chapter 2

Background and Prior Work

This chapter covers background knowledge and prior work that aid in understanding thin film materials characterization in general, characterization of YSZ regarding its residual stress and Young's modulus, and design and fabrication of μ SOFCs. Some material properties were identified as important inputs for the μ SOFC design work in the MURI project. However, due to their high dependence on fabrication process, these properties were unknown for the YSZ films deposited with particular conditions in our facility. Thus, characterization of these properties on these particular membranes fabricated was critical. Certain special testing techniques are suggested to extract required properties in the correct direction (in-plane) relevant to design of μ SOFCs. Based on the selection of these techniques shown in this chapter, the properties of YSZ are acquired and finally utilized in design and fabrication of μ SOFCs in Chapter 4 and 5. The sections on YSZ in this chapter draw heavily from the review work done by Quinn [1].

2.1 Material Property Characterization of Thin Film Materials

The importance of mechanical characterization of microstructures has become rapidly significant as microelectromechanical systems (MEMS) technologies evolve in various

fields. Accurate material properties are essential to effectively design such MEMS devices. Over the past decade, many testing techniques to obtain these properties have been established. Just like macro structures, microstructures exhibit elastic, plastic, anelastic, and visco-elastic constitutive behaviors. Some tests to characterize relatively thick films were derived from macro scale mechanical tests acknowledged by American Society for Testing and Materials (ASTM) [17]. However, as testing of various microstructures progressed, significant differences in the nature of testing in micro and macro scales have been noticed. As for a key phenomena driving this difference, material properties of microstructures are highly dependent on fabrication processes. Different fabrication facilities, or even from run to run within a single facility, material properties of fabricated microstructures likely vary. Related to this variation of properties, mechanical properties in micro scale could differ much from those of bulk due to its microstructure. Yield or failure stresses and strains of some small structures were found to be much larger than those of bulk possibly due to less flaws in the structures [18]. Other properties of structures such as resonance frequency of cantilevers are highly length-scale dependent, and thus can achieve extreme dynamic characteristics if desired. Another consideration should be given to the fact that test structures are often different from structures in actual devices (integrated). Testing specimens are often un-packaged from the device (non-integrated) for ease of fabrication and testing. With all the factors above, accurate measurement and characterization specific to each material in the specific structure, and its fabrication method, are indispensable to produce devices successfully. However, these characterization tasks in micro scale add many difficulties, including specimen preparation, accurate measurement at small scales, and accurate modeling of microstructures for analysis. Common sources of error include geometric conditions imposed by fabrication processes (shapes, residual stresses, or boundary conditions), metrology, or limitation of analytical models used to extract properties. Various experimental techniques specifically designed to test microstructures, especially thin films, will be reviewed here [17].

A good set of potential mechanical tests in microstructures have been established. Just like in the macro structure, mechanical tests are operated by applying a known

load or displacement to a well-characterized test structure, and by measuring the response of this structure. Currently available techniques cover a wide range of microstructures and material properties of interest. Techniques derived from macro scale test are the tension test, bend test, dynamic test, and nanoindentation test. As for details, the tension test is a straightforward extension to micro-scale with simple data reduction [19, 20]. Bend test is simple bending of various structures with different boundary conditions, and requires an analytical model for each structural setup. Bulge test involves with exertion of pressure to thin membranes: film stiffness can be obtained from measured center deflections as a function of the applied pressure. Dynamic (resonant) test measures stiffness and stress by vibrating cantilever beams [21]. Nanoindentation test is a hardness test with indentation to a thin film structure and measures stiffness perpendicular to the film plane as well as hardness [22]. Some characterization methods were designed specifically for microstructures. Wafer curvature test measures residual stresses of thin films due to intrinsic and extrinsic stresses (e.g., thermal mismatch). Passive strain sensor [23] is another method specifically for microstructures. It amplifies micro strains for easier and accurate measurement. An optical technique called Raman spectroscopy, which display Raman spectrum, was also developed for stress measurement. This optical method works only with certain single crystalline structures, but requires no sample preparations. With all the testing techniques shown above, now the key is selection of one or multiple characterization methods. Some good review papers [17, 24] help in selecting the most suitable method. Types of structures (integrated/non-integrated, thin or thick, or free-standing or constrained) and material properties of interest decide optimal methods. The selection can be further narrowed down when ease of instrumentation, specimen preparation, or data reduction are also pursued.

In this work, thermomechanical characterization of thin film membranes is pursued focusing on modulus and CTE. Thin membrane structure in this thesis work is defined as structure whose film thickness is comparable with its material grain sizes (normally less than $1\mu\text{m}$). According to the method selection charts available [17], the following are available for thin film modulus testing; tension test, microbeam

bend test, bulge test, M-test, wafer curvature measurement, resonance test, strain gage test, and Raman spectroscopy. Among them, a combination of wafer curvature measurement, bulge test, and height measurement of released membranes was chosen for characterization of the particular thin membrane structure for this work. Detailed reasoning behind this choice will be presented in Chapter 4.

2.2 Mechanical characterization of YSZ Thin Membranes

In this work, the most common solid-oxide fuel cell electrolyte, yttria-stabilized zirconia (YSZ), was chosen as a good μ SOFC candidate electrolyte. In early stages of the project, two possible SOFC electrolytes, YSZ and gadolinium-doped ceria (GDC), were inspected. YSZ was chosen over GDC for its higher ionic conductivity [11] and its better thermomechanical stability and strength [16]. In this section, followed by the thin film characterization reviewed above, mechanical characterization focused on thin membranes made of sputtered YSZ materials is reviewed including their microstructures, residual stresses, Young's modulus, and CTE.

2.2.1 Microstructure of Thin Films

Microstructure determines the mechanical properties of films, and the effect can be significant. Studies of microstructure are essential to understand the mechanisms behind particular properties of thin films. The following includes a discussion of the evolution of microstructure, requirements of microstructure of YSZ to work as SOFC electrolyte, and characteristics of microstructure of sputtered films.

Microstructure Evolution Mechanisms

Microstructure evolves during deposition under the influence of deposition conditions and the substrate. Film deposition mechanics of sputtered films will be explained below. As illustrated in Figure 2-1, typical deposition starts with formation of atom

clusters called grains, their growth, their coalescence, and their further growth after coalescence.

Grains are formed by atoms deposited on the substrate or on top of the deposited layer. Their movement, such as absorption/desorption or diffusion, are key elements to decide grain formation. These activities are highly dependent on temperature, flow flux, and substrate characteristics. Diffusion distances can be either limited by desorption rate, as the distance diffused before desorption, or by adatom clustering, as the distance diffused before the arrival or interaction with other adatoms. Substrate lattice can serve as an atomic template for film growth, and imposes specific orientation relationship between the lattices of the film and the substrate. When lattices are matched, grain growth progresses in homoepitaxy form (Frank-Van der Merwe). However, this lattice match rarely happens. More typically, when lattices of the substrate and the film material do not match exactly, epitaxy still occurs, but deposition forms oriented islands (Volmer-Weber) as previously illustrated in Figure 2-1. These atom clusters eventually reach the critical size to allow growth into clusters rather than diffusion. As deposition continues, grains grow and finally coalesce with each other. When all grains have the same orientation, film growth shows Volmer-Weber epitaxy. When grains have different orientations, grains will form a polycrystalline film with grain boundaries. The post-coalescence film growth is governed by minimization of total energy (strain energy and surface energy dominate) depending on the film thickness and grain boundary mobility.

Microstructures can be characterized by their grain size, distribution, average texture (grain orientation), grain shape (columnar or equiaxed), porosity, and surface roughness. These microstructures can be controlled by deposition conditions such as temperature of flow flux, as mentioned above. For example, with high temperatures (compared with the melting temperature of the film material) and low flux, atoms can have enough diffusion distance to achieve ordered growth of the film to form nearly fully textured grains (equiaxed). The opposite example is low temperature and high flux condition, which allows thin continuous film because this condition prevents diffusion of atoms and increases the number of clusters. The film microstructures

can be categorized by its grain orientation as amorphous, columnar with shadowing, columnar polycrystalline, and equiaxed polycrystalline as illustrated in Figure 2-2 [1, 25, 26].

YSZ Microstructure Requirements for a SOFC Electrolyte

Doped zirconia and zirconia alloys are representative electrolytes for SOFCs. In addition to its ionic conductivities, they are also known for low thermal conductivities, high strength, toughness, and hardness [27, 28]. As with zirconia, YSZ's microstructure is characterized as monoclinic with a crystal system where cell dimensions are of unequal length. The structure changes from monoclinic, tetragonal to cubic as heat energy is supplied to the structure as illustrated in Figure 2-3. Zirconia by itself requires temperature above 1170°C to achieve certain phases, tetragonal or cubic, for high enough ionic conductivities. To moderate this high temperature requirement, pure zirconia is typically doped with a second oxide such as CaO, Mg, O, Al₂O₃, or Y₂O₃ to increase oxygen vacancies, and thus to improve ionic conductivity [1, 13]. Introduction of defects into the crystal structure enhances ionic mobility by introducing lattice distortion and lattice defects, thereby reducing ions wedged into the ideal lattice [11]. The goal of doping is to stabilize the zirconia to a particular crystal structure with high ionic conductivity from room temperature to operation temperature. In bulk scale, zirconia was found to be tetragonal at room temperature with 2–8 mol% yttria dopant, and to be fully stabilized, cubic, with more than 10 mol% yttria dopant [29]. In micro scale, fabrication techniques have a great influence on the film structural growth, and the phases vary significantly from those of the bulk. Monoclinic, and mixed monoclinic and tetragonal structures were observed with as low as 2–3 mol% yttria dopant, and pure tetragonal structure was observed with 10

mol% yttria dopant [27, 30, 31]. Post-deposition annealing resulted in mixed-phase films as well as complete phase changes [27, 30].

Microstructure of Sputter-Deposited YSZ Thin Membranes

For deposition of YSZ in thin membrane form, several techniques have been investigated [32], including both chemical and physical processes such as chemical vapor deposition (CVD), sol-gel deposition, modified plasma spray techniques, and physical vapor deposition. Among these options, sputtering is a viable option for deposition of working YSZ electrolyte. Sputter technique is one type of physical vapor deposition (PVD) processes. In this physical process, chemically inert atoms ionized by a plasma, such as Argon, bombard a target, and ejected materials from the target deposit on the substrate. More details will be explained in Chapter 3. The thickness range of sputtering is on the order of $1\mu\text{m}$, which can achieve enough thinning effect to reduce the electrolyte impedance as discussed in Chapter 1. More importantly, sputtering has the ability to produce particular crystalline structures required for ionic conductivity. YSZ films sputtered generally grow in a columnar form with equiaxed structure due to high energetic bombardment such as large applied substrate bias [33, 34]. Microstructure depends highly on its fabrication processes. Sputtered YSZ structures with the thickness range of $0.1\text{--}5\mu\text{m}$ were observed to be monoclinic [35], tetragonal [29], or cubic [33, 36, 37], when inspected with X-ray diffraction (XRD), e-beam diffraction, and Raman spectroscopy. This variation is attributed to yttria content differences. Mixtures of crystalline and amorphous microstructures were also observed [27].

Based on the work presented above, sputter deposition was adopted to fabricate the SOFC electrolyte in this work. Quinn [1] deposited YSZ films with the same fabrication recipes and facility, and inspected their film composition, structure, and morphology. The composition of the YSZ target used was 4.7 mol% of $\text{Y}_2\text{O}_3\text{-ZrO}_2$ ($\text{Y}_{0.03}\text{Zr}_{0.31}\text{O}_{0.66}$ by atom fraction and $\text{Y}_{0.09}\text{Zr}_{0.91}\text{O}_{1.955}$ normalized to one cation). The YSZ films deposited with the target showed uniform composition through thickness when inspected with secondary ion mass spectrometry (SIMS). Its composition

was averaged to be $Y_{0.05}Zr_{0.30}O_{0.64}$ with wavelength dispersion spectroscopy (WDS). With the error range of 10–20 % of WDS, this result can conclude that deposited films are nearly stoichiometric. As for structure, columnar microstructure along with slight widening of grains was observed through the thickness of the film with transmission electro microscopy (TEM). Finally, texture was examined to determine the type of crystalline structure with XRD. The peak locations and relative intensities of the sputtered YSZ films showed good agreement with those of standard polycrystalline, unstressed, randomly-oriented cubic structure. Assuming misalignment can be attributed to minor differences in composition and the presence of residual strain/stress, the YSZ film deposited at room temperature can be characterized as cubic. This microstructural stabilization at room temperature has been predicted based on stabilization by decreasing grain sizes [38, 39], and have also been observed [35]. This result is also compatible with other YSZ layers deposited from targets with similar composition [27, 33]. Thus, it can be concluded that the YSZ films with proper ionic conductivity through their cubic structure were successfully deposited with our sputtering conditions and facilities.

2.2.2 Residual Stress of YSZ Sputter-Deposited Thin Films

Residual stresses play a key role in thermomechanical stability of released thin membrane form to be used in our SOFC device. Residual stresses originate from both intrinsic and extrinsic factors. Extrinsic stresses occur after deposition, due to external influences such as differential CTE during heating/cooling, or phase transformations. Intrinsic stresses are closely correlated to film deposition process [1, 40, 41, 42, 43]. This subsection focuses on the mechanisms behind this intrinsic stress of sputter-deposited YSZ films, the experimental measurement of their intrinsic stresses [1, 16], and its implications.

Mechanisms of Intrinsic Stress

Intrinsic stresses vary roughly from 2GPa compressive to 2GPa tensile in the sputtered YSZ films using recipes similar to those used in this work [16]. Stresses are attributed to microstructure or phase transition determined by deposition condition, mainly bombardment energy and substrate bias in RF sputtering [33], as well as lattice mismatch and constraints imposed by the underlying substrate [41]. In the following, the mechanisms behind formation of tensile stress, of compressive stress, and of stress relaxation will be explained.

Tensile stresses are generated by elastic deformation due to energy minimization under the boundary constraints imposed by substrate, assuming good adhesion between the film and the substrate [43, 44, 45, 46]. Grains grow in a way such that total energy is minimized. Total energy consists of surface energy, grain boundary interface energy, and strain energy. As thickness of the film increases, this energy minimization focuses on reducing grain boundary interface energy (or surface energy), which induces elastic deformation of grains. This elastic deformation causes tensile stresses. Models of this stress evolution corresponding to each stage of grain growth have been investigated [40, 46, 47], and these models have been verified with experimental results for a variety of sputtered materials [41, 48, 49]. Closure of microscopic voids are also considered to be one cause of tensile stress evolution [43].

Compressive stresses are expected to be caused by surface stresses, impurities, or high kinetic energy during deposition. Surface stresses result from the larger equilibrium spacing due to fewer atomic bonds at the film's surface, and can incorporate an excess concentration of atoms in the film. This phenomenon causes the compressive stress when surface atoms are constrained [50]. These mechanisms were again experimentally confirmed [49, 48, 51, 52]. Impurities, different-size atoms in the lattice or at grain boundaries, are expected to cause compressive stresses due to the similar reason as above. However, its effect was shown to be small for many material systems [53]. Finally, interstitial implantation of sputtered film atoms or gases originating from the evolving surface of the deposited film can also cause compressive stresses. The atoms

in the developing films are bombarded by arriving atoms or gasses with high energy, and displace the lattice. This forward sputtering mechanism called "atomic peening" is the most common explanation for compressive stresses, because stress levels under low to moderate energy processing conditions are typically tensile or only slightly compressive.

Total residual stress of the thin films is determined by a combination of the tensile and compressive stresses above, and stress relaxation factors. Relaxation occurs when lattice distortions are removed by atom diffusions at the surface or grain boundaries. For example, relaxation occurs at grain boundaries with high mobility or thicker films with smaller surfaces [48, 51, 52]. Relaxation processes through diffusion can be highly promoted with temperature.

Intrinsic Stresses in Sputter-Deposited YSZ Thin Films

Residual stresses of YSZ thin films deposited with our fabrication process and facility have been studied, and this study is critical since properties are highly dependent on fabrication processes. Residual stresses of YSZ films sputtered under various deposition conditions are hysteretic under post-deposition annealing. These results and the mechanisms behind this stress development will be presented in this section.

Baertsch et al. [16] initially studied YSZ films deposited at room temperature and at high temperature (600°C). Residual stresses varied between -865 to -155 MPa compressive. Quinn [1] advanced Baertsch's study, and performed detailed experimental studies of sputtered YSZ films with the same facilities and processes. As-deposited total residual stress state for YSZ on silicon (Si) substrates with (100) orientation and 4-inch diameter ranged from -1400 MPa to 200 MPa, and -1600 MPa to 400 MPa for films deposited at room temperature and 600°C, respectively, over the range of thickness (5nm–1 μ m) and working pressure (5–100mTorr). These measured stresses include not only intrinsic stresses but also extrinsic stresses because the films experience thermal mismatch in the cooling down process after deposition.

With films deposited at room temperature, effects of film thickness and working pressure were investigated [1]. Residual stresses increased by a few hundred MPa with

the film thickness, but reached a plateau of $\sim -100\text{MPa}$ at $\sim 300\text{nm}$ thickness. This phenomena were explained as follows: compressive stress components evolve from lattice distortions and interstitials generated by atomic peening, and these effects are more significant with thinner layers due to their lack of stress relieving diffusion time and due to high surface effect. Also, more grain growth and void coalescence with increasing thickness were confirmed by SEM, and these behaviors promotes tensile stress development [1, 29, 33]. As for working pressure variation, a sharp increase of stress with working pressure was observed under moderate to high levels of energy bombardment. This tendency can be attributed to forward sputtering/atomic peening. With high working pressure, decreasing travel distances of atoms promote their collision, and thus bombardment energy becomes low. Lattice distortions will be reduced, and thus residual stress becomes less compressive. This tendency were also observed by others [40, 42]. Membranes were exposed to annealing cycles up to 500°C after deposition. Hysteretic behavior of $\sim 1000\text{MPa}$ (tensile) increase in total residual stress were observed at $\sim 200^\circ\text{C}$ in the first annealing cycle. The final stress state, $560\text{MPa} \pm 100\text{MPa}$, was roughly independent of deposition conditions. This hysteresis can be attributed to crystallographic phase change [35, 54], classical plasticity and film yielding [55, 56, 43], or relief of compressive atomic-peening stresses through diffusion. Stress (due to atomic peening of sputtered target atoms) relief by diffusion is considered the mechanism at work in the sputtered YSZ films.

The films deposited at high temperature showed a clear difference from films deposited at room temperature. Normally, the intrinsic stress component is expected to decrease with increasing substrate temperature because heating promotes diffusion and thus stress relief. However, high substrate temperature in Quinn's work promoted further compressive stress. Most likely, these compressive stresses were due to atomic peening, since its effect becomes more significant when films are highly crystalline like the ones deposited at high temperature [1]. Temperature, working pressure, and film thickness influenced these films in a similar way as the samples deposited at room temperature shown above. As for post-annealing, stress hysteresis occurred at higher temperature ($\sim 400^\circ\text{C}$) with less hysteresis (a few hundred MPa). Films

deposited at high temperature experience annealing/cooling processes when they are cooled down from the deposition temperature, and thus additional annealing has less effect on their microstructure and residual stresses [1]. Insignificant phase change was observed through XRD studies so that it was ruled out as a stress relief mechanism.

Based on this residual stress analysis, the SOFC stacks with three layers (anode, electrolyte, and cathode) were deposited, and their residual stresses were observed to be mildly tensile or compressive both before and after post-deposition annealing ($-100\text{MPa}\sim 300\text{MPa}$) [1].

Implication of Residual Stresses to Structural Thermal Stability

Residual stress is of great interest because of its direct effect on the device's structure, its failure, and the performance of the final device. The structures of released beams and membranes are significantly affected by residual stresses and stress gradients. These structural variations caused by residual stresses, or the residual stress impact on the performances of the final devices such as resonance or optoelectronic effects, must be designed. In addition, extreme residual stresses can often cause structural failure such as cracking, fracture, or buckling. Thus, design of devices needs to be carefully done with close attention to control these phenomena within a specified limit, based on characterization of residual stress that are sometimes counterintuitive. For example, theoretical simulations have shown that post-buckled films can withstand larger intrinsic stresses or temperature excursions beyond a simple buckling criteria [1]. This analysis is supported by experimental results by Baertsch et al, who observed the sputtered films with compressive stress had better mechanical and thermomechanical stability than electron-beam evaporated films with tensile stresses [16].

2.2.3 Coefficient of Thermal Expansion and Biaxial Modulus of YSZ Thin Films

Other material properties of interest, CTE and biaxial modulus of YSZ in thin film form, were theoretically modeled, and experimentally characterized.

Material properties of YSZ in bulk (polycrystalline, randomly oriented) form has been measured and analyzed. Young's modulus can be calculated based on its cubic structure [57, 58, 59, 60]. Poisson's ratio and biaxial modulus have also been studied [59, 61]. The film of interest for the project consists of textured, partially crystallized columnar microstructure, and thus is expected to have different mechanical properties than the bulk. Mechanical properties of a film vary significantly from those of bulk, particularly for strength as discussed above [62]. The expected value of the product of the CTE and the biaxial modulus for YSZ will be presented in Chapter 4.

Quinn [1] measured the product of CTE and the in-plane biaxial modulus with wafer curvature technique, and measured the out-of-plane Young's modulus and strength by nanoindentation technique. The measured value of the product of CTE and the in-plane biaxial modulus were much lower, almost by half, than the theoretical value calculated with bulk properties. High deposition pressure causes porosity in the film, and the low temperature may cause a mixed amorphous/crystalline microstructure. These microstructures could have lowered the in-plane biaxial modulus and CTE. On the other hand, the measured strength was $\sim 750\text{MPa}$, higher than that of bulk YSZ, 650MPa . In addition, nanoindentation with two indentors was performed to the deposited film to extract hardness and Young's modulus. The out-of-plane Young's modulus was measured as $220\text{--}280\text{GPa}$. This value is equal or above both bulk and upper bounds for a randomly oriented polycrystalline YSZ materials. This increase in the out-of-plane Young' modulus is due to the dominant (100) texture observed in XRD studies of the films. Considering this high stiffness in the out-of-plane direction and the low modulus-CTE product observed in the in-plane direction, Quinn [1] concluded that the structure of sputter-deposited YSZ films consists of columnar crystalline phases and amorphous regions extending through the

film thickness. Apart from the work by Quinn [1], no other modulus or CTE values for submicron YSZ films is known by the author.

2.3 Prior Work on Achieving μ SOFCs

Miniaturization of SOFCs has been theoretically and experimentally investigated by various groups. With variation of deposition methods, SOFCs with electrolyte thickness of 2-20 μm have been fabricated, and produced power output of 110–1935 mW/cm^2 [63, 64, 65, 66]. The values of these power outputs and measured ionic conductivities were comparable with those of macro-scale. In addition, operation temperature significantly decreased from $\sim 1000^\circ\text{C}$ down to the range of 600–800 $^\circ\text{C}$. Similar effects have been observed with different materials such as Samaria-doped ceria solid oxide electrolyte [67], or Nafion, a proton exchange electrolyte [68], where electrolyte resistance significantly depends on grain size and impurity content. However, electrolytes that are thinner than a fraction of one micron and thermomechanical stabilities of such ultra-thin electrolyte structures have not been investigated.

In order to successfully design thermomechanically stable thin membrane structures, SOFCs were analytically modeled to characterize their electrochemical performance, mechanical stability, and reliability and thermal behavior [14, 69]. Thermal stress and thermal transfer were found to be functions of scale. For example, the very thin film structures suffer from large heat loss through air convection and structural conduction, and require appropriate packaging for heat management. Meanwhile, thinning effect theoretically stops improving fuel cell performance once thickness reaches the micrometer range in the operation temperature range of 500-600 $^\circ\text{C}$ [14]. Srikar et al. [14] indicated the design space of thin membranes regarding the residual stresses and the temperature change that films can endure before failing. In that work, and the work of others, failure was determined by a buckling criterion. Tang [69] suggested extending this regime by accommodating "corrugated" membranes for their smaller thermal-induced stress and more effective areas. As for design, they suggested usage of these corrugated membranes as part of substrate to add flexibility.

In this thesis work, this same design regime was investigated to avoid fracture by relieving stresses with out-of-plane deflections in a post-buckled regime. This regime was experimentally verified to be effective. In this work, thermomechanically stable, large-area freestanding (electrolyte supported) thin-film SOFCs will be demonstrated.

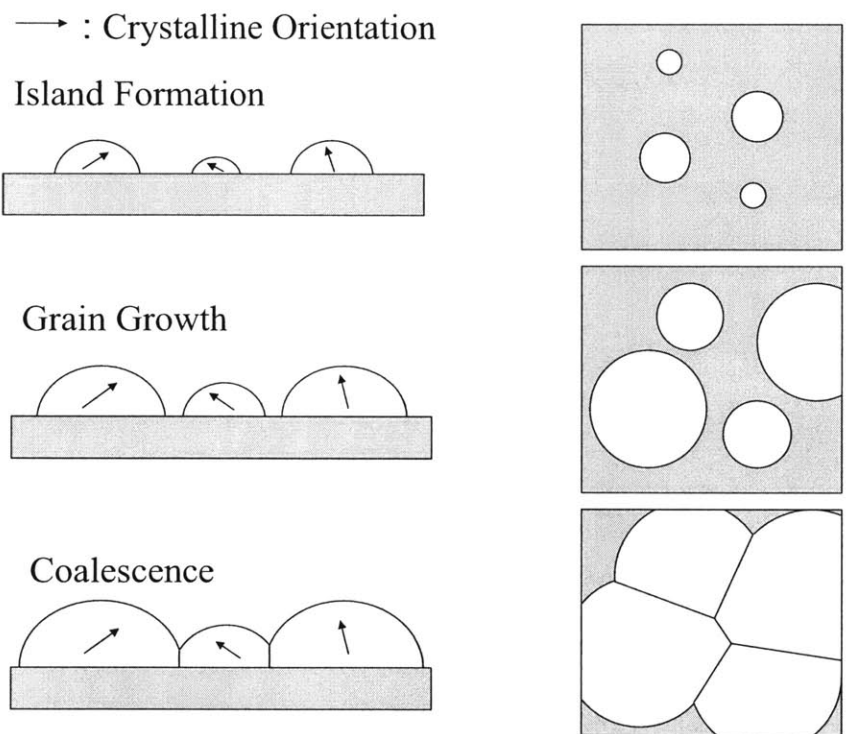


Figure 2-1: Film deposition mechanism of sputtered polycrystalline films: side and top views of grain growth, from [2].

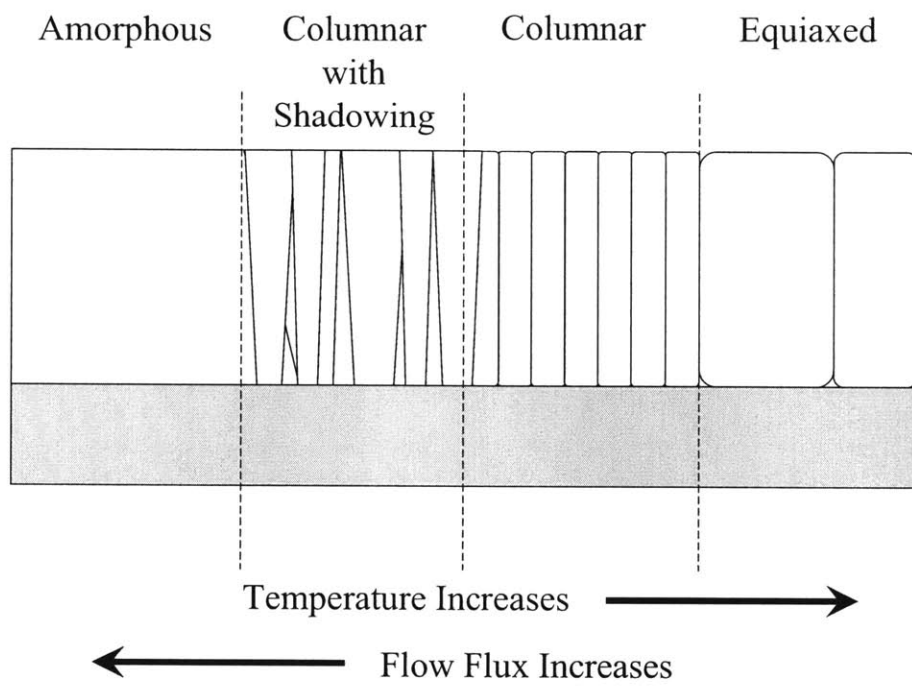


Figure 2-2: Microstructure types determined by deposition conditions, after [2].

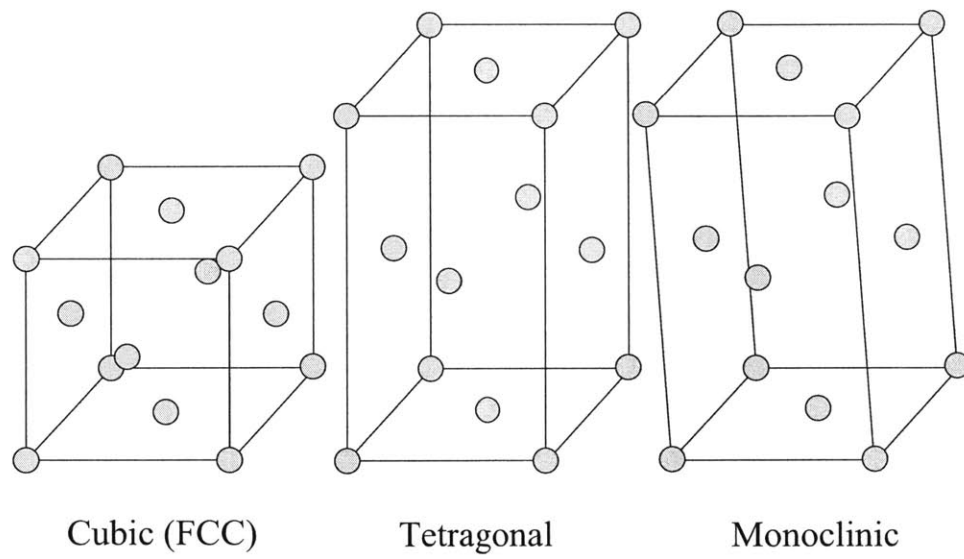


Figure 2-3: Crystalline structure of zirconia with lattice sites occupied by the cations (Zr, Y).

Chapter 3

Thin Film Fabrication

Microfabrication processes for thin membranes will be discussed in this section. Sputtering method was selected for deposition of films of interest, YSZ electrolyte or the tri-layer μ SOFC devices (Pt-YSZ anode, YSZ electrolyte, and Pt-YSZ cathode). The chapter starts with an overview of sputtering, progresses to descriptions of apparatus and conditions, and ends with the overall flow of microfabrication processes for thin membranes. The chapter is limited to the microfabrication of the basic structure of interest in this work: free-standing thin films. The details of additional microfabrication steps that were used to build samples for each test will be covered as they appear in this thesis.

3.1 Sputtering

As mentioned in Chapter 2, sputtering method was chosen to fabricate μ SOFCs for this particular MURI project over e-beam evaporation due to better thermomechanical stability of sputter-deposited films with compressive residual stresses. In addition, sputter-deposited films were confirmed to have microstructures suitable for ion conduction as discussed previously in Chapter 2. More generally, sputtering has advantages in step coverage, stoichiometry control, sensitive thickness control with low deposition rate, accommodation of various targets, and the low vacuum requirement. This section covers issues related to sputter deposition, including its physical process,

its deposition characterization parameters such as energies, and their influences on microstructure of YSZ. After presentation of the sputtering mechanisms, deposition conditions used to deposit films in this work follow.

3.1.1 Sputtering Mechanism

Sputtering is a physical vapor deposition (PVD) process that employs bombardment of energized gas particles on the target to eject film materials for deposition. Traditional configuration of sputtering system consists of two parallel electrodes in a low pressure (1–100 mTorr) inert gas atmosphere (typically Argon) separated by a distance of a few tens of centimeters. The cathode is made of a material to be deposited. When DC or AC voltages (several kV) are applied to the electrodes, electric field is generated between the two. Once this field exceeds the breakdown field of the gas, the voltage arc flashes between the electrodes to capture a plasma. This arc creates a large number of ions and free electrons. The electrons are attracted towards the positively charged anode. On the other hand, the ions are accelerated towards the cathode (the target) with large enough energy to eject the target material. When the target is an electrically conductive material, secondary electrons, in addition to the target particles, will be released when the ions strike the cathode. These secondary electrons are attracted towards the anode. At high field, these electrons have enough energy to ionize neutral atoms. Ions and secondary electrons create each other, and thus the plasma sustains. However, this is not the case with an insulating target/cathode. With DC charge on insulating materials, charges accumulate at each electrode, and the plasma quenches within 1–10 μ sec. When a radio frequency (RF), high frequency alternating voltage above 10kHz, is employed, electrons are accelerated fast, due to their small mass, to both the electrode and the substrate. Both surfaces become negatively charged, and thus ions will be attracted to the both sides. In this way, the plasma achieves a steady state, and films are deposited on the substrate. RF systems operate with a load resistance ($\sim 500 \Omega$), and impedance drops across the two electrodes. The amount of this potential drop varies with target materials and processing conditions. RF sputtering system requires impedance matching

circuit to give necessary resistive load [70]. The sputtering method used in this thesis work is a reactive sputtering process that utilizes a second gas (oxygen in this case) prior to deposition on the substrate, allowing deposition of compounds such as oxides [1, 2, 71].

Parameters that influence these sputtered films are used to assess their quality. Thickness of sputtered films can be assessed with the number of atoms removed per incident ion (sputter field) and amount of atoms sputtered from the cathode. The latter is a function of working voltage, discharge current, working distance (the distance between anode and cathode), and working pressure (sputtering gas pressure). Thickness uniformity can be also predicted by cosine distribution law [3, 72]. With small area source, ejected particles distribute in the way shown in Figure 3-1. With more ions deposited, the film becomes thicker towards the edges of the substrate.

Bombardment energies associated with sputtering process significantly affect resultant structures and properties of deposited films [40] as explained previously in Chapter 2. Energies are contained by particles such as target atoms, gas atoms, and secondary electrons when they are reflected from the target. While secondary electrons do not affect film structure greatly, sputtered atoms and back-reflected neutrals affect film structures and properties with their bombardment energies. Sputtered atoms arrive with moderate to high energy (5–50 eV), and reflected neutrals arrive with even larger energy. With traditional diode plasma system like the one used in this thesis work, bombardment can be adjusted by varying process parameters such as sputtering gas composition, working pressure, or setup geometries. For example, lower working pressure increases the mean free path, resulting in less collisions, so that particles arrive at the substrate with higher energy. Geometric configuration has a similar effect: shorter working distance decreases the probability of collisions, again allowing particles to keep their high energies before arrival at the substrate.

3.1.2 Sputtering Deposition Apparatus and Conditions

The sputtering system used in this project is a diode, plasma, planar magnetron system design by Kurt J. Lesker Inc.(Clairton, PA). As shown in Figure 3-2, the

system has three sputter target positions with diameter of 50 mm tilted by 30 degrees from the vertical. Each target has a shutter between the substrate and the target to control the deposition start time. Magnets are located underneath a copper mounting plate of each target. All three target positions are water-cooled. The working distance between targets and substrates was ~ 9 cm for wafers with 100-mm diameter and ~ 8 cm for wafers with 150-mm diameter held in different wafer holders. Targets are cylindrical pieces with 50-mm diameter and 1-cm thickness. A new YSZ target from ACI Alloys (San Jose, CA) with the same composition (91% Zirconium and 9% Yttrium by mass) previously used by Quinn [1] was introduced, because the old one simply wore out. Pt and Ti targets were obtained from Birmingham Metal (Carson City, NV), and they both had purity better than 99.99%.

The deposition procedure was as follows: targets and a substrate were placed in the sputtering vacuum chamber. The vacuum chamber was first pumped down to 0.8 Torr with a mechanical pump, and then was pumped down to high vacuum ($< 1 \times 10^{-6}$ Torr) with a Cryo-Pump for ~ 5 hours. An ionization gage was degasified with a heating filament before each pressure measurement. Once the base pressure became low enough for sputtering process, the substrate temperature was set by a programmable controller with a resolution of 1°C . After the temperature stabilized at the desirable value, gases were introduced into the chamber, with working pressure and gas ratio set by an MKS multi-gas MASSFLO 647C controller. Rotation of the wafer began at this point to enhance thickness uniformity and coverage. The plasma was finally ignited, starting from a low power value ($\sim 20\text{W}$). A gradual increase in power (3–5 W/sec) was necessary in order to avoid target cracking due to thermal shock. With the sputtering conditions (working pressure, temperature, and power), sputtering was operated with the shutter closed for 20 min. – 1 hour. This pre-sputtering process was to avoid deposition of atoms from the target surface that might be oxidized or contaminated. Sputtering process started by opening the shutters. Once a desirable thickness was achieved, the power was decreased again slowly. After the chamber was cleared and the temperature was decreased to room temperature, the chamber was vented to take out samples.

The deposition recipes were generated by Hertz [73] to achieve the desirable film microstructure necessary for working μ SOFC fuel stacks. Four different materials were sputter-deposited to fabricate YSZ mechanical characterization test samples and μ SOFC power test samples; YSZ, Pt-YSZ, Pt, and Ti. The YSZ target was placed in Position A, and the metals were placed in Position C (see Figure 3-2). Deposition conditions and deposition rate characterized by Hertz [73] are summarized in Table 3.1. The deposition condition of Pt-YSZ was improved in terms of sputtering rate since Quinn's work [1], but still required high temperature (500 °C) deposition to achieve its structure to act a good electrode/current collector. The film composition of Pt and YSZ was characterized as 51/49% by volume, respectively [73].

The deposition rate and uniformity of films sputtered under these conditions were evaluated by Quinn [1] through thickness measurement. Some area on the substrate was covered by a non-volatile hardening paint, such as the commercial office supply "whiteout," to screen deposition. Before loading a sample into the vacuum chamber, this paint was applied \sim 60 mm radially away from the wafer center. The step height from the covered area to the deposited area was measured as the film thickness. A Tencor P10 profilometer was used to measure thicknesses with a stylus having a 2- μ m radius, using a stylus force of 6 mg, 20 μ m/s scan speed, 50Hz sampling rate, and 13 μ m range setting with a resolution of 7.81×10^{-3} Å. Before each measurement, the Veedi 4500Å step-standard was measured to calibrate the machine. The error range averaged over 17 dies was less than 5%. At least three measurements were taken per film, and the averaged value was set as the film thickness. Deposition rates were calculated by dividing these measured thicknesses over the deposition time, since deposition time-thickness plots were linear [1, 73]. Film thickness uniformity across the wafer was also studied by taking thickness measurements at various positions on the substrate. Quinn [1] observed radial thickness variation of +9% in the inner radial area (0–40 mm) on 100-mm diameter silicon wafers, with larger thicknesses towards the rim. This result is consistent with the distribution behavior of ejected target atoms as discussed above. In this thesis work, in addition to silicon wafers with 100-mm diameter, wafers with 150-mm diameters were also utilized. Thickness

distribution on 150-mm-diameter wafers was similarly measured as shown in Figure 3-3. YSZ film of 150-nm thickness was deposited on a substrate of a silicon wafer covered with ~ 300 -nm-thick silicon nitride layer. The thickness was measured at radially distributed locations on lines at 0, 45, 90, 135 degrees relative to the wafer's (110) direction. The error bars in the plots show the minimum and maximum values among the measured thicknesses on those locations. The results showed a good axisymmetric thickness distribution. The thickness variation in the inner ~ 40 -mm radial area was $\pm 5\%$, which is similar to Quinn's data results of 100-mm diameter wafers [1]. With the larger radial length (75 mm), film thickness towards the wafer edges showed sharper increase. The thickness at the closest point to the rim was larger than the thickness measured at the wafer center by $+19\%$. To avoid this non-uniformity, analysis in the following chapters were limited only to the inner 40-mm diameter area of the substrates. The effect of this thickness variation on extraction of material properties will be discussed in Chapter 4.

3.2 Microfabrication of Free-Standing Thin Membranes

The fabrication flow of free-standing thin membranes in micro scale will be described in this section. The processes were relatively simple. The film to be released was deposited on a substrate as previously described. Then, membranes were released by etching the silicon wafer through silicon nitride mask patterns from the other side. Detailed process steps will be described in the following, accompanied by cross-sectional illustrations of the wafers after each step shown in Figure 3-4.

The first half of fabrication processes was performed in the cleanroom environment with classes of 100 and 10,000 at Microsystems Technology Laboratories (MTL) at MIT. Substrates in this work were double-side polished (DSP) single crystal silicon wafers with 100-mm or 150-mm diameters and (100) orientation. First, RCA clean was performed on these silicon wafers to eliminate all organic, oxide, or ionic contami-

nations. After RCA cleaning, low stress silicon-rich nitride of ~ 300 -nm thickness was deposited on both sides of the wafers in a vertical thermal reactor (VTR). The ratio of deposition gases were a mixture of 250-sccm Dichlorosilane and 25-sccm Ammonia, with 250-mT pressure at 775°C . Residual stress of the deposited nitride was calibrated roughly as ~ 210 MPa tensile from wafer curvature measurements. The back side of this nitride was patterned with photolithography to serve as an etch mask. A thin layer of positive photoresist, OCG825, was spin-coated (pour for 6 sec. at 500 rpm, spread for 6 sec. at 730 rpm, and spin for 30 sec. at 2300 rpm). Photoresist was softbaked at 95°C for 30 minutes. The hardened photoresist was exposed through chrome masks to transfer patterns. All the chrome masks were ordered from Fineline Imaging, and were with a resolution of $10\ \mu\text{m}$. Exposure recipe was soft contact with $30\ \mu\text{m}$ separation with exposure time of 2.1 seconds. After photoresist developing, wafers were again baked at 120°C for 30 min. to well define the patterns. With the photoresist etch mask, the silicon nitride was patterned by plasma etch with Sulfur Hexafluoride (SF_6) at an etch rate of ~ 75 nm/min for 6 minutes. Plasma etch is a physical etching process with the help of a chemical reaction for better etch rate and selectivity. During this etch, surface roughness of an unpolished wafer might prevent clearly defining patterns. Thus, DSP wafers were particularly used for accurate KOH etch mask patterning. Finally, photoresist was stripped by Piranha (1:3 mixture of $\text{H}_2\text{O}_2:\text{H}_2\text{SO}_4$), and substrates for sputtering were completed.

The second half of microfabrication occurred outside the cleanroom environment. Layers of interest were sputter-deposited with the recipes presented above following the procedure given in Section 3.1.2. After deposition, the bi-layer membranes, the film of interest (YSZ, or Pt-YSZ/YSZ/Pt-YSZ) on top of the underlying silicon nitride, were released by potassium hydroxide (KOH) etching. KOH etch is an anisotropic wet etching selective in crystal orientation. VTR dense silicon nitride works as an etch stop very well. The etch rate in (100) direction is $72\ \mu\text{m}/\text{hour}$ with the 25% KOH solution at 83°C . After released membranes were confirmed, the silicon nitride layer was plasma etched with SF_6 to release membranes just with the films of interest, at an etch rate of $21.6\ \text{nm}/\text{min}$. for 20 minutes. The wafers were diesawed

into dies. To avoid fracture of thin membranes due to the diesaw vibration and handling, a thin coat of OCG825 photoresist was sprayed over the released membranes before dicing. After the dies were successfully separated, this photoresist coating was removed with acetone.

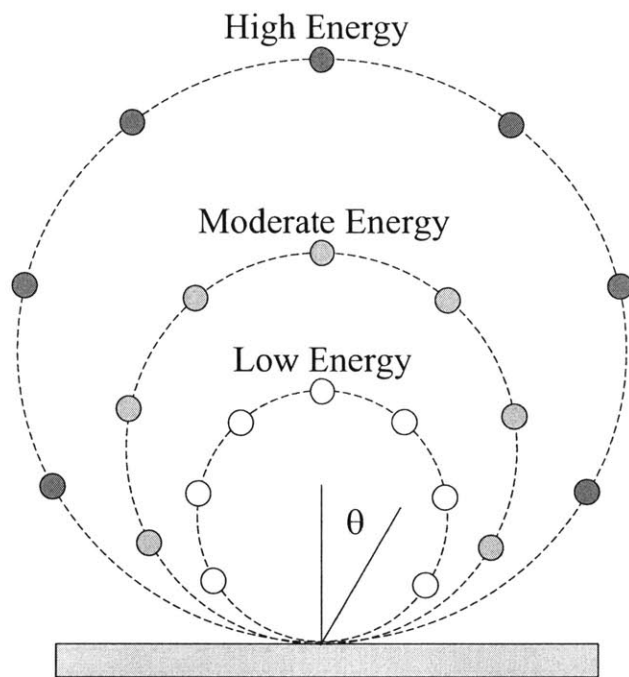


Figure 3-1: Angular emission distributions for sputtered atoms with different energies, from [1] after [3].

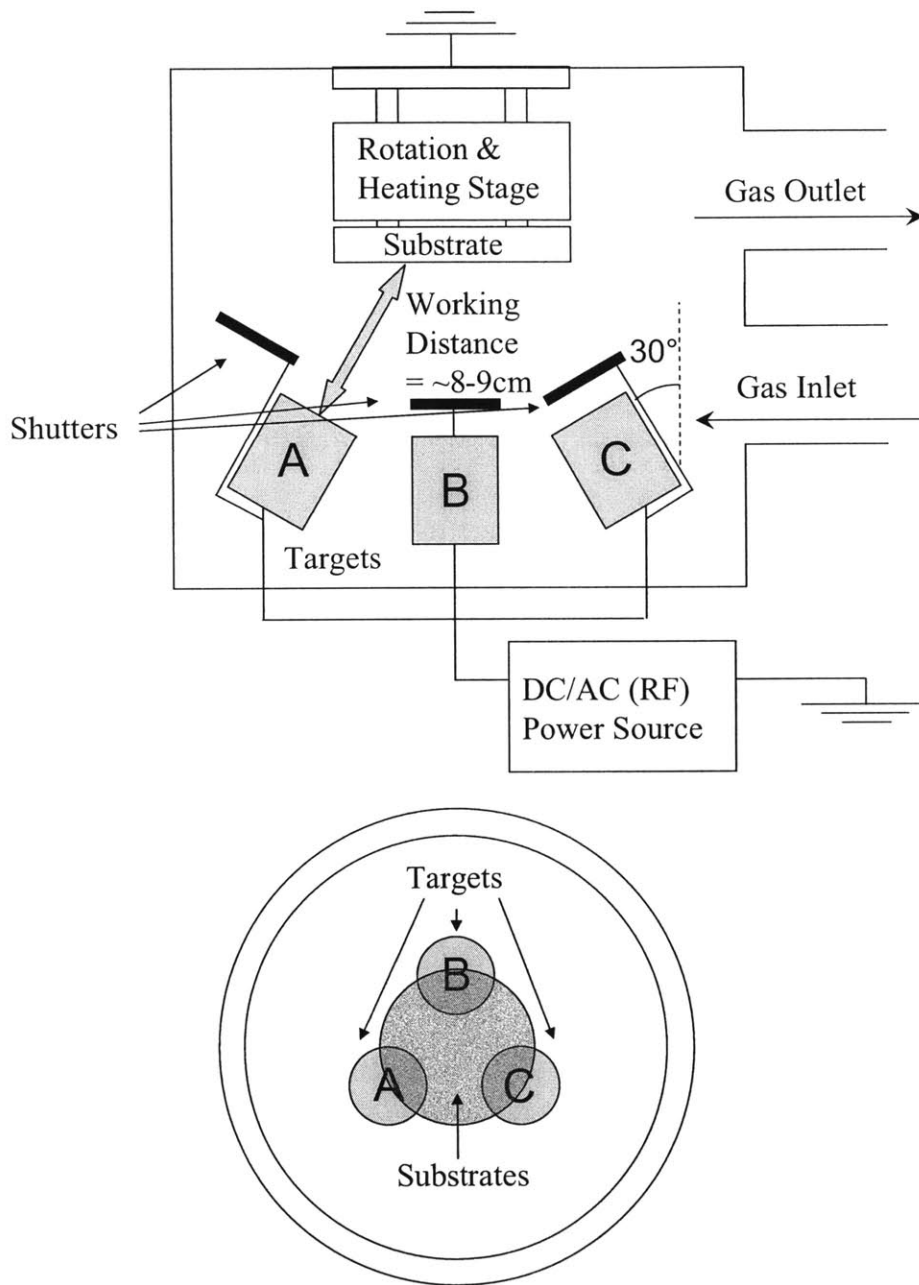


Figure 3-2: Schematic view (side and top) of Kurt J. Lesker sputtering system, modified from [1].

Film Material	Base Pressure [Torr]	Working Pressure [mTorr]	Gas Flow Ratio	Power [W]	Substrate Temp [°C]	Deposition Rate [Ang/min.]
YSZ	$< 5 \times 10^{-6}$	10	9:1 Ar/O ₂	RF 200	RT or 500	29.63
Pt	$< 1 \times 10^{-7}$	5	100% Ar	DC 50	RT	157.3
Ti	$< 1 \times 10^{-7}$	5	100% Ar	DC 100	RT	129.53
Pt-YSZ	$< 5 \times 10^{-6}$	10	9:1 Ar/O ₂	YSZ: RF150 Pt: DC 50	500	241.55

Table 3.1: Sputtering conditions and deposition rates of YSZ, Pt, Ti, and Pt-YSZ.

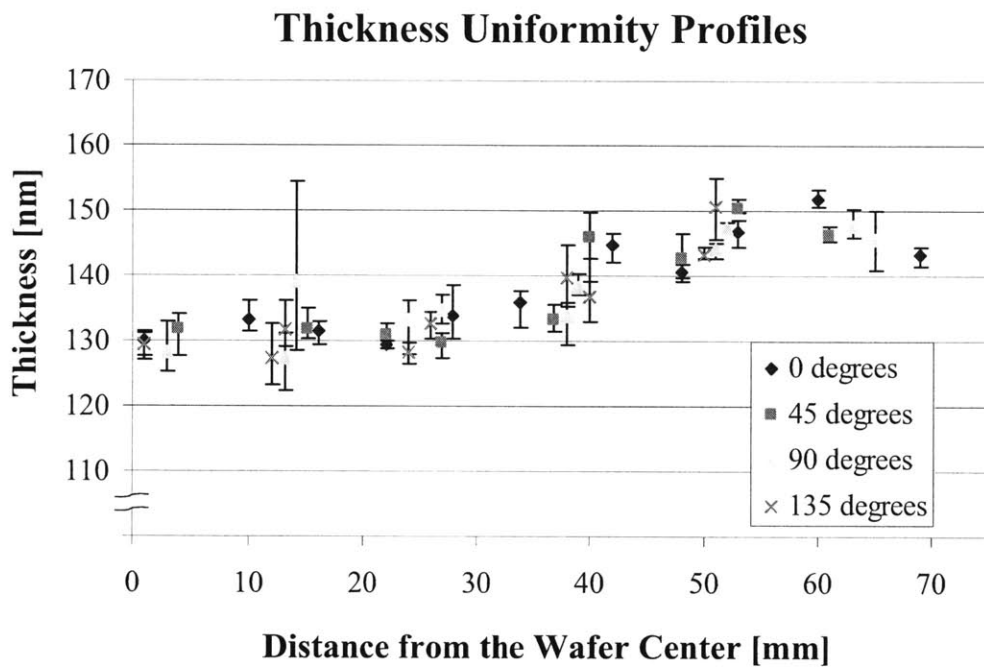


Figure 3-3: Thickness distribution of a 150-nm-thick YSZ film across a Si_3N_4 (300nm)/ Si / Si_3N_4 (300nm) wafer.

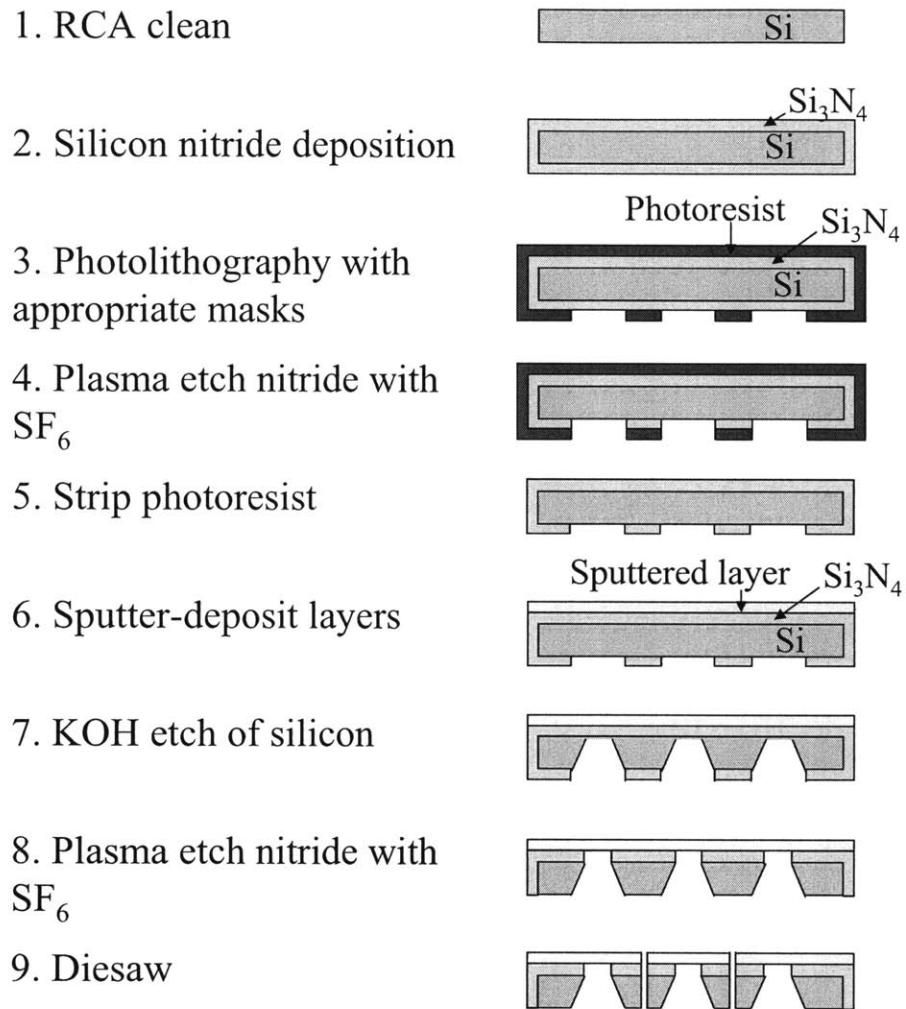


Figure 3-4: Summary of microfabrication processes for free-standing thin films.

Chapter 4

Mechanical Property

Characterization of a μ SOFC

Electrolyte

The focus of this chapter is mechanical characterization of yttria-stabilized zirconia (YSZ) in thin membrane form deposited with RF magnetron reactive sputtering. As previously pointed out many times, some properties, such as CTE and biaxial modulus, are critical to predict the mechanical behavior of thin membrane structures, and to design the thin film structure of μ SOFC in the thermomechanically stable regime. The characterization method, broadly applicable to thin-film materials property measurement, will be first described. A set of tests are performed on YSZ films, and the obtained properties will be discussed and used in the μ SOFC design in Chapter 5.

4.1 Overview of Characterization Procedure

This section introduces a series of methods to characterize critical properties of materials in thin-film form. The three properties required, at minimum, for thermomechanical stability prediction are residual stress, biaxial modulus, and coefficient of thermal expansion (CTE). Fracture stress, typically important for brittle materials, is also of interest. CTE determines membrane expansion during heating, and biaxial

modulus determines the membranes' resistance against this expansion due to fixed boundary conditions. Residual stresses are the initial offsets of the stress behavior. Thus, these three properties can be used to model behaviors of thin membranes under thermocycles to a certain extent, and help in designing stable fuel cell membranes that resist fracture.

As mentioned in Chapter 2, there are a variety of methods to acquire properties of thin films. Among them, curvature measurement (including measurement during annealing), height measurement of released buckled square membranes, and bulge testing of membranes were chosen due to the following reasons. First, this combination of methods can obtain the properties of interest. Second, the combination of bulge test and height measurement of square membranes can measure biaxial modulus regardless of the sign of the films' residual stresses. Bulge test can be used when the residual stress is tensile, and center deflection measurement of square membranes is applicable to films in compression. The residual stresses vary greatly with a slight change in fabrication parameters. Thus, flexibility to accommodate specimens of various conditions is desirable. Third, specimen fabrication is relatively simple. Wafer curvature measurement method requires only uniform films on substrates. Bulge test needs these same films to be released in a shape of rectangular membranes (including square). Square released membranes are also needed for the height-measurement tests. As illustrated in Chapter 3, fabrication of such membranes is relatively straightforward. Hardness of YSZ becomes an advantage in the plasma etch process to selectively remove solely silicon nitride in the final fabrication step. On the other hand, fabrication of cantilevers or beams is not feasible with YSZ because patterning of YSZ is extremely difficult with its high stiffness and hardness. Thus, tension tests to measure modulus [19, 20] or MEMS temperature sensor to extract CTE [74] are not suitable for YSZ and other hard ceramic films. Fourth, the chosen experimental methods are also relatively simple. Other CTE extraction methods are available as suggested by Ziebart et al. [75] involving height measurement of released membranes during annealing, but this method involves more complexity in equipment setup and measurement. Fifth, the testing structures are very close to the fuel cell stack struc-

ture. Both are released thin membranes with similar dimensions and shapes. This structural similarity and the carefully chosen testing technique allow direct measurement of properties in the correct direction (in the plane of the film), especially in terms of fracture. Although also possessing a simple testing structure, nanoindentation was not selected for characterization because its measurement of stiffness is in the wrong direction. Needless to say, the chosen methods do not require many additional fabrication steps beyond the ones for the working fuel cell devices. Last, due to similarity with the device structure, these test methods can also be used to test structures such as the fuel cell tri-layer stack which will be discussed in Chapter 5. The material characterization methods were carefully chosen for this thesis work based on the five strong points mentioned above. The theoretical underpinning of such test method will be explained in detail in the following as they appear.

The flowchart in Figure 4-1 is an illustration of the paths to complete characterization. The characterization of thin membranes starts with curvature measurement of a substrate (typically single crystal silicon as in this work) with a thin film deposited under various fabrication conditions. With Stoney's equation, curvature measurement yields the residual stress (σ_0) of the thin film. Measurement of wafer curvature continues during thermocycles, and the slope of temperature versus total residual stress gives the product of the biaxial modulus of the film and the CTE difference between the film and the substrate ("modulus-CTE" product). To evaluate the biaxial modulus and CTE separately, two other methods were introduced corresponding to the sign of the film's residual stress. For tensile membranes, bulge testing was performed, and for slightly compressive membranes, center heights of buckled membranes were measured to extract biaxial modulus. Using the extracted biaxial modulus, CTEs were calculated from the previously measured products of the two. The simple flow chart tests yield residual stress, film CTE, and film biaxial modulus as desired and shown in Figure 4-1.

This section will be followed by detailed explanations of each characterization step including theoretical background, experimental methods, and results for YSZ films with error range analysis.

4.2 Residual Stress by Wafer Curvature Measurement

Residual stresses should be carefully controlled to realize thermomechanically stable membranes. Residual stresses are directly related to the in-plane stresses in the film, and contribute to the overall stress state in the film, which determines membrane failure. With extreme tensile or compressive stresses, membranes might fail even without temperature rise. Buckling can relieve in-plane stresses through out-of-plane deflections, and this mode change occurs at different temperatures as a function of sidelength with different residual stresses. It is critical to characterize residual stress that is highly dependent on fabrication processes to avoid structural instability. In the following, the theory behind the wafer curvature measurement will be reviewed. The experimental procedures and the results, which showed excellent agreement with previous work, follows.

4.2.1 Theory and Experimental Procedures

Curvature measurement method is a widely used technique to measure overall residual stresses (intrinsic and extrinsic) of thin films deposited on well-characterized substrates. In Stoney's model [76], residual stresses are correlated with differences in the curvatures of thick, known substrates, which are initially stress-free, imposed by thin film deposition as following.

$$\sigma_0 = \frac{E_s}{1 - \nu_s} \frac{\Delta\kappa}{6} \frac{h_s^2}{h_f} \quad (4.1)$$

This relationship is true only when the following conditions hold. As for dimension, both the film and substrate thicknesses are small compared to the lateral dimensions (the wafer diameter). In addition, the film thickness should be much smaller than the substrate thickness. As for material properties, the substrate material is homogeneous, in-plane isotropic, and linearly elastic. The film material is assumed to be in-plane isotropic. The structural stiffness of the film should be much smaller than that of substrate ($E_s h_s / (1 - \nu_s) \gg E_f h_f / (1 - \nu_f)$). These assumptions can be inter-

preted that the film's thermal behavior is dominated by the substrate expansion. In terms of mechanical behaviors, axisymmetric (spherical) bending, small deflections, and uniform film thickness are assumed. Lastly, any edge effects near the perimeter are ignored. With the axisymmetric and small deflection assumption mentioned above, the curvature of a plate along a particular coordinate in the plate plane can be modeled as following.

$$\kappa = -\frac{d^2w}{dx^2} \quad (4.2)$$

In order to employ the theory and the equations expressed above, this testing requires measurement of three parameters: the substrate thickness, the film thickness, and the curvature change imposed by film deposition. The material properties of the substrate in this work, silicon, can be assumed to be well characterized. The properties of silicon varies little in the literature. In this thesis work, the biaxial modulus of silicon was assumed to be 180.5 GPa [9], and the CTE of silicon was set as $2.55 \times 10^{-6}/^{\circ}\text{C}$ [8] as summarized in Table 4.1, based on the literature work previously done to bulk silicon material with (100) orientation. These properties are assumed to be constant regardless of the temperature in this work. The substrate thickness was measured by a standard micrometer with a resolution of $10 \mu\text{m}$. At least three measurement were taken for each substrate, and the results showed a precision better than $10 \mu\text{m}$, nearly $5 \mu\text{m}$. Measurement of the film thickness was explained in Chapter 3. As mentioned previously, the thickness variation across the wafer was relatively large, as much as +19% both for 100-mm [1] and 150-mm diameter wafers across the whole wafer. Curvatures were extracted from deflection profiles of a single line along the entire wafer diameter measured by laser-scan. The profile taken before film deposition was subtracted from the one taken after deposition or after thermocycles. These profiles shaped like a parabola were curve-fitted by a second order polynomial function. Using Equation 4-2, the curvature can be extracted from an approximated profile of $w=Px^2+Qx+R$ as:

$$\kappa = -2P \quad (4.3)$$

In this research work, a Tencor 2320 Wafer Curvature Measurement System in MIT's Department of Materials Science Engineering was utilized for this profile measurement. The schematic of this machine is shown in Figure 4-2. This machine works based on the original interferometric technique developed by Rosakis [77]. The incident laser reflected from the substrate surface is cast on an optical detector, and the out-of-plane deflection of the wafer is determined by this laser spot position. Calibration of this device was done by a trained technician from the manufacturer twice, just before this research work started (April 21, 2005) and one year after (May 25, 2006). Two curvature standards made of polished mirrors of uniform curvature of 20 m and >1200 m were utilized to calibrate curvature, and the light intensity of the lasers was adjusted. Little difference in curvature measurement on the same specimen before and after the second calibration was observed. In individual measurement, a wafer was set at the center of the stage using locator rings. This secureness by the locator rings was critical to make locations of profile measurement before and after film deposition as close as possible. The wafer was leveled prior to measurement by centering the reflected laser spot (at center of wafer) on the position detector. Again, at least three curvature measurements along the same line were taken per wafer before film deposition, after film deposition, and after thermocycles. For measurement during wafer annealing, the stage, which works also as a hot plate, was covered with a silica glass plate and a metal cover to minimize thermal loss and gradient. This measurement was done in the center circular area of 135-mm diameter to give the deflection profile across the wafer. Exclusion of the wafer edges was to avoid free edge effects. The error range caused by the three measured parameters from above will be calculated accordingly in the following.

Uncertainties in the residual stress extraction are introduced from deviation from the assumptions explained above and errors in measurement. All assumptions about the dimensions and the material properties are well satisfied. The wafer diameter (~ 150 mm) is much larger than the substrate thickness (~ 600 μm), and the substrate thickness is much larger than the film thickness ($< \sim 1$ μm). The axisymmetry of the material properties can be assumed since sputtering deposition is directional

only in the wafer thickness direction. However, measured properties (substrate thickness, film thickness, and curvature change) introduce errors large enough to influence residual stress extraction. Thickness uniformity is relatively poor as explained in Chapter 3 with +19% difference between the minimum and maximum thickness. To reduce its effect on data reduction, the analysis was limited to the inner area with 40-mm radius with thickness variation of only $\pm 5\%$ for wafers with both 100-mm and 150-mm diameters. This limitation is valid for this thesis purpose because most of the pattern features, released thin membranes, are included inside the inner circular area with ~ 40 -mm radius. As for films deposited on 150-mm diameter wafers, accounting that the thickness measurement (see Section 3.1.2) was taken at a point ~ 60 mm radially away from the center (to avoid patterning areas), the thickness was first adjusted by -10% , and then its relative uncertainty was set conservatively as -15 – -5% ($\pm 5\%$). As for films deposited on 100-mm diameter wafers, accounting that the thickness measurement was taken at a point ~ 40 mm radially away from the center, the thickness was not adjusted, and the relative uncertainty was set conservatively as $\pm 5\%$. The measurement precision error of film thickness, $\pm 5\%$ was also included in this uncertainty. Thus, the data adjustment and error assessment were based on thickness measurement on each wafer sample. Meanwhile, Quinn [1] and Hertz [73] assessed data using the detailed deposition rate characterization on 100-mm diameter wafers. Although the same facility and deposition condition as theirs were utilized, the thicknesses measured in this thesis work slightly deviated from the thickness estimated with the deposition rate stated by Quinn and Hertz, most likely due to the substrate and working distance differences. The 150-mm diameter wafers used in this thesis work were held in a special holder designed, which situated the wafers closer to the target (~ 8 cm) than the 100-mm diameter wafers (~ 9 cm). Thus, in this thesis work, data adjustment and error assessment based on thickness measurement were preferred over the data analysis based on the deposition rate characterization. Other errors were from measurement of substrate thickness and wafer curvature. As discussed above, the substrate thickness measurement has a good precision ($< \sim 10 \mu\text{m}$). The total thickness variation (TTV) given by wafer suppliers

was less than $3\mu\text{m}$. Thus, a conservative estimate of substrate thickness uncertainty was assumed to be $\pm 5\%$. The relative uncertainty in curvature measurement was verified to be less than $\pm 1\%$ by Quinn [1] with 30 measurements of the same line of a wafer. Thus, again, a conservative estimate of $\pm 3\%$ was assumed. Other factors such as temperature might affect the precision and accuracy of the measurement data, but they are ignored in this thesis work assuming their effects are small. With these relative uncertainties in the measured properties listed above, the uncertainty in the calculated residual stresses of films by Stoney's equation can be calculated. The uncertainty of a function with these three variables (film thickness, substrate thickness, and curvature change) is calculated as a sum of the product of the partial derivative and the uncertainty of respective variable as shown in the following:

$$\begin{aligned} & \delta\sigma(\Delta\kappa, h_f, h_s, \delta(\Delta\kappa), \delta h_f, \delta h_s) \\ &= \left| \frac{\partial\sigma(\Delta\kappa, h_f, h_s)}{\partial(\Delta\kappa)} \right| \delta(\Delta\kappa) + \left| \frac{\partial\sigma(\Delta\kappa, h_f, h_s)}{\partial(h_f)} \right| \delta h_f + \left| \frac{\partial\sigma(\Delta\kappa, h_f, h_s)}{\partial(h_s)} \right| \delta h_s \end{aligned} \quad (4.4)$$

With the Stoney's equation, the equation above can be expanded to:

$$\begin{aligned} & \delta\sigma(\Delta\kappa, h_f, h_s, \delta(\Delta\kappa), \delta h_f, \delta h_s) \\ &= \left| \frac{E_s}{1-\nu_s} \frac{1}{6} \frac{h_s^2}{h_f} \right| \delta(\Delta\kappa) + \left| \frac{E_s}{1-\nu_s} \frac{\Delta\kappa}{6} \frac{h_s^2}{h_f^2} \right| \delta h_f + \left| \frac{E_s}{1-\nu_s} \frac{\Delta\kappa}{3} \frac{h_s}{h_f} \right| \delta h_s \end{aligned} \quad (4.5)$$

The subsequent residual stress data will be presented together with error bars estimated with the uncertainties using the equations 4-4 and 4-5.

4.2.2 Results and Discussion

The measurement and analysis given above was applied to YSZ films with various thickness ($\sim 70\text{--}600\text{nm}$) deposited at room temperature and at high temperatures (500°C and 600°C) on either bare silicon wafers of 100-mm diameter or silicon wafers of 150-mm diameter previously deposited with 300-nm-thick VTR silicon nitride, as discussed in Chapter 3. After deposition, these films were heated to 500°C at a slow ramp rate of $<2^\circ\text{C}/\text{min}$. to avoid structural microcracks due to thermal shocks,

and to allow enough time for each measurement scan every 10°C. The temperature was held at 500°C for one hour, and decreased at a similar rate. The same films, but after these thermocycles, were laser-scanned for curvature measurement. Curvefitting the parabola shaped deflection profiles across the wafer diameter was excellent with average R-squared value of 0.99. The effects of deposition temperature, thickness, and post-deposition thermocycles showed very much similar trends observed by Quinn [1] and Baertsch [16]. Overall shifting towards compressive of the stresses due to target surface condition and working distance was observed as predicted by Quinn [1]. The residual stress measurement results will be presented in the following.

The residual stresses of YSZ films deposited at room temperature on the two different substrates of eleven samples in total are summarized in Figure 4-3. Films with various thicknesses were deposited on five bare silicon wafers with 100-mm diameter, and on six silicon wafer deposited with ~300-nm thick silicon nitride with 150-mm diameter. No significant effect by the substrate difference was observed. Regardless of the substrates, the residual stresses started from ~-600MPa compressive with ~70-nm thickness, and increased up to ~-100MPa compressive until the stress reached a plateau around 250-nm thickness. This phenomena was also observed by Quinn (the stress plateau at ~300-nm thickness) [1], and can be attributed to the compressive stress mechanism of lattice distortions (atomic peening) and tensile stress evolution mechanism due to grain growth as discussed in Chapter 2.

In Figure 4-4, the stress evolution of a 87-nm thick YSZ film deposited on bare silicon substrate at room temperature is shown. In the first cycle, the stresses at first decreased with the increasing temperature due to the CTE mismatch between the YSZ and the substrate silicon. Then, a hysteretic increase in the stress was observed beginning at ~200°C. After cooling, the stress increased by ~1GPa in total. In the second cycle, a hysteretic behavior was not observed, and the film stress varied linearly only according to the CTE mismatch between the film and the substrate. The post-thermocycle residual stresses of eight samples whose thickness varied between 112-382 nm resulted in ~380MPa±100MPa tensile (see Figure 4-3). Again this residual stress shifting behavior and the independence of the final stress state from the

deposition conditions were observed previously by Quinn [1]. As Quinn suggested, this hysteresis can be explained with crystallographic phase change, migration or diffusion of interstitials, and grain growth mechanisms as discussed in Chapter 2.

YSZ films were deposited also at high temperature (500°C or 600°C) on several 150-mm diameter silicon wafers deposited with ~ 300 -nm thick silicon nitride. As shown in Figure 4-5, the as-deposited residual stresses were more compressive when compared with the residual stress states of films deposited at room temperature as shown in Figure 4-3. This tendency again coincides with Quinn's results [1]. Unlike the films deposited at room temperature, the films deposited at high temperatures have compressive residual stress, rather than tensile, after annealing.

Stress hysteresis in a high temperature deposited film of 657-nm thickness is shown in Figure 4-6. Stress hysteresis occurred at higher temperature ($\sim 400^\circ\text{C}$) with less transition ($\sim 200\text{MPa}$) than room temperature deposited films. As discussed previously in Chapter 2, annealing/cooling processes are already active when high-temperature deposited films are cooled down from the deposition temperature, and thus additional annealing has less effect.

The residual stresses and their behaviors under thermocycles studied in this thesis work showed good agreement with the results previously obtained by Quinn [1]. The only difference between the data presented above and Quinn's data is the range of residual stresses. Compared with Quinn's data set, the residual stresses of the YSZ films sputtered in this thesis work are shifted towards more compressive by $\sim 300\text{MPa}$ as-deposited, and by $\sim 200\text{MPa}$ after post-deposition annealing (both at room temperature and 500°C). Quinn observed a significant increase ($\sim +500\text{MPa}$) in stress level over time during his work over two years, and a deviation from the data by Baertsch et al. [16] who has used the same sputtering apparatus under similar conditions. Quinn attributed this difference to the bombardment energy decrease with target wear. As sputtering proceeds, the process leaves a characteristic wear mark in the shape of a "donut-ring" on the surface of the target due to the magnetron sputtering system. This uneven surface of the target increases working distance and causes a more random emission profile at oblique angles. Thus, collisions between sputtered

and reflected gas atoms are promoted, and bombardment energy is decreased, resulting in lower compressive stress generated by atomic peening mechanism [1]. In this research work, a new target with a flatter surface was introduced. In addition, when wafers of 150-mm diameter were used, the holder situated the wafers closer to the target, decreasing working distance from ~ 9 cm to ~ 8 cm. Thus, the stress state was shifted in the opposite direction (compressive) when compared with films deposited from the worn target with ~ 9 cm working distance. The residual stress data presented above support Quinn's hypothesis that the residual stresses shift more tensile as the target wears.

4.3 Modulus-CTE Product Extraction by Wafer Annealing

The CTE and Young's modulus of the films are critical in structural behavior prediction of thin membranes. Their product can be extracted by curvature measurement during annealing the samples, since CTEs determine the amount of the expansion, and Young's moduli regulate this expansion with fixed boundary condition. The relationship between these two material properties of interest and what can be measured during annealing will be explained in this section.

4.3.1 Experimental Procedures

As previously mentioned, the total residual stresses in the film on the substrate consists of two components, extrinsic and intrinsic stresses. In the following analysis, the intrinsic stress was assumed to be unchanged during annealing process. This is applicable for films (as in this work) that have been annealed and show no hysteresis in the residual stresses vs. temperature measurements. On the other hand, the extrinsic stress varies due to CTE mismatch between the YSZ and the substrate. The perfect bonding between the film and the substrate was also assumed, so the strains of the substrate and those of the film at the film-substrate interface are the same.

Again, due to very small film thickness relative to the substrate thickness, the film can be assumed to be very compliant. Thus, the substrate expands purely due to thermal expansion, and experiences no mechanical strain. The film also expands due to thermal expansion, but has to compensate for the difference in expansion amount with mechanical strains. This is where the additional stresses is introduced. The equation that equilibrates the film and substrate strains is expressed as follows:

$$\frac{1 - \nu_f}{E_f} \sigma_{thermal} + \alpha_f \Delta T = \alpha_s \Delta T \quad (4.6)$$

Thus, the slope of the temperature-residual stress plot is expressed as the product of the biaxial modulus of the film and the CTE difference between the film and the substrate as follows:

$$\frac{\partial \sigma_{thermal}}{\partial T} = \frac{E_f}{1 - \nu_f} (\alpha_s - \alpha_f) = \overline{E}_f (\alpha_s - \alpha_f) \quad (4.7)$$

In this data reduction, the variation of material properties due to temperature change were assumed to be small and were ignored.

In total, four different deposition conditions for YSZ were tested: room temperature deposition on bare silicon wafers of 100-mm diameter, room temperature deposition on silicon wafers of 150-mm diameter with 300-nm thick silicon nitride, 500°C deposition on silicon wafers of 150-mm diameter deposited with 300-nm thick silicon nitride, and 600°C deposition on silicon wafers of 150-mm diameter with 300-nm thick silicon nitride. Within the two annealing cycles, four slopes in total, two sets of heating and cooling slopes, were obtained per wafer by linear least-squares fit. In the first cycle with hysteresis, the heating slopes were taken from the initial heating slopes before the onset of the stress hysteresis.

4.3.2 Results and Discussion

The modulus-CTE calculations are averaged and summarized in Table 4.2. Some differences originating from the deposition condition were observed. In the analysis,

creep deformation mechanisms are ignored assuming its effect is small since hysteresis was not observed during the second cycles. Effects by deposition parameters such as thickness, temperature, and substrate will be discussed. The data are compared with the bulk value from literature and the results by Quinn [1]. The error ranges were not particularly pursued for this set of data because the accuracy of the data has little effect on slope measurement, and also because the linear approximation is very good with all the R-squared values better than 0.98.

The slopes were averaged among the data of films over different thicknesses. The data were too few to observe any thickness effect on the behavior. The deviation of the slope data from the average values was $\pm 20\%$, except for the slopes of the first heating cycles before the hysteresis behavior. The initial slopes showed significant differences up to $\pm 40\%$ wafer by wafer. The decrease in the data dispersion as annealing progressed can be explained with microstructure development. Microstructure evolves with heating closer to the final state that is independent of thicknesses (see Figures 4-3 and 4-5). One distinct effect by thickness was crack failure of films with thickness larger than ~ 700 nm. Normally, thin films under biaxial compression cause cracks at the interface between the film and the substrate, and the delaminated films buckles in a "wormlike" or straight pattern [78, 79, 80], with the buckling stress being a function of squared thickness. After reaching the plateau of stress state, thickness should not affect the intrinsic stress of the film as-deposited. Thus, the extrinsic stress is the only contribution to the microcrack. Impurities or dust included in the films might also have promoted propagation of these cracks.

Significant increase in stiffness was observed with increasing deposition temperature. With high temperature deposition, the microstructure increases its crystallinity as discussed in Chapter 2, and by Quinn [1] for sputtered YSZ films. Films deposited on bare silicon showed slightly higher products than those of the films deposited on silicon nitride. This difference could be attributed to errors introduced by measurements, but could possibly also be explained by crystalline orientation difference in microstructure. Quinn [1] and Baertsch et al. [16] observed the X-ray diffraction patterns of YSZ films deposited on different substrates. They employed the same

sputtering conditions with the same facility as was done in this thesis work, except that it was at room temperature. Quinn deposited YSZ films on bare silicon wafers, and observed the XRD peaks whose angle positions are comparable with those of cubic structure. However, magnitudes of the obtained XRD peaks were deviated from those of standard peaks of single crystal cubic structure. Concretely, in the XRD peaks of Quinn's film, the peak at (200) was relatively large, indicating (100) texture. Since the substrate is single crystalline, it is possible that the substrate has served as a template for crystalline growth of the deposited YSZ film. However, since the substrates were cleaned only with alcohols, the silicon substrate surface might be considered as amorphous due to native oxide layer or dust on the surface. Thus, substrate template effect cannot be verified. Meanwhile, Baertsch et al. deposited YSZ films on amorphous VTR silicon nitride, just as done in this thesis work. These films again showed the XRD peak locations compatible with those of a cubic structure. This time, a peak at (111) was much larger than a peak at (200) [16], and this magnitude range was more comparable with those of standard peaks of single crystal cubic structure. This resemblance is due to the large thickness of this film ($\sim 1 \mu\text{m}$). With this large thickness, the substrate effect is much less. This type of texture variation due to substrate difference are often observed in various combination of film and substrate in sputtering [81, 82, 83]. Although explanation of origin of crystalline orientation difference is not clear, the critical observation made from the XRD results by Quinn [1] and Baertsch [16] is that crystalline orientations of deposited YSZ is more likely to line up with (100) on silicon wafers than on VTR silicon nitride surfaces, probably due to an energy minimization. Quinn also observed peak intensification, rather than shifting of peak intensities between (100) and (111), with YSZ films deposited at high temperature or YSZ films after post-deposition annealing. Thus, although the crystallographic textures were not inspected by XRD in this thesis work, it is very likely that the films deposited on silicon nitride have a cubic structure with texture (111) just like the films deposited by Baertsch et al. [16]. This mixture of texture, or mixture of crystalline and amorphous structure can explain the decrease in the resultant modulus-CTE product in films deposited on silicon nitride, which will be

explained in more detail later in this section.

The obtained results were compared with the results by Quinn [1] who used the same facility but sputtered films on bare silicon substrates with a worn-out target. The slope values of the YSZ films deposited on bare silicon at room temperature showed higher values ($\sim 33\%$) than those given by Quinn. This may be attributed to the flatter surface of the new target or a holder for 150-mm diameter wafers that utilized in this work and decreased working distance, or just due to error range. On the other hand, all the films deposited on silicon nitride films showed slightly lower slope values both at room temperature ($\sim 2\%$) and at 600°C ($\sim 40\%$). This can be also explained by the crystalline orientation difference between the YSZ films deposited on silicon and silicon nitride.

Finally, the data was compared with the expected values based on the bulk YSZ modulus. The slope was expected to be $1.86 \text{ MPa}/^\circ\text{C}$ with the CTE and the in-plane biaxial modulus of bulk YSZ [7]. All the data values are significantly lower than the expected bulk values just like the properties measured by Quinn [1]. This difference can be again attributed to the amorphous part of the microstructure as discussed in Chapter 2, in addition to the columnar microstructure of sputtered YSZ proposed by Quinn [1].

4.4 Modulus Extraction by Square Membrane Buckling of Compressive Membranes

Young's modulus was extracted by center height measurement of buckled square membranes with slightly compressive stresses. With just enough compressive stresses, the membranes can release its in-plane stresses with out-of-plane deflections. This behavior is called buckling. As released, buckling of membranes is controlled by its stiffness and its geometrical configuration. The big advantage of this method is that the displacement to measure is relatively large and thus easier to measure than in-plane strains before buckling occurs. This extraction method is significantly

important because the 150-nm thick YSZ film deposited at 500°C, which will be used as the electrolyte layer in the fuel cell stack, are expected to have compressive stress at room temperature and at elevated operation temperature.

4.4.1 Theoretical Background

Young's modulus extraction from the center height measurement was performed on buckled square thin membranes by Ziebart et al. [84]. Three-dimensional deflection profiles of buckled square membranes were approximated through energy minimization method (EMM), and were verified with finite-element simulations (FES) and experimental work. All work was done non-dimensionally so that the extracted models are independent of materials and geometries. Square membranes were set to have built-in fixed edges with relatively small in-plane compressive residual strains and stresses. Before starting energy minimization, buckling behaviors of square membranes and thus their deflections were characterized. As exemplified in Figure 4-7, just after the first critical buckling, the deflection profile has two-axis symmetry about two perpendicular axes in the membrane plane, and rotation symmetry about the out-of-plane axis. However, after the second critical buckling, the profile loses the two-axis symmetries, but keeps only the rotation symmetry. With this observation, each symmetry was modeled by Ziebart et al. [84] with various displacement functions that consists of combination of sines and cosines. Thus the out-of-plane deflection profile and the in-plane displacement were modeled as the sum of these trial functions multiplied with unknown weighting coefficients. Due to the limitation in computational time, Ziebart et al. limited number of the functions to 8. Total energy, the sum of bending energy and in-plane deformation energy, was calculated from this deflection. The total energy was minimized by the Ritz method to obtain the unknown weight coefficients. The resulting deflection profiles were observed to be very weakly dependent on Poisson's ratio, but to be strong functions of residual strain or stress. The first critical buckling strain was also modeled by seeking for a point where the total energy ceases to be minimum in the flat state. This first critical buckling strain as shown in the following is in agreement with the analytical value

provided by Timoshenko [85]:

$$\varepsilon_{cr1} = -\frac{4.363}{1 + \nu_f} \frac{h_f^2}{a^2} \quad (4.8)$$

More than a thousand simulations were performed in the range of stresses before the second buckling with Poisson's ratio varying from 0 to 0.5 to extract a fit function of the center deflection (ω_0). The fit function is expressed as following.

$$\frac{\omega_0}{h_f} = \sqrt{\Delta\bar{\varepsilon}_0 \left(c_1 + c_2 \tanh(c_3 \Delta\bar{\varepsilon}_0) + \frac{c_4 \Delta\bar{\varepsilon}_0 + c_5 \Delta\bar{\varepsilon}_0^2}{1 - c_6 \Delta\bar{\varepsilon}_0^3} \right)} \quad (4.9)$$

where

$$\Delta\bar{\varepsilon}_0 = (\varepsilon_0 - \varepsilon_{cr1}) \frac{a^2}{h_f^2}$$

and

$$\begin{pmatrix} c_1 \\ c_2 \\ c_3 \\ c_4 \\ c_5 \\ c_6 \end{pmatrix} = \begin{pmatrix} -0.4972 & -0.2314 & -0.2128 \\ 0.0698 & 0.1625 & 0.200 \\ -7.19 \times 10^{-3} & -0.0466 & 0.0367 \\ -1.19 \times 10^{-3} & 0 & 5.51 \times 10^{-3} \\ -3.34 \times 10^{-6} & -7.43 \times 10^{-5} & 1.28 \times 10^{-4} \\ 3.16 \times 10^{-6} & 4.80 \times 10^{-6} & -1.52 \times 10^{-5} \end{pmatrix} \cdot \begin{pmatrix} 1 \\ \nu \\ \nu^2 \end{pmatrix}$$

and

$$\varepsilon_0 = \frac{1 - \nu_f}{E_f} \sigma_0$$

With this curve-fit, the normalized difference ($\Delta\bar{\varepsilon}_0$) will be first obtained. Since the first buckling strain is available as shown in Equation 1.8, the residual strain is extracted and used to calculate the biaxial modulus as desired. Ziebart et al. note that the uncertainty of the curve-fit was 0.5% over the entire simulation range. The center deflections modeled by EMM and FEM matched well with a difference of $\sim \pm 1\%$. This EMM analysis was also compared with buckling profiles of released silicon nitride square membranes. The two showed an excellent agreement in terms

of deflection symmetries, existence and position of local extrema, and deflection amplitudes. Young's moduli extracted using the curve-fit function shown above were comparable with the properties obtained from other testing method such as bulge test.

Ziebart et al. significantly improved the prediction of buckling behaviors by well characterizing deflection symmetries and by having an adequate number of deflection functions. Their analysis is expanded to calculate stresses from the deflections to ensure thermally stable membrane structures and to study failure of thin membranes later in this chapter.

4.4.2 Experimental Procedures

The design of test samples, fabrication methods, and measurement of center height will be described in the following. These experiments contained several major difficulties, and thus careful design work, fabrication tasks, and measurement were performed to extract the desired parameters successfully.

Three films were sputtered with different deposition conditions for test sample fabrication. Design of test samples needed to satisfy the first buckling mode so that the model by Ziebart et al. [84] explained above can be applied. In other words, modeling extraction via Equation 4.9 is only valid for the first (not second) buckling. Selection of deposition conditions was the key to achieve slightly compressive stresses, just enough to cause the first buckling mode at room temperature, but not enough to reach the second buckling mode. The residual stress studies in the previous section in this chapter were helpful in this selection process. Thicker films deposited at high temperature achieve slightly compressive stresses after annealing up to 500°C. Thus, thick films deposited at high temperature were selected for sample fabrication. As explained in the previous section, films thicker than ~ 700 nm cracked after one thermocycle. Thus, the largest film thickness attempted for the test samples was limited to 650nm. A wide range of sidelengths was designed to be on one die to observe the buckling evolution of membranes from flat, first buckling, to second buckling behavior. The largest membrane released using the same fabrication procedure and

facility was $1025\ \mu\text{m}$ by Baertsch et al [16], so $1025\ \mu\text{m}$ was set as the rough upper limit of sidelength. According to the first critical buckling strain and stress modeled by Ziebart et al. as shown above, the magnitude of the critical compressive stress increases with larger thickness, smaller sidelength, and larger Young's modulus. With the bulk YSZ modulus, 650-nm thickness, and $100\text{-}\mu\text{m}$ sidelength, the first critical buckling stress was calculated as $\sim 62\ \text{MPa}$ compressive, but is very likely to be lower considering the very low modulus-CTE product values of YSZ observed in the previous section. The stress range around $\sim 62\ \text{MPa}$ was targeted in the design to achieve the desired buckling mode. This condition seemed to be achievable with $\sim 600\text{-nm}$ thick films deposited at 500°C with the compressive residual stresses of $\sim 40\text{--}200\ \text{MPa}$. A sidelength range of $10\text{--}250\ \mu\text{m}$ was designed to maintain enough margin from the second buckling behavior by increasing the first critical buckling stress with smaller sidelength. The sputtering conditions of the three films are summarized in Table 4.3. One film, called sq05, was deposited at 500°C on silicon substrate covered with 300-nm thick silicon nitride. One film, called sq07, was deposited at 500°C on a bare silicon. These two films were annealed at 500°C for 1 hour after deposition. The third film, called sq06, was deposited at room temperature, and annealed only once at 300°C for 1 hour to ensure the final residual stress remains slightly compressive.

Fabrication of these test samples followed the microfabrication procedures of released thin membranes up to the KOH etch step as expressed in Chapter 3. The mask pattern to release the membranes with the desired sidelengths is shown in Figure 4-8. The circular patterns were employed to etch square membranes without any shape or size change induced by misalignment. If square patterns are used, the released membranes will be rectangular, not square, when the mask direction and substrate crystalline orientation are misaligned. However, with circular patterns, the largest distance in the crystal orientation direction between the two points in the pattern is always constant, and thus can etch squares of desirable sidelength regardless of misalignment. The diameter of the circles were designed to vary between $483\text{ to }603\ \mu\text{m}$ assuming a nominal wafer thickness of $675\ \mu\text{m}$. The vertical and horizontal lines are to separate dies as membranes are released. At first, dies were separated by diesaw

with photoresist coating as explained in Chapter 3. However, pressure caused by photoresist coating or vibration of diesaw kept breaking membranes. Utilization of KOH etch mask pattern to separate dies increased the number of survived membranes, although some membranes still broke during handling such as rinsing in water. After die separation, the backside silicon nitride was plasma etched to release just YSZ membranes. One die contained 25 membranes with square sidelength varying from $10\ \mu\text{m}$ to $250\ \mu\text{m}$. In total 32 dies are fabricated out of one wafer.

A three-dimensional surface profiler called Zygo NewView 5000 was used to measure the center deflection of the buckled membranes. This machine works based on scanning white-light interferometry. A precision vertical scanning transducer and camera together obtain a three-dimensional interferogram of the surface. The measurement control was set with objective of $10\times$, image zoom with indexed position of 1.3 or 2.0, and measurement array of 640×480 at 7 Hz. The system has stated vertical resolution of 0.1 nm, and step height accuracy of $<3\%$ [86]. The stage was tilted to promote interferometry on the nearly transparent YSZ films. The profiles were sometimes distorted by interference due to the silicon substrate. This distortion and the tilt observed in the data were corrected in the process for center height extraction. Three measurements were taken for each membrane, and were averaged.

Finally, other parameters of the membrane structures required for this modulus extraction analysis were measured. The film thicknesses were measured using the the Tencor P10 profilometer as explained in Chapter 3 at the position radially $\sim 60\ \text{mm}$ away from the wafer center. The thickness was again adjusted by -10% to compensate for thickening towards the wafer edges. The square sidelengths were measured from the picture images taken with a $10\times$ microscope. The square sidelengths were measured on the image, and thus the resolution was governed by the pixel on the screen. After taking several measurements on the same sidelength, the precision errors was observed to be $\sim \pm 3\%$. The residual stresses were measured again by curvature measurement, and the modulus-CTE products were obtained from the slope of the temperature-residual stress plots as described in the previous section.

The error range of the extracted Young's modulus was calculated using the uncer-

tainties. Since an analytical solution of the Young's modulus was not available in this analysis, the following method was taken to calculate the error range. To estimate the minimum Young's modulus, the largest normalized deflection in the error range was taken. In a similar way, the smallest normalized deflection in the error range was used to extract $\Delta\bar{\epsilon}_0$ for the maximum Young's modulus. Once the $\Delta\bar{\epsilon}_0$ is extracted, the Young's modulus can be obtained using the following expression:

$$E_f = \frac{1 - \nu_f}{\Delta\bar{\epsilon}_0 - \frac{4.363}{1 + \nu_f}} \frac{E_s}{1 - \nu_s} \frac{1}{6} \frac{\Delta\kappa h_s^2 a^2}{h_f^3} = M \frac{\Delta\kappa h_s^2 a^2}{h_f^3} \quad (4.10)$$

where

$$M = [Constant] = \frac{1 - \nu_f}{\Delta\bar{\epsilon}_0 - \frac{4.33}{1 + \nu_f}} \frac{E_s}{1 - \nu_s} \frac{1}{6}$$

Thus, the traditional estimation of uncertainty can be finally used to calculate the error range of the Young's modulus of the film as a sum of the products of the partial derivative and the uncertainty of respective variable as shown in the following:

$$\begin{aligned} & \delta E_f(\Delta\kappa, h_s, h_f, a, \delta(\Delta\kappa), \delta h_s, \delta h_f, \delta a) \\ &= \left| \frac{M h_s^2 a^2}{h_f^3} \right| \delta(\Delta\kappa) + \left| \frac{2M \Delta\kappa h_s a^2}{h_f^3} \right| \delta h_s + \left| \frac{2M \Delta\kappa h_s^2 a}{h_f^3} \right| \delta a + \left| \frac{3M \Delta\kappa h_s^2 a^2}{h_f^4} \right| \delta h_f \end{aligned} \quad (4.11)$$

The uncertainties of the five parameter (center deflection of buckled square membranes, curvature difference, film thickness, square sidelength, and substrate thickness) were estimated as following. As set previously for the error range calculation for the residual stress measurement, conservative uncertainties estimation of curvature difference, film thickness, and substrate thickness were $\pm 5\%$, $-15 - -5\%$ ($\pm 5\%$), and $\pm 5\%$ respectively. The uncertainty of center deflection of buckled square membranes was set as $\pm 5\%$ based on the specification stated in the Zygo manual and on data dispersion observed experimentally. The uncertainty of the sidelength were calculated as $\pm 3\mu\text{m}$. The error ranges were expected to be large, and will be presented together with the results in the following.

4.4.3 Results and Discussion

Young's modulus for each wafer was extracted from membranes released successfully. Some membranes broke due to handling. The sidelength of the membranes turned out to be larger ($\sim 50\text{-}400\mu\text{m}$) than designed, because of substrate thickness variation and overetch of the substrate in KOH solution. Larger sidelength reduces the first and second critical buckling stress, and thus more membranes showed second buckling than desired. Only one to eight membranes per each die turned out to be in the first buckling mode. Thus in total $\sim 20\text{-}30$ membrane samples per wafer were in the first buckling mode. In this extraction, the Poisson's ratio was fixed at 0.2 [7], but the effect of this fixed value on the extracted modulus was expected to be small [84].

The extracted Young's modulus values varied much between dies from the same wafer. This large dispersion was expected due to relatively large errors introduced to the analytical model by measured values. Among them, film thickness was the largest error factor ($\sim 50\%$ of total error range). To better interpret the data, extracted Young's modulus were sorted according to each die, considering that the thickness variation on one die ($15\text{ mm}\times 15\text{ mm}$ square) is very small relative to thickness variation across the wafer. The locations of dies from the wafer sample sq06 were recorded and thus the data was sorted by the radial length from the center of the wafer to the dies. The data taken from the points radially away from the wafer center by more than 40-mm were eliminated to exclude the error introduced by sharp thickness increase at the wafer edge. As for the other two wafer samples (sq05 and sq07), the locations were not recorded and thus the data were sorted by dies, but none of the data were eliminated. These plots for the samples sq05, sq06, and sq07 are shown in Figure 4-9, 4-10, and 4-11. In Figure 4-10, the extracted Young's modulus showed the tendency to increase as the radial distance of the die location increases. This expected modulus deviation is due to the thickness non-uniformity. The thickness used in calculation is the one calibrated by -10% from the thickness measured at $\sim 60\text{mm}$ away from the wafer center. However, the dies from the area $\sim 60\text{mm}$ away from the wafer center have the thickness larger than this calibrated value. The Young's

moduli of the films on these dies were re-calculated with the measured thickness (369 nm) and the residual stress (-36 MPa) calculated with this measured thickness. As shown in Figure 4-12, the Young's moduli decreased, correcting the increasing trend of Young's moduli towards the wafer edges. In this way, the decreasing tendency of Young's modulus towards the center of the wafer can be explained. The plots of the dies from the other two wafers (sq05 and sq07) can be interpreted in the same way, although this interpretation can not be confirmed because radial locations of these dies were not recorded.

The averaged extracted Young's modulus is summarized in Table 4.4. The data deviated from these averaged values by ~ 5 -300%, which was large as expected. Even with these data without much accuracy, still two major trends were observed. First, the CTE extracted did not vary much regardless of the rather large variation in the extracted slope of temperature-residual stress plot and the extracted Young's moduli, showing little dependence on microstructure. The effects of thin film microstructure on CTE has been studied by several groups. Films normally contain amorphous and crystalline phases in its structures. Even with fully crystalline structures, amorphous parts can be observed at the grain boundaries [87]. These phase differences, and cavities or porosities often contained in the structure could affect CTEs [87, 88]. Crystal orientations can also affect CTEs, but this effect should not be significant in randomly-oriented microstructure [88]. CTE variation due to microstructures were experimentally studied, but the results varied from material to material [88, 89, 90, 91]. Takimoto et al. studied hydrogenated amorphous and microcrystalline silicon films deposited by CVD, and observed little dependence of CTE on microstructure [90]. Wan et al. also observed little dependence of CTEs on grain size or grain aspect ratio with YSZ at 300–1473K temperature range [88]. Even with relatively large error range in this experimental work, the CTE of sputter-deposited YSZ films appeared independent of microstructure. Accordingly, these relatively constant CTEs leave the Young's moduli varying in proportion to the "modulus-CTE" products. The extracted Young's modulus showed a clear increasing tendency with higher deposition temperature, which effect can be explained by crystalline growth.

Second, the extracted Young's moduli, even the ones of the films deposited at high temperatures, are much lower than that of bulk YSZ. Various groups have tried to characterize YSZ stiffness. The modulus of YSZ given by Ashby [7], 200GPa, was obtained from experimental testing on the bulk YSZ. Ingel and Lewis [58, 59], and Kandil [58] well characterized the cubic YSZ with yttria concentration of 3.9 mol%. They were able to extract the cubic single crystal YSZ stiffness (C) and compliance (S) matrices as follows:

$$C = \begin{pmatrix} c_{11} & c_{12} & c_{12} & 0 & 0 & 0 \\ c_{12} & c_{11} & c_{12} & 0 & 0 & 0 \\ c_{12} & c_{12} & c_{11} & 0 & 0 & 0 \\ 0 & 0 & 0 & c_{44} & 0 & 0 \\ 0 & 0 & 0 & 0 & c_{44} & 0 \\ 0 & 0 & 0 & 0 & 0 & c_{44} \end{pmatrix} = \begin{pmatrix} 410 & 110 & 110 & 0 & 0 & 0 \\ 110 & 410 & 110 & 0 & 0 & 0 \\ 110 & 110 & 410 & 0 & 0 & 0 \\ 0 & 0 & 0 & 55 & 0 & 0 \\ 0 & 0 & 0 & 0 & 55 & 0 \\ 0 & 0 & 0 & 0 & 0 & 55 \end{pmatrix} [GPa] \quad (4.12)$$

$$S = \begin{pmatrix} s_{11} & s_{12} & s_{12} & 0 & 0 & 0 \\ s_{12} & s_{11} & s_{12} & 0 & 0 & 0 \\ s_{12} & s_{12} & s_{11} & 0 & 0 & 0 \\ 0 & 0 & 0 & s_{44} & 0 & 0 \\ 0 & 0 & 0 & 0 & s_{44} & 0 \\ 0 & 0 & 0 & 0 & 0 & s_{44} \end{pmatrix} = \begin{pmatrix} 27.5 & -5.82 & -5.82 & 0 & 0 & 0 \\ -5.82 & 27.5 & -5.82 & 0 & 0 & 0 \\ -5.82 & -5.82 & 27.5 & 0 & 0 & 0 \\ 0 & 0 & 0 & 180 & 0 & 0 \\ 0 & 0 & 0 & 0 & 180 & 0 \\ 0 & 0 & 0 & 0 & 0 & 180 \end{pmatrix} [10^{-4} \frac{1}{GPa}] \quad (4.13)$$

Hill [92] set the bounds for Young's modulus and Poisson's ratio for the randomly oriented, fully crystallized, polycrystalline structure. The bounds for YSZ biaxial modulus in the specified microstructure were calculated as 285-370 GPa [1]. Crystallographic texture influences the structural stiffness. Nye [61] presents a method to transfer a compliance matrix in one direction to that in a desired direction. Using this transformation, Young's moduli in the desired direction and in the direction perpendicular to that direction are calculated as follows:

$$\frac{1}{E_i^*} = s_{11}^* = s_{11} + 2\left(\frac{1}{2}s_{44} + s_{12} - s_{11}\right)(l_1^2 m_1^2 + l_1^2 n_1^2 + m_1^2 n_1^2) \quad (4.14)$$

$$\frac{1}{E_t^*} = s_{12}^* = s_{12} - \left(\frac{1}{2}s_{44} + s_{12} - s_{11}\right)(l_1^2 l_2^2 + m_1^2 m_2^2 + n_1^2 n_2^2) \quad (4.15)$$

where the unit vectors of the <100> axis system, \mathbf{e}_1 , \mathbf{e}_2 , and \mathbf{e}_3 , are expressed in terms of the unit vectors of the new axis system after rotation, \mathbf{u}_1 , \mathbf{u}_2 , and \mathbf{u}_3 as following:

$$\mathbf{e}_1 = l_1 \mathbf{u}_1 + l_2 \mathbf{u}_2 + l_3 \mathbf{u}_3$$

$$\mathbf{e}_2 = m_1 \mathbf{u}_1 + m_2 \mathbf{u}_2 + m_3 \mathbf{u}_3$$

$$\mathbf{e}_3 = n_1 \mathbf{u}_1 + n_2 \mathbf{u}_2 + n_3 \mathbf{u}_3$$

As described in Chapter 2, Quinn [1] observed (100) orientation in YSZ films sputtered at room temperature with XRD. Thus, the Young's modulus and Poisson's ratio in the out-of-film-plane direction of YSZ crystalline structure with (100) texture was estimated as 363.4 GPa and 0.212 using $(l_1, l_2, l_3)=(1, 0, 0)$, $(m_1, m_2, m_3)=(0, 1, 0)$, and $(n_1, n_2, n_3)=(0, 0, 1)$. Accordingly, the biaxial modulus in the in-plane direction was calculated as 461 GPa. Meanwhile, the films deposited on silicon nitride are believed to have texture of (111) rather than (100) in this thesis work. Thus, the stiffness matrices expressed in the equation above is originally aligned in (111) direction. To obtain the the Young's modulus and Poisson's ratio in the out-of-film-plane direction, the compliance matrix needs to be transferred to the (100) direction. The transformation should be performed with $(l_1, l_2, l_3) = (1/\sqrt{3}, 1/\sqrt{3}, 1/\sqrt{3})$, $(m_1, m_2, m_3) = (1/\sqrt{3}, -1/\sqrt{3}, 1/\sqrt{3})$, and $(n_1, n_2, n_3) = (-1/\sqrt{3}, 1/\sqrt{3}, 1/\sqrt{3})$. The calculated Young's modulus and Poisson's ratio in the film plane are 153.17 GPa and 0.378. The biaxial modulus in the in-plane direction was calculated as 246.25 GPa, which is much lower than 461 GPa calculated for the (100) orientation. Thus, this explains why modulus-CTE products, and thus moduli, of films deposited on silicon nitride with (111) orientation are lower than those of films deposited on bare silicon by Quinn [1] with (100) orientation. Mixture of orientations of (111) with (100) lowers the modulus due to lower stiffness in the in-plane direction due to lower stiffness of crystalline structure with (111) orientation. In addition, mixture of texture inevitably introduces grain boundaries, which again lowers the stiffness. The difference between

these extracted Young's moduli and the high bulk YSZ moduli is explained by the YSZ films' microstructure with mixed phases. The microstructure of the deposited films consists of the amorphous regions threading through the crystalline structures, and its structure is illustrated in Figure 4-13 [1]. The low measured in-plane stiffness relative to bulk can be attributed to the grain boundaries and amorphous regions.

4.4.4 Implications for Design of Thermally Stable Thin Membranes

The design of thermomechanically stable YSZ films with sputtering conditions used in this work became somewhat easier with the residual stress studies and the rough evaluation of Young's modulus and CTE obtained from above. The key for the structural ability is to keep in-plane stresses under the fracture stresses. The in-plane stresses of the film with compressive stresses can be modeled by expanding the square buckling membrane analysis by Ziebart et al. presented above. The stress state under annealing to 600°C was calculated to ensure the fuel cell stack membranes will survive without any fracture caused by stress concentrations. The in-plane stress calculation method, the in-plane stresses for YSZ calculated with the properties obtained above, and experimental verification of these analytical results will be presented in the following. The analytical work portion was based on the original work by Wicks [93].

The in-plane stresses of thin films under thermocycles were calculated with von Karman nonlinear plate theory. Strains were assumed to be small, and normals to the middle surface were assumed to be always normal. Following Ziebart's process as expressed above, the deflection and the in-plane displacements of membranes were again modeled as a sum of the trial functions that satisfy the observed symmetry of buckled square membranes. Due to the calculation time limitation, the number of trial functions was reduced from 8 by Ziebart et al. to 3. Ziebart et al. [84] included both the deflection with the axes and rotation symmetries and the deflection function with skew reflection symmetries, but the latter was eliminated in this analysis for

again the computation time limitation and to consider only first buckling. The trial displacement functions used in this work are as follows:

$$g_{mn}^s(x, y) = (\cos 2m\pi \frac{x}{a} - (-1)^m)(\cos 2n\pi \frac{y}{a} - (-1)^n) + (\cos 2n\pi \frac{x}{a} - (-1)^n)(\cos 2m\pi \frac{y}{a} - (-1)^m) \quad (4.16)$$

where

$$m, n = 1, 2, 3$$

After setting these displacements, plate theory was introduced to calculate strains:

$$\varepsilon_{xx} = u_{,x} - zw_{,xx} + \frac{1}{2}w_{,x}^2 \quad (4.17)$$

$$\varepsilon_{yy} = v_{,y} - zw_{,yy} + \frac{1}{2}w_{,y}^2 \quad (4.18)$$

$$\varepsilon_{xy} = \frac{1}{2}(u_{,y} + v_{,x}) - zw_{,xy} + \frac{1}{2}w_{,x}w_{,y} \quad (4.19)$$

The total strains are calculated as the sum of these strains shown above, the thermal strains introduced by temperature rise, and the residual strains.

$$\varepsilon_{total} = \varepsilon + \varepsilon_{thermal} + \varepsilon_0 \quad (4.20)$$

with

$$\varepsilon_{thermal} = -\alpha_f \Delta T$$

$$\varepsilon_0 = -\sigma_0 \frac{1 - \nu_f}{E_f}$$

With these strains, the total energy for this film was calculated with the total strain energy as following.

$$U = \int \int \int \frac{1}{2}(\sigma_{xx}\varepsilon_{totalxx} + \sigma_{yy}\varepsilon_{totalyy} + 2\sigma_{xy}\varepsilon_{totalxy})dxdydz \quad (4.21)$$

Minimization of this strain energy was performed to obtain the unknown weight coefficients of the trial functions that model the displacement. Obtained displacement profiles are now only a function of temperature rise. With each temperature rise, the

displacements, and thus strains and stresses, at any point inside the thin membrane are obtained. The maximum (tensile) and minimum (compressive) stresses were obtained as the extreme stresses that the film experiences. These values are compared with the fracture stresses of the YSZ thin films deposited with the same facility observed by Quinn [1]. With the limited amount of the trial functions, the stresses calculated were not as accurate as the original Ziebart's analysis. The results here were primarily used to observe trends.

Two different YSZ film conditions were analyzed with the model explained above to help design thermomechanically stable membranes at high μ SOFC operation temperatures. Thus, the film condition was chosen to be as close as the one for the fuel cell stack deposition, such as deposition temperature of 500°C. Thickness was chosen to be 150nm and 250nm, because films with 125-nm thickness were the smallest thickness deposited, and experimentally confirmed to be continuous. Smaller thickness was more desirable for better ionic conductivity. However, thin membranes have less possibility to survive handling during fabrication. Thus, the film with 250-nm thickness was also explored. The properties required in the analysis were obtained in the previous sections. One major difference between the YSZ membranes investigated above and the fuel cell electrolyte YSZ membranes is that the SOFC electrolyte is sandwiched by the anode and cathode Pt-YSZ layers. Again, the effects of these two layers on the mechanical behavior of YSZ were assumed to be small and ignored because the anode and cathode are often porous and therefore very compliant. The substrate difference should not affect residual stress as observed earlier, but will have a small influence on the stiffness. The residual stress of films after thermocycles was set as ~ -300 MPa compressive as experimentally observed. The stiffness and CTE of these films were set to be 106.92 GPa and $10.20 \times 10^{-6}/^{\circ}\text{C}$, from the measured properties of YSZ films deposited on silicon substrate at 500°C. With this higher value of Young's modulus and CTE among the obtained property results, the magnitude of the in-plane stresses increases, and thus a conservative analysis is obtained. The temperature rise was set at 600°C, the likely operation temperature. The maximum and minimum stresses were calculated for the films with 150-nm and 250-nm thickness

over the sidelength ranging between 0.5 to 200 μm .

The extreme stresses in the film calculated are shown in Figures 4-14 and 4-15, respectively, for the films with 150-nm and 250-nm thickness. The stresses can be categorized into three regions depending on the membrane sidelength. In the first region with very small sidelengths ($\sim 0.5\mu\text{m}$), only compressive stresses are observed, when no buckling was predicted. As sidelength increases ($\sim 0.5\text{-}50\mu\text{m}$), membranes buckle and reach their maximum stresses that are probably large enough to cause membrane breakage. With further increase in sidelength ($>\sim 50\mu\text{m}$), the stresses decrease down to $\sim 400\text{MPa}$ and plateau. This $\sim 400\text{MPa}$ is satisfactorily smaller than the fracture stress of 710-750MPa observed by Quinn [1]. Thus, for thermally stable structure, sidelength needs to be either less than $\sim 0.5\mu\text{m}$ or larger than $50\mu\text{m}$. Precise control of small sidelength was experimentally confirmed to be difficult in the previous section. In addition, greater released membrane areas are desirable so that the power output can be large enough to measure. Thus, the sidelength of the fuel cell stacks were determined to be $100\mu\text{m}$ and $200\mu\text{m}$ so that the in-plane stresses will be small after the substantial stress drop due to buckling. The thermomechanical stability of the tri-layer stacks with YSZ electrolyte of 150-nm and 250-nm thick was experimentally observed during the development of power test structure, and will be discussed in Chapter 5.

4.5 Young's Modulus Extraction by Bulge Test on Tensile Membranes

Extraction of Young's modulus from films with tensile residual stresses will be explained in the following. While the stiffness extraction from the square buckled membranes expressed above is limited to films with compressive stress, the bulge test is applicable only to films with tensile stress. Unlike the method in the previous section that limits the compressive stress in the first buckling mode range, the bulge test allows any tensile stress range as long as the stresses do not fail the released membranes

before completion of the bulge test. The theory behind the bulge test, the design and fabrication of bulge test samples, and the preliminary results will be discussed in the following.

4.5.1 Theoretical Background

Bulge tests produce pressure-center deflection plots of released thin membranes, and stress-strain curves can be derived from these measurements. With the great progress in microfabrication methods, accurate data acquisition has become easier with precisely controlled dimensions and reduced sample handling. Bulge test has been studied by various researchers since Beams [94] first established the test type. Circular, square, and rectangular membranes have been studied mostly with energy minimization methods [95, 96, 97]. Our interest here is the biaxial modulus extraction from thin films with tensile residual stresses. Vlasaak and Nix [95] have investigated this particular case with rectangular membranes based on the approach originally developed by Timoshenko [97]. Just like other researchers, Vlasaak and Nix assumed plane strain, and thus film stresses and strains are assumed to be distributed uniformly across the membrane width. Displacements were approximated as functions that satisfy the boundary conditions of four fixed edges. Assuming tensile residual stresses, the applied pressure was divided into two parts. The first pressure, q_1 , to balance the tensile residual stress (prestress), and the second pressure, q_2 , to stretch the membranes. The first pressure q_1 is modeled as a function of the center deflection of the membranes. The second pressure q_2 can be also modeled by minimizing the strain energy. Bending energy was neglected in calculation because its effect is significant only close to the edges, and is negligible everywhere else especially with large deflections [95]. The coefficients of these functions converge as in the following equation with increasing aspect ratio of the rectangular sidelengths.

$$q = q_1 + q_2 = \frac{8\sigma_0 h}{a^2} w_0 + \frac{64}{3(1 + \nu_f)} \frac{E_f h_f}{a^4(1 - \nu_f)} w_0^3 \quad (4.22)$$

This model can be used as an approximation for rectangular samples with aspect ratio larger than four [95]. This analysis is observed to be very sensitive to geometry, and requires accurate measurement of the rectangular width. Initial height measurement before starting pressure application to the films is also critical [98]. This analysis and its accuracy was confirmed with FEM and experiments [95].

Testing samples sometimes require two layers, a film of interest and a film that structurally supports the film of interest. As long as both films deform elastically, the constitutive function is valid whether the film is freestanding or part of a bi-layer. Thus, pressure required to deflect just the film of interest can be acquired by subtracting the pressure-deflection curve of a free standing supporting layer from that of the bilayer. One last thing to be noted is that this analysis can be applied only for elastic deformation with tensile residual stresses. For plastic behavior characterization, FEM is necessary [99].

4.5.2 Sample Fabrication and Experimental Procedures

Bulge testing was performed at the test setup situated at Thin Films Mechanics Laboratory at Harvard University. The schematic of the bulge test apparatus is given in Figure 4-16. Samples were clamped on top of the cavity of water container, and sealed with grease and mechanical loading. Pressurization of membranes was done by water, and was controlled by a stepper motor with a resolution of 0.1 kPa. The achievable maximum pressure was 200kPa. The center deflection of the membranes was measured by a laser interferometer with a He-Ne laser light source. A photosensitive resistor detects the interference pattern, and each intensity peak corresponds to a deflection of 316.5 nm, which is equal to half the wavelength of the light. The pressure was controlled and recorded with a LabView data acquisition system during the test.

The testing samples were designed as following. First, limitations imposed by the test setup were considered. The light interferometer requires relatively large membranes, at least a width larger than 1 mm. Thus, the length needed to be at least 4 mm to use the approximate analysis for long rectangular membranes expressed

above. A mono-layer of YSZ with this large area was tried to be released, but all membranes broke during cleaning process after KOH etch. Due to the YSZ's fragility, an underlying layer to support the YSZ membranes were required so that membranes can survive handling during fabrication. Thus, the structure of the bulge test samples used in this thesis work was a bi-layer of YSZ and VTR silicon nitride (300-nm thickness). This silicon nitride layer was confirmed to have tensile residual stress of ~ 200 MPa.

Fabrication of samples followed the processes explained in Chapter 3. The silicon nitride mask pattern is given in Figure 4-17. Various sizes of membranes from $\sim 1\text{mm} \times \sim 3\text{mm}$ to $\sim 2\text{mm} \times \sim 10\text{mm}$ were designed to be released. Again, the lines to separate dies during the KOH etch process were included in the patterns. Diesawing of dies was not an option in this sample fabrication due to the membrane fragility. After nitride patterning with this chrome mask, a YSZ film was deposited at room temperature to ensure tensile stress after post-deposition thermocycles. Thinner membranes (~ 100 nm) were desirable to regulate this tensile residual stress small enough to avoid membrane failure, and also to promote large deflections for easy measurement. After membranes were released by KOH etch, the nitride layer was maintained (not etched) so that the nitride layer can support the fragile YSZ membranes. Most membranes survived releasing, but a few broke during the subsequent diesaw process.

4.5.3 Results and Discussion

Due to time limitation, only one data point was taken for this thesis work with the assistance of Xiang at Harvard. The YSZ film of 125-nm thickness was deposited at 500°C with 472 MPa tensile post-annealing residual stress. This layer was supported with ~ 300 -nm-thick VTR silicon nitride layer. The membrane area was $\sim 2\text{mm} \times \sim 10\text{mm}$. The applied pressures were cycled three times, first up to 50kPa, second to 90kPa, and third to 150kPa. The stress-strain and pressure-deflection slopes on this bi-layer film are presented in Figure 4-18. The membrane's behavior was elastic regardless of stress loading and unloading up to ~ 1300 MPa for the bi-layer film. Similarly, a VTR silicon nitride layer of ~ 300 -nm thickness was bulged up to 90 kPa.

The stress-strain plots were subtracted to produce the stress-strain plot of the YSZ membrane. Assuming Poisson's ratio of YSZ as 0.2, the extracted Young's modulus was 161 GPa for the bi-layer of silicon nitride and YSZ, while Young's modulus for the nitride layer was measured as 153 GPa. The YSZ Young's modulus was found to be 168 GPa, higher than the extracted modulus of room temperature deposited YSZ films from the square buckling test (24 GPa), but still lower than the bulk value (200 GPa). However, this data contains significant error sources. One very noticeable error is the residual stress of YSZ films, which was measured as 472 MPa by wafer curvature, was calculated as 528 MPa. First, membranes dimensions of the two samples were assumed to be the same, but were slightly different from each other due to substrate thickness difference in KOH process. The thicknesses of silicon nitride on both dies were also slightly different, too. YSZ thickness measurement might not have been accurate enough, or might not have been uniform across the dies. Last, the silicon nitride layer was roughly three times thicker than the YSZ layer, reducing the accuracy of the data. The bi-layer Young's modulus (161 GPa) and the silicon nitride Young's modulus (153 GPa) were apparently equal, indicating that a compliant (as expected) YSZ layer contributes little to the bi-layer stiffness. The first two error sources could have been avoided if YSZ could have been selectively etched from the bi-layer die to produce just the nitride-layer membrane. However, this was not possible due to the hardness of YSZ.

4.6 Comparison of Measured YSZ Material Properties

Using the two different method (measurement of square buckled membranes, and bulge test), Young's moduli of sputter-deposited YSZ films were obtained. However, these two sets of data were not directly comparable, because as frequently observed by now, stiffness properties of YSZ highly depend on the films' fabrication processes. The extracted Young's modulus from bulge test of films deposited at room temperature

(167 GPa) turned out to be much higher than the one obtained by square buckling membranes (24 GPa and 64 GPa). Considering that the bulge test die used was located relatively closer to the rim and the error sources mentioned in the previous section, the values were assumed to be in the large error range.

Overall, the material properties of YSZ films deposited in this thesis work (24~167 GPa) were confirmed to be lower than that of the bulk YSZ (200 GPa) by $-88\text{--}-17\%$. Just with Young's modulus extracted from center deflection measurement of square buckled membranes, this result was hard to confirm due to its large error range.

4.7 Conclusions

In this chapter, three material properties (residual stress, Young's modulus, and CTE) were obtained to help in designing thermomechanically stable thin membrane structure for μ SOFC.

The residual stresses and their variation due to the deposition condition were well characterized with an acceptable error range. The residual stresses of the films deposited at room temperature starts compressive ($\sim -600\text{MPa}$) in thinner films, but converge to $\sim -380\text{MPa}$ after the large hysteretic behavior in thermocycles regardless of the deposition condition. The residual stresses of films deposited at higher temperature (500-600°C) were also well characterized, and tended to be more compressive which is attributed to the atomic peening effect. The difference from the previous data by Quinn [1] was observed because of the difference in a target surface condition. Little effect was observed by substrate difference (silicon and silicon nitride).

Modulus-CTE products were measured from the slope of temperature-residual stress plot by annealing wafers deposited with films. These values were highly dependent on the deposition conditions, and this variation can be attributed to the microstructure variation due to the deposition conditions. The bulk values were two or ten times higher than film YSZ values.

The Young's moduli of YSZ films were extracted from two different methods: bulge test for tensile films, and center deflection measurement of square buckled membranes

for slightly compressive films. The residual stress studies above were used to design appropriate samples for the two tests. The extracted Young's moduli again depended significantly on the deposition conditions. The extracted moduli (24 to 167 GPa) were much lower than the bulk values estimated by the literature (200 GPa). This tendency is due to the mixture of amorphous and crystalline phases in the columnar structure of the YSZ films deposited in this thesis work. CTEs were extracted from the modulus-CTE products and the Young's moduli. The CTEs were independent of fabrication process and were consistent with the bulk value.

Even with relatively large errors, an approximate set of material properties were obtained for the design work of μ SOFCs. A nonlinear in-plane stress analysis will be utilized to set the preliminary deposition conditions and geometric conditions based on a maximum stress failure criteria, including design in the postbuckling regime. The validity of these studies will be examined in the next chapter, through the actual fabrication of working μ SOFC membranes.

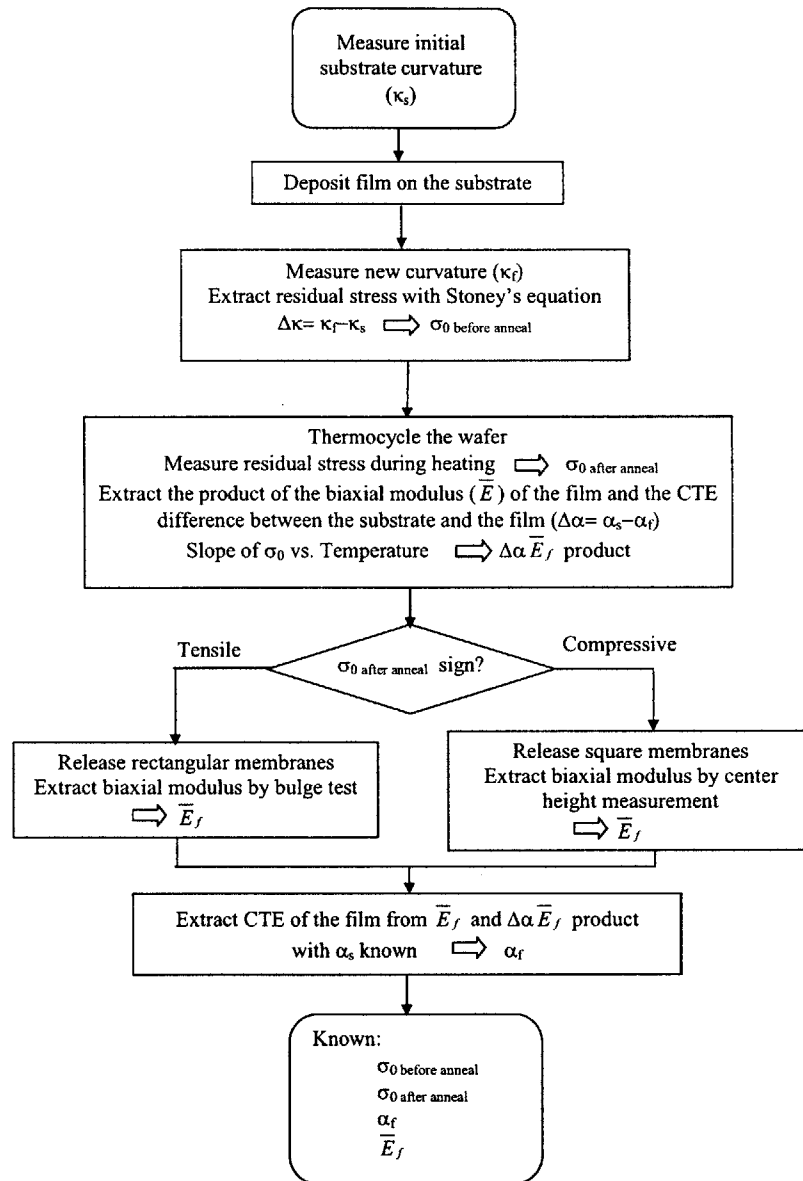


Figure 4-1: Testing flow for key thermomechanical properties of thin membranes.

Bulk Yittria Stabilized Zirconia (YSZ)	
Young's Modulus, E_f [GPa]	200
Poisson's Ratio, ν_f	0.2
Biaxial Modulus, \overline{E}_f [GPa]	250
Coefficient of Thermal Expansion (CTE), α_f [$\times 10^{-6}$ / $^{\circ}$ C]	10

Silicon (100)	
Biaxial Modulus, \overline{E}_s [GPa]	180.5
Coefficient of Thermal Expansion (CTE), α_s [$\times 10^{-6}$ / $^{\circ}$ C]	2.55

Table 4.1: Bulk modulus of YSZ and silicon with (100) orientation, from [7, 8, 9].

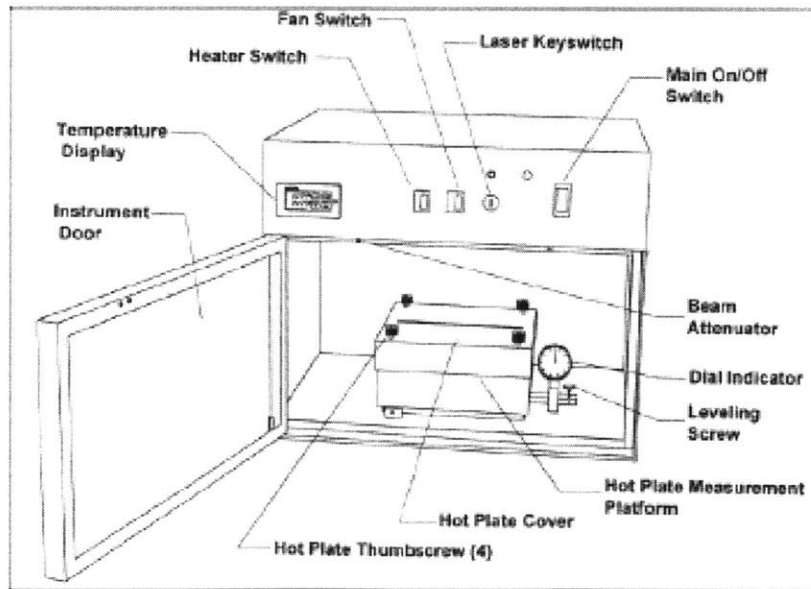
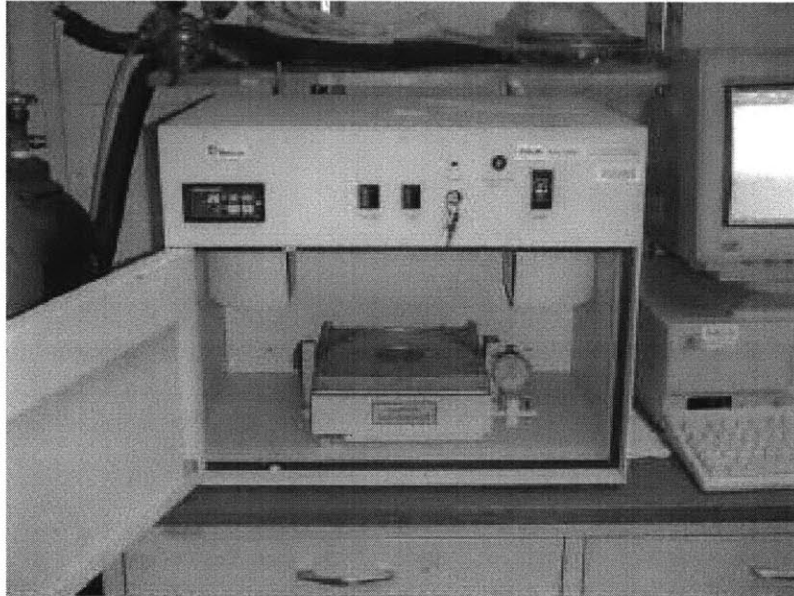


Figure 4-2: A picture (*top*) and schematic (*bottom*) of the Tencor FLX curvature measurement system, from [4, 1].

Residual Stress: As-Deposited and After Post-Deposition Thermocycles

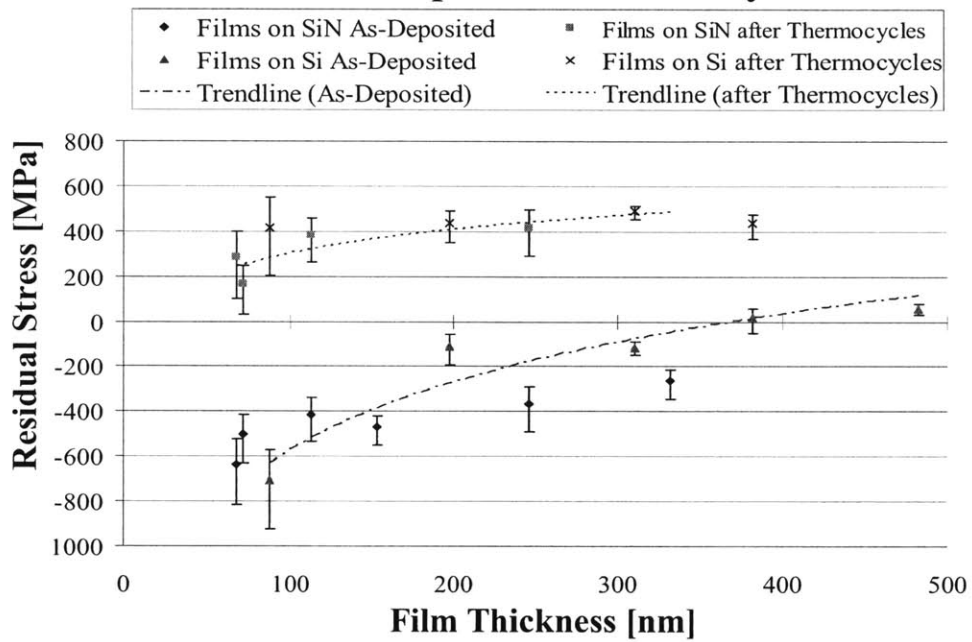


Figure 4-3: Total residual stresses of the YSZ films deposited at room temperature; measured as deposited and after post-deposition annealing.

YSZ Residual Stress Evolution during Post-Deposition Thermocycles ($h_f=87\text{nm}$)

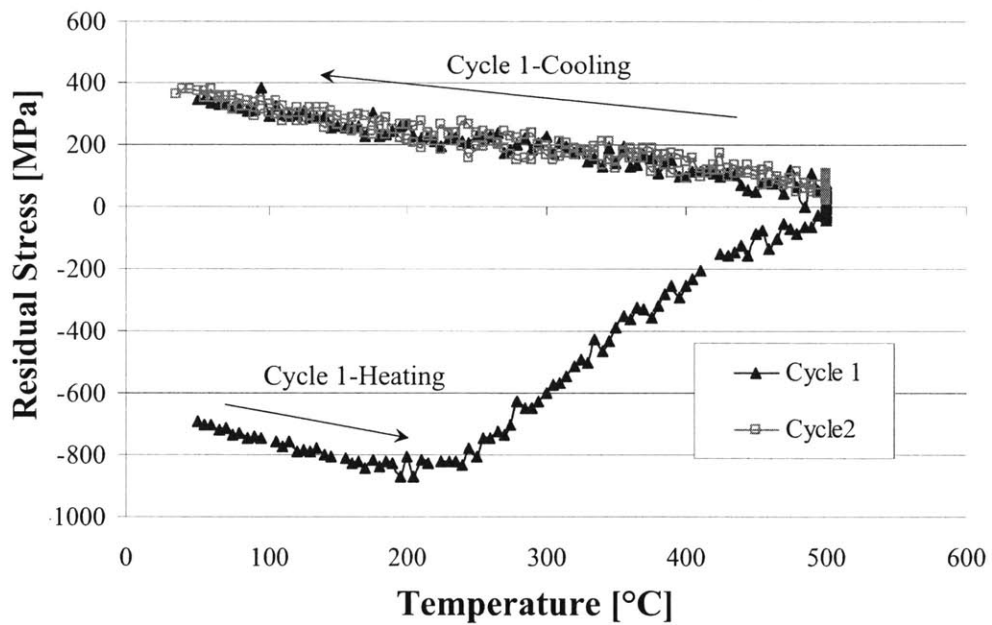


Figure 4-4: Residual stress evolution of an 87-nm thick YSZ film deposited at room temperature during post-deposition annealing.

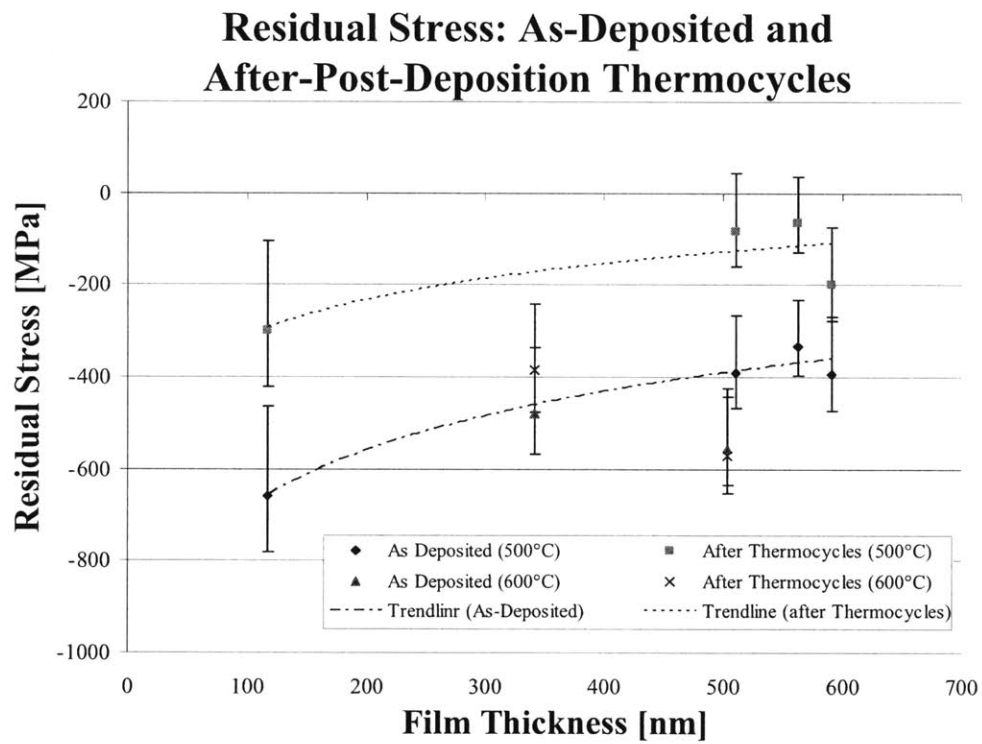


Figure 4-5: Total residual stresses of the YSZ films deposited at high temperature; measured as deposited and after post-deposition annealing.

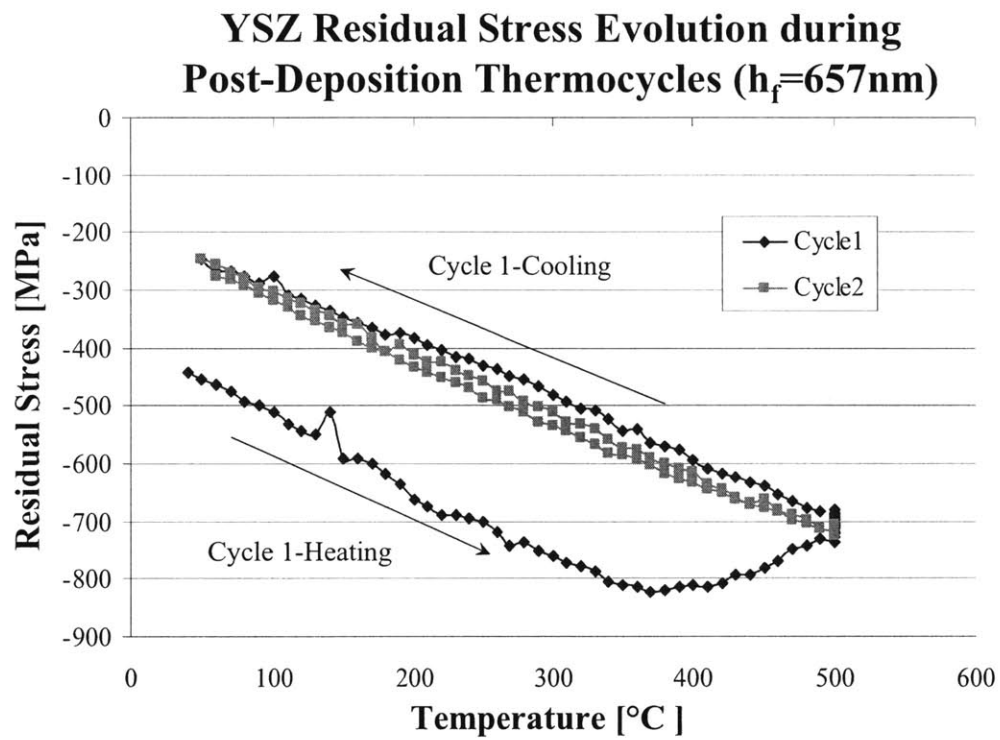
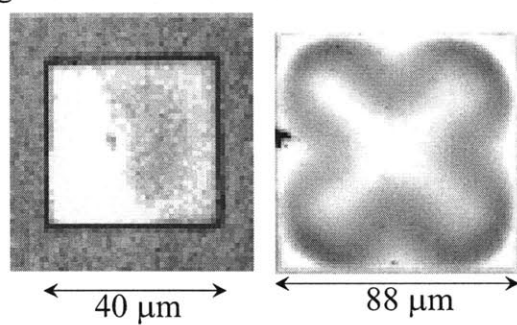


Figure 4-6: Residual stress evolution of a 657-nm thick YSZ film deposited at 500°C during post-deposition annealing.

Deposition Conditions	Number of Samples	Slope (MPa/°C)			
		Cycle 1 Heating; Average	Cycle 1 Cooling; Average	Cycle 2+ Heating; Average	Cycle 2+ Cooling; Average
At Room Temperature, on Si with 300-nm thick Si ₃ N ₄	3	-0.48	-0.32	-0.37	-0.35
At Room Temperature, on Bare Silicon	5	-0.70	-0.47	-0.48	-0.54
At 500°C, on Si with 300-nm thick Si ₃ N ₄	4	-1.01	-0.77	-0.81	-0.88
At 600°C, on Si with 300-nm thick Si ₃ N ₄	2	-1.13	-1.08	-0.94	-1.16
Expected Slope (based on bulk properties)		-1.86			

Table 4.2: Measured slopes of temperature-total stress plots of YSZ films to extract "modulus-CTE" products: $\frac{E_f}{1-\nu_f}(\alpha_s - \alpha_f)$.

First Buckling Mode Evolution with 2-Axis and Rotation Symmetry



Second Buckling Mode Evolution with only Rotation Symmetry

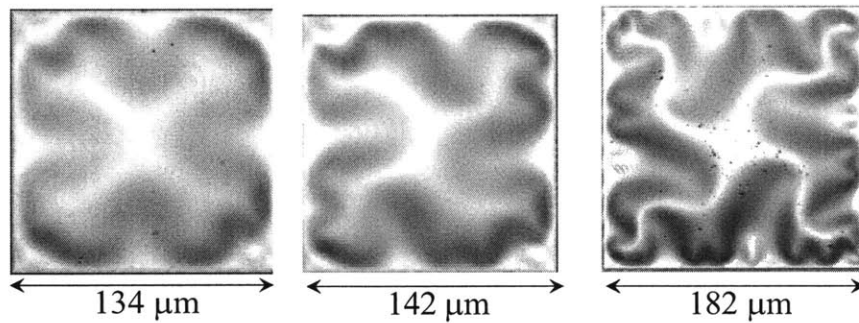


Figure 4-7: Buckling evolution of thin square YSZ membranes deposited at room temperature with film thickness of 368 μm .

Wafer ID	Thickness [nm]	Deposition Temp [°C]	Substrate	Annealing Temp [°C]	Residual Stress after Annealing [MPa]
sq05	625.2	500	Si ₃ N ₄ on Si	500	-65.76
sq06	368.7	Room Temp	Si ₃ N ₄ on Si	300	-38.60
sq07	656.7	500	Si	500	-191.53

Table 4.3: Deposition and annealing conditions for test samples for center height measurement, and their measured residual stresses.

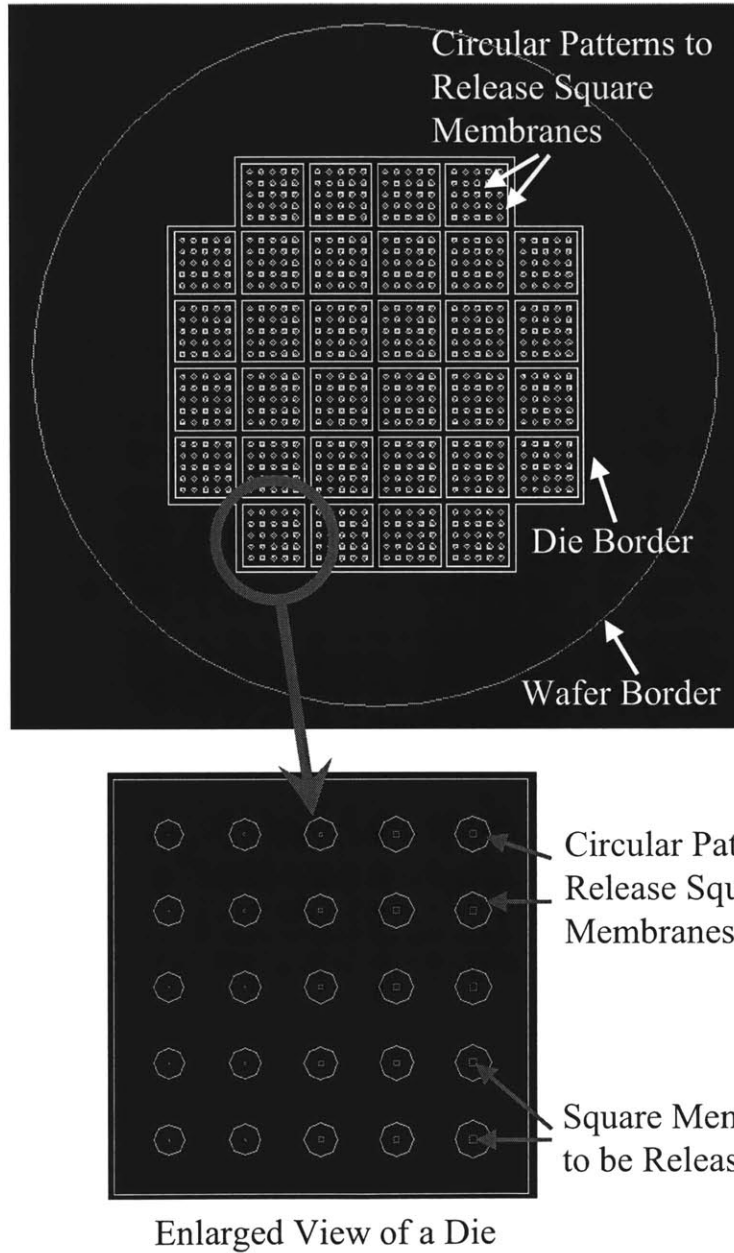


Figure 4-8: Chrome mask design to pattern silicon nitride to release square membranes for center buckling height measurement; wafer view (*top*) and enlarged die view (*bottom*).

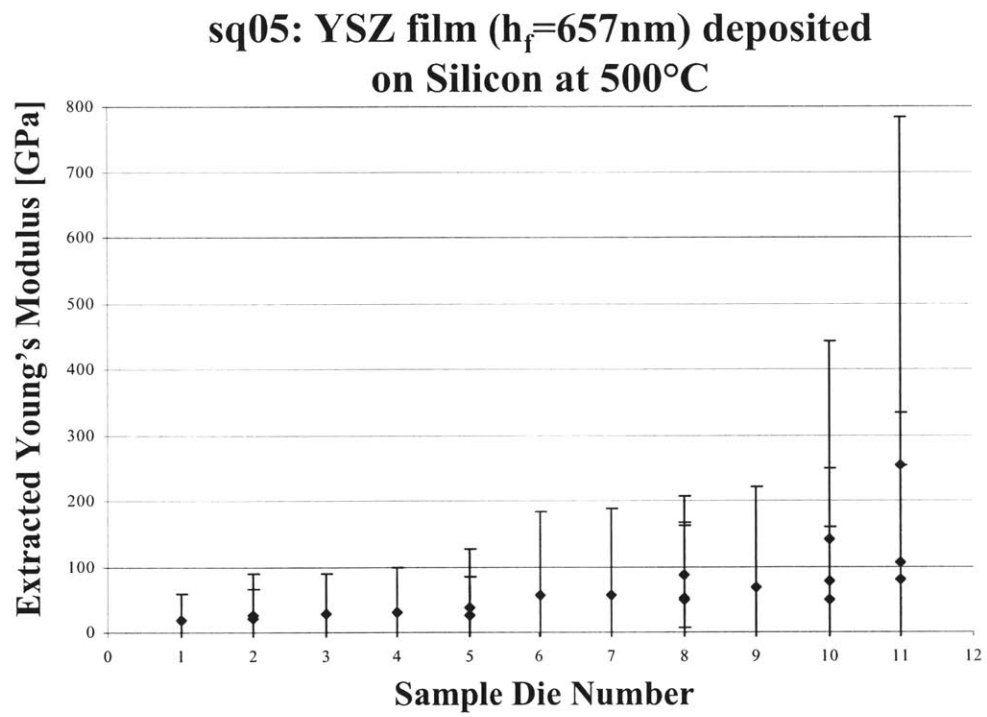


Figure 4-9: Extracted Young's modulus on the sample sq05 by center deflection measurement of square buckled membranes by die.

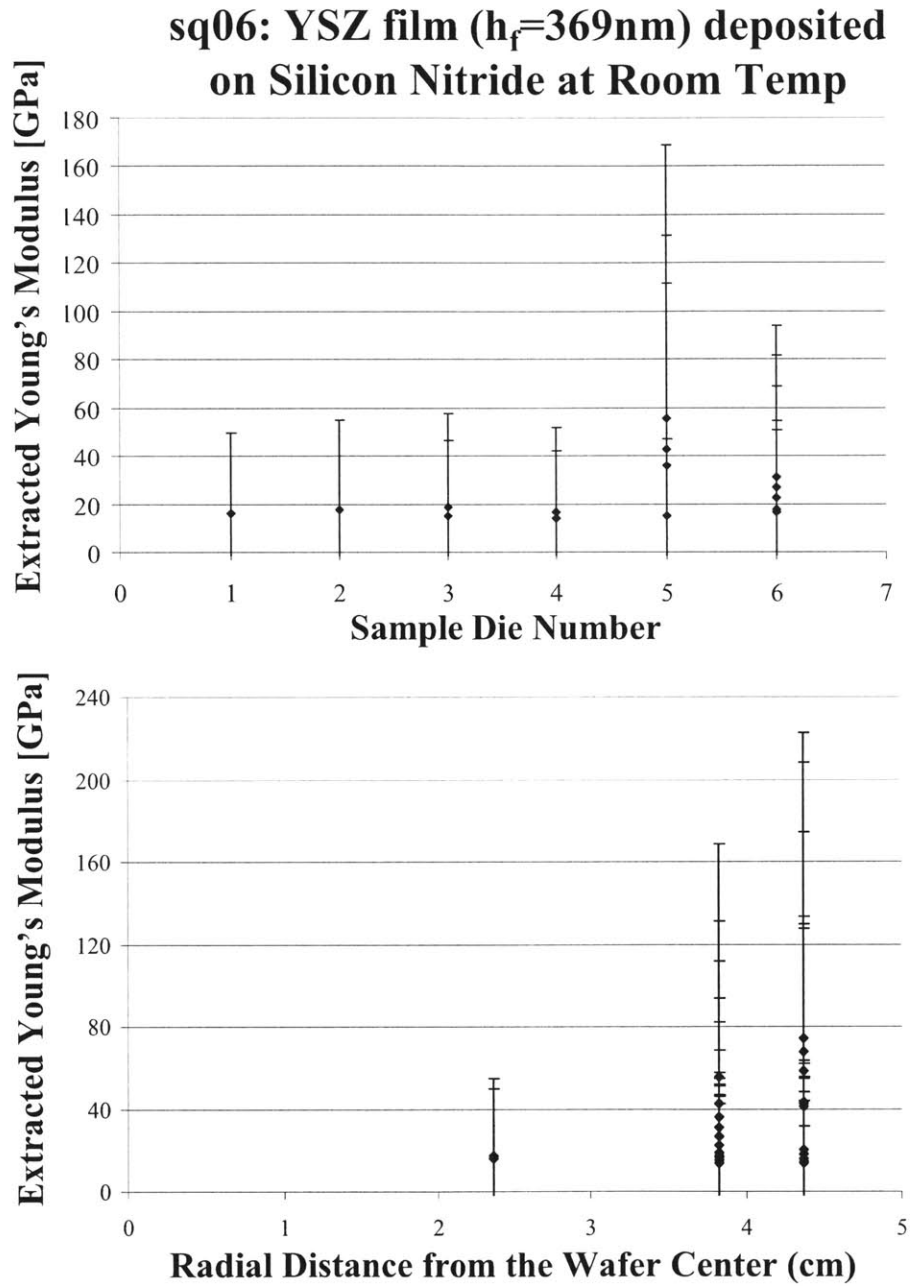


Figure 4-10: Extracted Young's modulus on the sample sq06 by center deflection measurement of square buckled membranes: by die in inner $\sim 40\text{-mm}$ -radius area (*top*), by distance from the wafer center (*bottom*)

**sq07: YSZ film ($h_f=625\text{nm}$) deposited
on Silicon Nitride at 500°C**

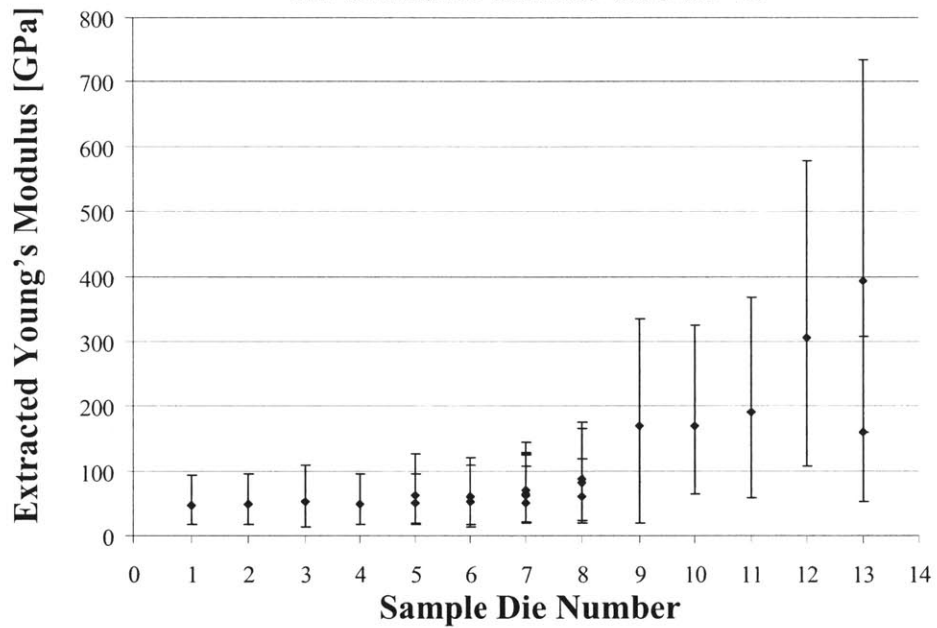


Figure 4-11: Extracted Young's modulus on the sample sq07 by center deflection measurement of square buckled membranes by die.

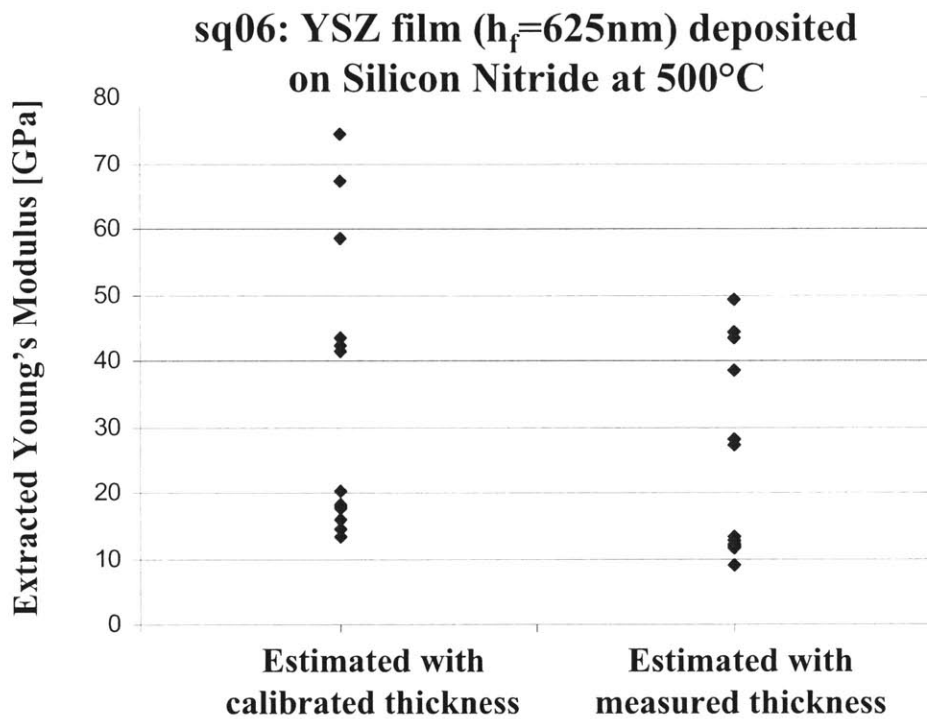


Figure 4-12: Comparison of extracted Young's moduli from dies that are radially ~ 40 mm away from the wafer center with calibrated (by -10%) and measured (at 60mm away from the wafer center) thicknesses.

Wafer ID	Averaged Slope of Temp-Stress Plot [MPa]	Averaged Young's Modulus [GPa]	CTE [$10^{-6}/^{\circ}\text{C}$]	Number of Samples	Coefficient of Variation [%]
sq05	-0.71	63.97	11.39	20	84
sq06	-0.22	24.08	9.74	15	48
sq07	-1.02	106.92	10.20	22	84

Table 4.4: Extracted Young's modulus and CTE from center height measurement of square buckled membranes.

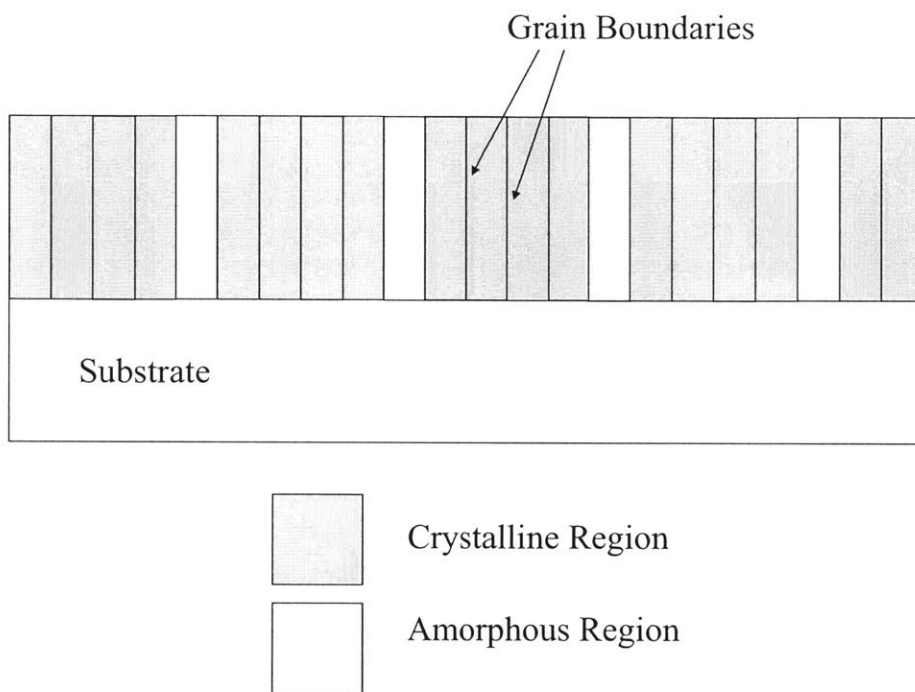


Figure 4-13: Cross-sectional view of microstructure of sputter-deposited YSZ films with mixed amorphous and columnar crystalline phases, from [1].

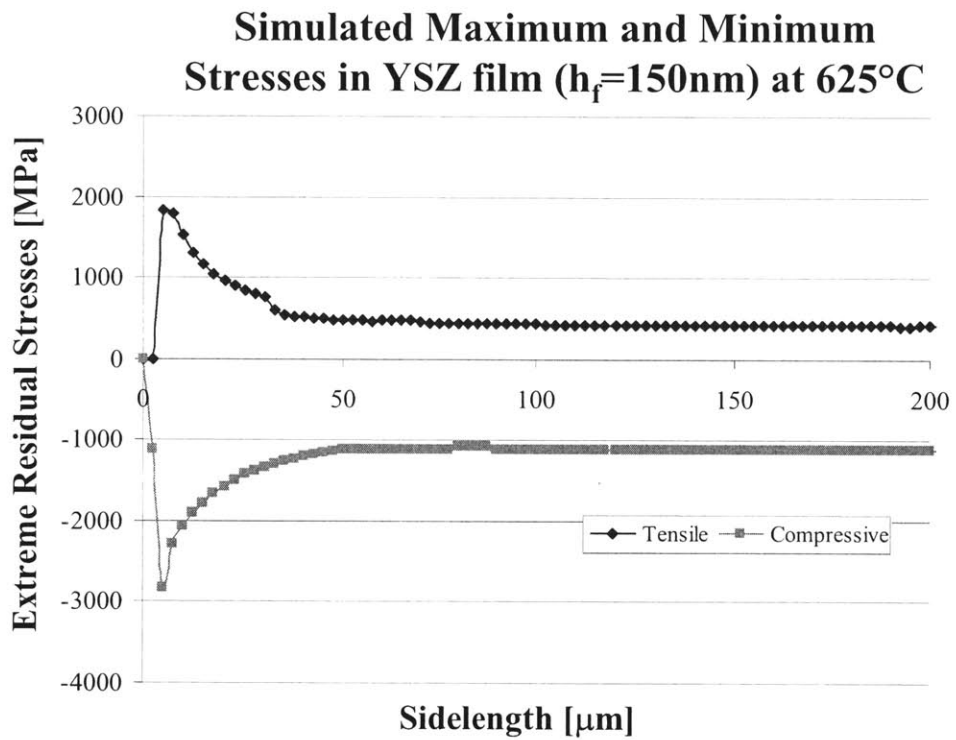


Figure 4-14: Simulated maximum (tensile) and minimum (compressive) stresses in the YSZ film (150nm) deposited at 500°C when annealed to 625°C .

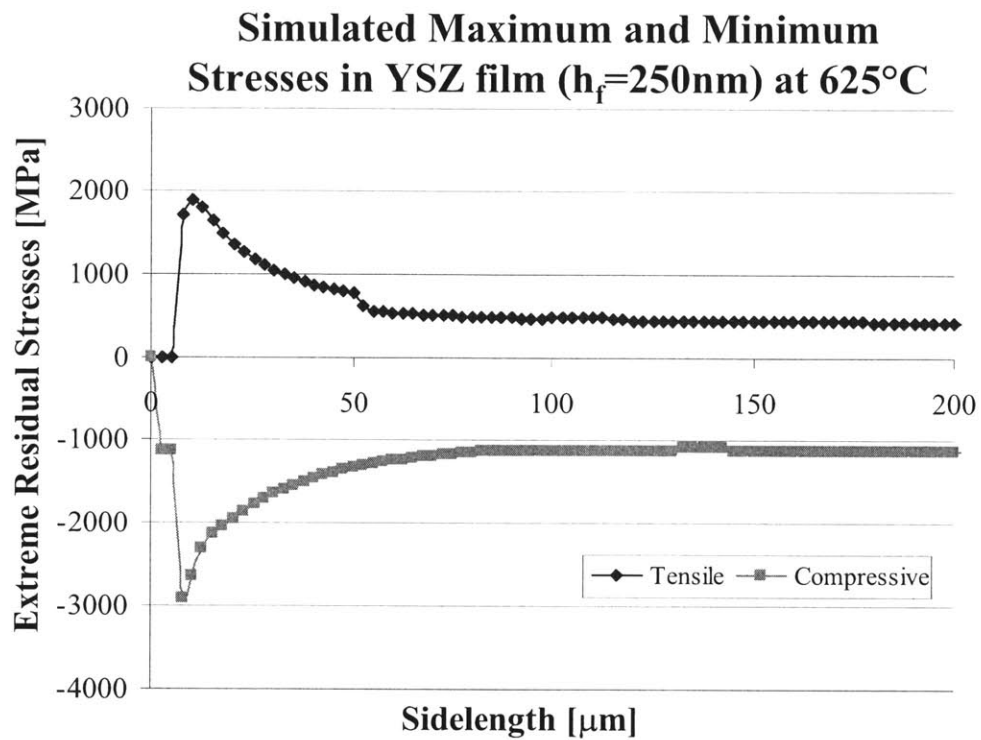


Figure 4-15: Simulated maximum (tensile) and minimum (compressive) stresses in the YSZ film (250nm) deposited at 500°C when annealed to 625°C .

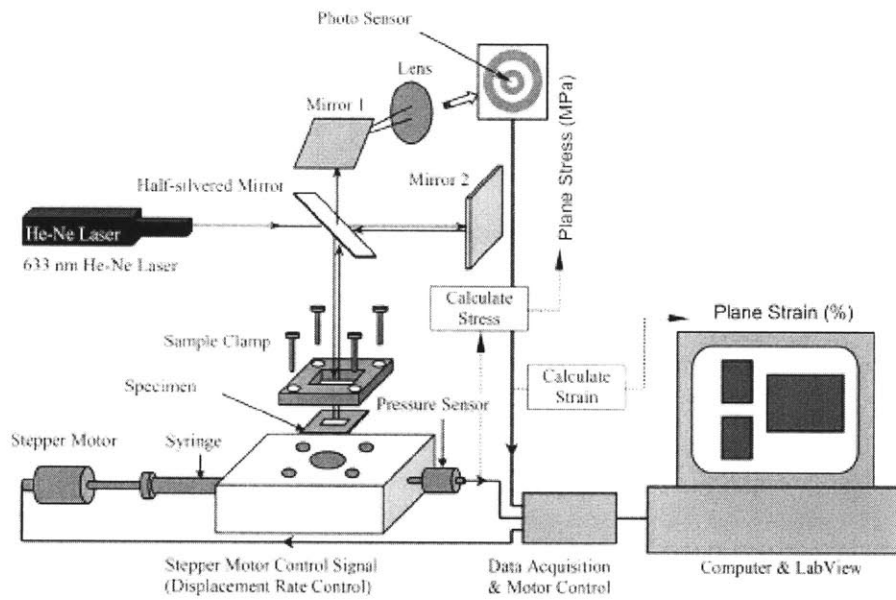


Figure 4-16: Schematic of the bulge test setup at thin film mechanics laboratory at Harvard University, from [5].

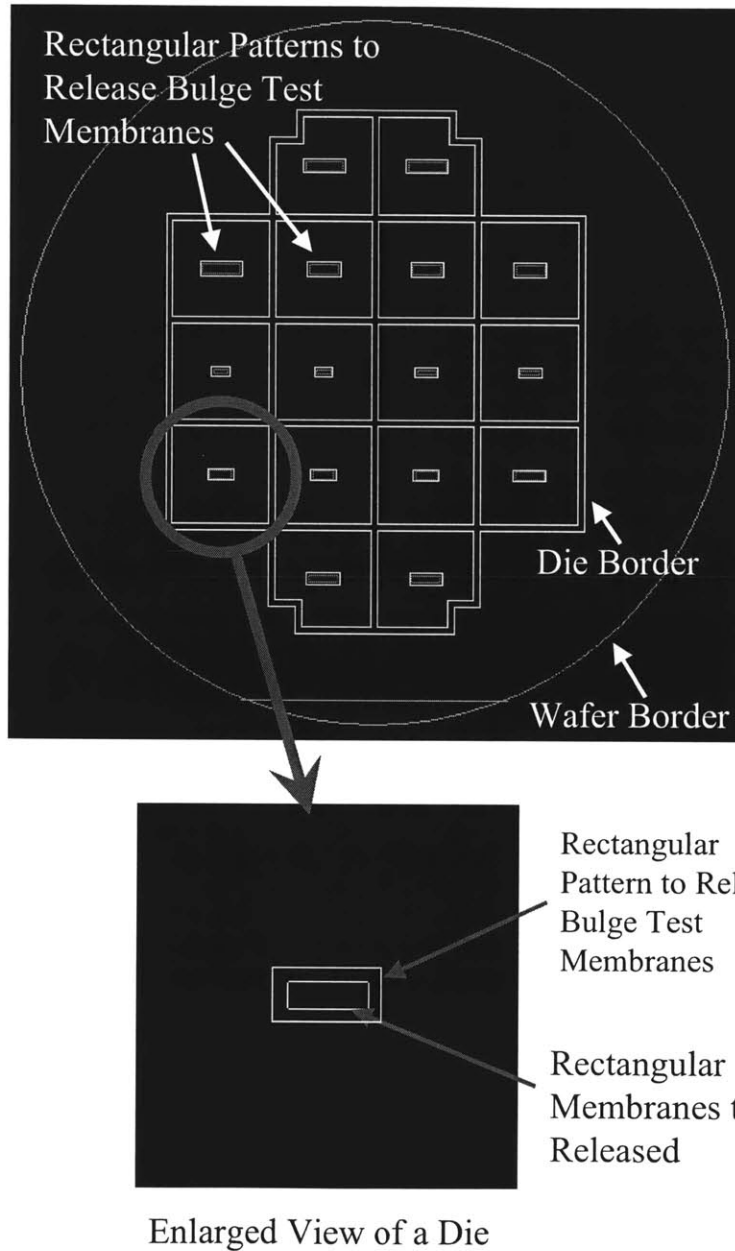


Figure 4-17: Chrome mask design to pattern silicon nitride to release bulge test samples.

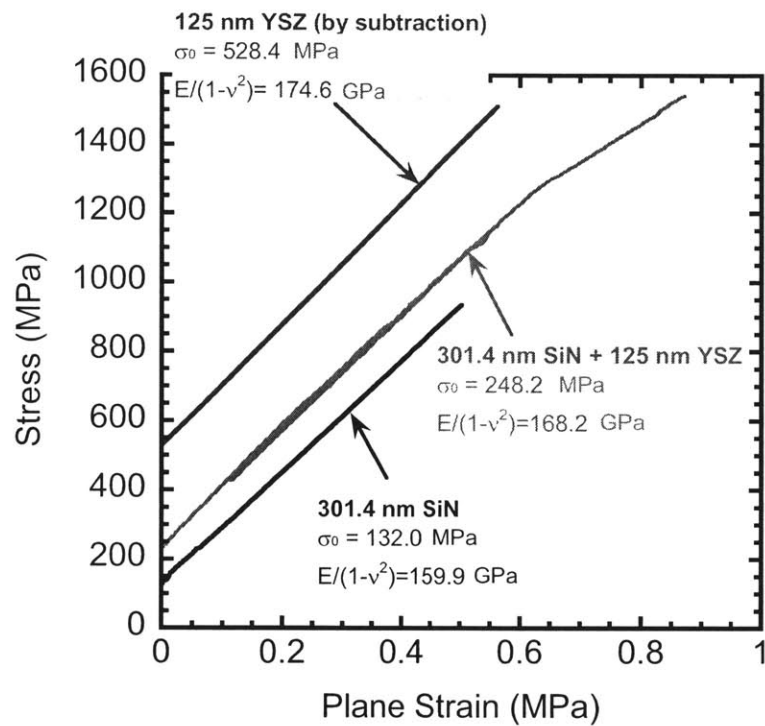


Figure 4-18: Stress-strain slopes on bilayer of YSZ (125nm, deposited at room temperature) and silicon nitride (~300nm) film, just silicon nitride (~300nm) film, and subtracted slope for YSZ stiffness estimation.

Chapter 5

μ SOFC Device Fabrication and Testing

In this chapter, structural design and fabrication processes of μ SOFC devices that achieve thermostructural stability will be presented. The μ SOFC devices were fabricated based on these designs, and were power tested as presented below. In the previous chapter, the material properties (including residual stress) of the YSZ films deposited under various conditions were characterized. In-plane maximum stresses of these films in a post-buckling regime were calculated with von Karman plate theory based on these properties. These studies were well utilized to design the power test samples of tri-layer structure (Pt-YSZ/YSZ/Pt-YSZ). As the Pt-YSZ properties are not yet characterized, preliminary design is based on a single YSZ film. The tri-layer was investigated experimentally, and structural stability under large temperature rise was confirmed. The tri-layer membranes fabricated with the final design were tested to verify that membranes satisfy not only the structural requirement, but also chemical and electrical requirements.

5.1 Design and Fabrication of Fuel Cell Device

Design and fabrication processes of an active fuel cell will be presented in this section. Requirements for power test dies were to have released tri-layer membranes

(cathode, electrolyte, and anode), to be thermomechanically stable under temperature cycles (room temperature to 500–1000°C) necessary for power test setup and operation, to have electric connections for power measurement, and for the ultra-thin YSZ electrolyte to be dense and electrically insulating.

5.1.1 Structural Design

The structure of the tri-layer stack is shown in Figure 5-1. As shown in the cross section, in addition to the fuel cell tri-layer stack, Platinum (Pt) layer and Titanium (Ti) layer were deposited underneath the tri-layer for electric connection output and as an adhesion layer between the Pt layer and silicon substrate, respectively. The thickness of each layer was determined as follows: Pt layer does not adhere well with silicon substrate because Pt or Pt-YSZ layers do not reduce silica to promote reaction at the interface, and to secure bonding between the two. Required thickness of Ti was experimentally confirmed to be $\sim 50\text{nm}$. The fuel cell stack layers (each 250-nm thick, total 750-nm thick tri-layer) deposited with the 50-nm thick Ti layer underneath did not delaminate when heated at $\sim 1000^\circ\text{C}$ for 4 hours [100]. The thickness of Pt contact pad layer was set to 100nm. This thickness was comparable to the thickness of the subsequent Pt-YSZ layer to be deposited next, but nonetheless step coverage was confirmed due to large openings between each film stack patterns. As for the tri-layer, layer thicknesses were kept to 150nm or 250nm. These two thicknesses satisfy the thickness condition ($< \sim 5\mu\text{m}$) required to significantly improve ionic conductivity with electrolyte thinning effect [73, 15].

The die layout is illustrated in Figure 5-2. One die is a square with 30-mm sidelength, and has 64 square membranes. The sidelength of these squares was designed to be either $\sim 100\ \mu\text{m}$ or $\sim 200\ \mu\text{m}$. Based on the in-plane stress analysis performed in Chapter 4, membranes with these sidelengths and the thicknesses mentioned above can survive thermocycles up to 600°C . Releasing the tri-layer membranes deposited at the standard condition with these sizes was experimentally confirmed to be possible by Quinn [100] who successfully released fuel cell stack with sidelengths of $\sim 180\mu\text{m}$. In addition, these areas were designed to produce large enough power for measure-

ment. The power output estimated with electrochemical test data by Hertz [73] was 0.25 W/cm^2 . The power output is at least on the order of tens of μW with the designed square membrane areas, which is easily measurable with the resolution of $\sim 1 \text{ nW}$ available in the lab. Not all membranes on the current dies were used for power testing due to issues with the test fixture and tri-layer shorting from dust as explained below. The glass (Macor) fixture has gold (Au) contact pads attached with long Au wire to transfer current outside the furnace to measure and record the electric signals. With the fixture, two sets of electric signals can be conducted from the two Pt pads ($5\text{mm} \times 8\text{mm}$) that connect with the bottom Pt-YSZ layer and the two top Pt-YSZ layers. Thus, the Pt contact pads and the top Pt-YSZ were situated to connect with the Au contact pads of the fixture. The inner $10\text{mm} \times 10\text{mm}$ square area was the dedicated space for fuel cell stack membranes. The glass fixture for electric connection had a hole for this area to be exposed to gasses. Originally, this inner square area was designed to be covered completely with the top Pt-YSZ area. However, the top and bottom Pt-YSZ layers electronically shorted due to this large area of Pt-YSZ deposition. Among possible other factors, electric shortage was confirmed to occur through asperities in the insulating YSZ electrolyte layer. When YSZ was deposited on the substrate that is cleaned with alcohol before deposition, defects of $5\mu\text{m}$ diameter as shown in Figure 5-3 were observed. When the area of $\sim 1\text{mm} \times 1\text{mm}$ observed under scanning electron microscope (SEM), the defects were roughly $\sim 500\mu\text{m}$ apart from each other. These defects are likely due to dust on the substrate surface introduced from sputtering chamber, wafer handling, or anything that touches the deposition surface. Some adjustment was attempted in the fabrication process to reduce these asperities. For example, wafers were intensively cleaned with strong acid, Piranha, to remove dust particles or oxide layer on the deposition surface. Wafers were annealed (500°C for 20 min.) after each layer deposition to give atoms enough time to diffuse to fill in these defects. YSZ electrolyte layer deposition was broken into two depositions, before and after the vacuum break to change pattern masks, hoping to fill in asperities in the YSZ film deposited before the vacuum break with the one deposited after the break. However, none of the above critically solved the shortage

problem. Instead of fine adjustments in fabrication processes listed above, the stack layout design was changed to decrease the probability of electric shorting. The area of the top Pt-YSZ layer was reduced hoping to decrease the probability of a defect occurring between the deposited layers. This solution worked significantly better than the adjustments mentioned above, although it was purely statistical. As shown in Figure 5-2, the area of Pt-YSZ was reduced, but the silicon nitride patterns to release membranes were kept distributed over the inner square areas as originally planned. Thus, the dies ended up containing bi-layer (YSZ/Pt-YSZ) membranes in addition to the fuel cell tri-layer (Pt-YSZ/YSZ/Pt-YSZ) membranes. The top Pt-YSZ area design came in the variety of 1.25 mm \times 2.5 mm, 1.25 mm \times 3.75 mm, and 2.5 mm \times 3.75 mm areas. Each was designed to have one, two, and four tri-layer membranes on the top Pt-YSZ area respectively. Finally, the membranes were again released with KOH solution. The tri-layers were released by plasma etching the silicon nitride layer and the Ti layer. Nine dies were produced out of one 150-mm-diameter silicon wafer, leaving some room close to the edges for handling purposes as shown in Figure 5-2.

5.1.2 Fabrication

Fabrication of these membranes largely followed the procedures explained in Chapter 3, but involved more sputtering and frequent intensive cleaning between each layer depositions. For power test sample fabrication, double side polished (DSP) silicon wafers were prepared as substrates. Both sides of the substrates required smoothness for clear pattern defining and film stack deposition. Single side polished wafers were ordered from WaferNet, INC. (San Jose, CA), and then the rough sides were polished down to 640–645 μm by Umicore Semiconductor Processing (Boston, MA). As explained in Chapter 3, VTR silicon nitride (~ 300 nm) was first deposited on these substrates for etch mask patterning. The chrome mask to pattern silicon nitride is shown in Figure 5-4. Again, circular patterns were used to etch squares to avoid the effect of misalignment between the substrate and the mask. On the front side of the substrate, a Ti (50 nm) layer was deposited. After the Ti layer deposition, the chamber vacuum was broken to apply a metal shadow mask (see Figure 5-1 and 5-2) for

a Pt layer (100 nm) deposition. After the Pt layer deposition, the vacuum was again broken to apply a silicon mask for deposition of the bottom Pt-YSZ and $\sim 1/2$ of the electrolyte YSZ layer. When originally a stainless steel metal shadow mask was used, due to the CTE difference between the metal mask and the silicon substrate, a gap occurred between the two, and the pattern yielded poorly defined edges. To minimize this effect caused by the CTE difference, a shadow mask made of the same material as the substrate, silicon, was used for deposition of the fuel cell stack layers. In SEM pictures of Figure 5-5, the clear patterning of the bottom Pt-YSZ/YSZ stack layers through a silicon shadow mask is compared with the blurry edges of the top Pt-YSZ patterns deposited on the bottom Pt-YSZ/YSZ layers through a metal shadow mask. After deposition of the bottom Pt-YSZ and the middle YSZ layers through a silicon shadow mask, the vacuum was broken for the third and last time to exchange a silicon mask for deposition of the rest of the YSZ layer and the top Pt-YSZ layer (150 or 250 nm). At all the three vacuum breaks during the sputtering process, the wafers were cleaned intensively with Piranha. During releasing of membranes in KOH solution, deposited layers were protected with a Teflon chuck. Finally, the silicon nitride and the Ti layer underlying the tri-layer were plasma-etched with 25 sccm of SF₆ at 25 mTorr pressure, and with 300 W of incident power for ~ 20 minutes. X-ray diffraction SEM was used to assess residue of these layers after etching. Small signal of N and no signal of Ti were observed as shown in Figure 5-6, showing the two layers were removed. The only material that matched the signal peak at ~ 2.4 was Technetium (Tc), which could be from the SEM stage. However, this inspection was not performed on all dies because membranes on the die break after removal from the SEM stage. The cross-section of the tri-layer fuel cell device cut by diesaw and inspected by SEM is shown in Figure 5-7. The YSZ electrolyte layer was observed to have a columnar structure as expected from the work by Quinn [1].

5.1.3 Statistical Characterization of Electrical Shorting of Power Test Samples

The probabilistic nature of film quality as it relates to functional failure in fuel cell device fabrication is discussed here. Failure of these extremely thin and small membranes came in variety. Membranes physically fail, such as breakage or delamination due to both internal (such as stress) and external (such as handling) factors. Membranes can also functionally fail due to electrical shorting as explained in the section above. In addition, non-uniformity in the film quality (asperities/dust as explained previously) is often observed due to fabrication process, and this variation could significantly affect material properties of deposited films. To understand and control the quality of micro-fabrication, these phenomena was statistically studied and understood. Some of these features have been already discussed in the previous sections, such as thickness uniformity in Chapter 3 and error ranges of the residual stress data in Chapter 4. In this section, the functional failures observed during fabrication of power test samples are discussed and quantified. In the following, the statistics of the functional failures of shorted or broken cathode (top Pt-YSZ) and anode (bottom Pt-YSZ) will be discussed.

One wafer micromachined can produce nine power test samples, and each die has two sets of anodes and cathodes. Thus, in total, 18 connection sets are available on one wafer. Some of these electric connection sets were noted to be shorted with a simple multimeter test. To understand the influence of each fabrication step on this functional failure, these connections were assessed after each fabrication process step that followed film deposition. After sputtering, two fabrication steps followed; releasing membranes with KOH etch and separating dies by diesaw. Asperities caused by dust can induce shortage during film deposition. After KOH etch, released membranes become significantly easier to break when touched. When one membrane breaks in the tri-layer area, the top and bottom Pt-YSZ layers easily contact with each other, causing shortage. At the diesaw, again the membranes might break due to the cutting blade vibration, and thus cause shortage for the same reason. The number of

electrically shorted or broken connections after these different process steps are summarized in Table 5.1. The data is also sorted by the top Pt-YSZ area (small 1.25mm x 2.5mm, middle 1.25mm x 3.75mm, and large 2.5mm x 3.75mm). Larger area was expected to be more likely to experience shortage because it increases the possibility for the film to be deposited over dust. In addition to this prediction, the membranes with thinner electrolyte layer were expected to have more shortage because they have less possibility to overcome the height of the dust that causes shortage. As expected, the number of shorted or broken membranes increased with the top Pt-YSZ area as expected, while the thickness or fabrication processes were not significant factors as shown in Table 5.1. This statistical analysis confirmed possibility to avoid shorting by reducing the probability of having dust underneath the top Pt-YSZ layers with small area. Since elimination of dust in the current sputtering facility was not possible, area adjustment was very effective to fabricate tri-layer membranes without shorting or breakage, even with some yield loss.

5.2 Membrane Stress Evolution under Thermocycling

Fabricated power test dies were thermally cycled up to the operation temperature to experimentally confirm thermomechanical stability. All the membranes on a die were required to survive thermal cycles that the dies have to experience during the power tests including pre-test setup processes. The in-plane stresses of single YSZ membranes of sidelengths of $\sim 80\mu\text{m}$ and $\sim 180\mu\text{m}$ with 150-nm and 250-nm thickness were modeled and predicted to be thermomechanically stable with a temperature rise of 600°C (see section 4.4.4). However, this analysis ignored the effect of the top and bottom Pt-YSZ layers. The material properties used in this analysis for YSZ have a large error range, and are likely different from the ones of the fabricated films due to their high dependence on fabrication process. The geometries of the fabricated samples can be also be different from the values used in the analysis. Thickness

of the layers was not measured to avoid introducing dust on the surface and thus shortage. The square sidelengths were not exactly $\sim 100\mu\text{m}$ or $\sim 200\mu\text{m}$ as designed because of substrate thickness variation from wafer to wafer. The sidelength of the membranes turned out to be $\sim 80\mu\text{m}$ and $\sim 180\mu\text{m}$ due to thinner substrate thickness than designed. Thus, it was critical to experimentally verify the structural stability of the power test membranes.

Experimental procedures for the tri-layer membranes were following: prior to releasing, the tri-layer films were annealed to 500°C and held for 1 hour. Membranes with two different sidelengths ($\sim 80\mu\text{m}$ and $\sim 180\mu\text{m}$) and with different electrolyte thicknesses ($\sim 150\text{ nm}$ and $\sim 250\text{ nm}$) were thermally cycled up to a temperature that varied between $600\text{--}650^\circ\text{C}$, a temperature slightly higher than the operation temperature for the power test purpose. The ramp rate was kept small at $2^\circ\text{C}/\text{min}$. to avoid thermal shock. After holding the desired temperature for ~ 2 hours, more than enough time to finish performing the power test, the dies were cooled down at the same slow rate. The results of this annealing test to assess thermomechanical stability are summarized in Table 5.2. In the following, the structural behaviors of membranes will be discussed in detail with regard to electrolyte thickness.

The fuel cell stack tri-layer (Pt-YSZ/YSZ/Pt-YSZ) membranes (20 membranes) and the bi-layer (YSZ/Pt-YSZ) membranes (172 membranes) with 150-nm thick electrolyte layer were thermomechanically stable under two thermocycles up to $\sim 625^\circ\text{C}$. The top views of several tri-layer membranes are shown in Figure 5-8. The membranes with smaller sidelength are flat as released. After the first heating cycle up to $\sim 625^\circ\text{C}$, the membrane showed the first buckling mode (with axisymmetry), probably due to permanent deformation obtained during thermal cycles. After the second heating cycle, more deformation accumulated, and the membrane showed a second buckling mode with only rotational symmetry. The membranes with larger sidelength begins with the first buckling mode upon release. This is expected because the first critical buckling stress decreases with increasing sidelength, i.e., larger membranes are easier to buckle. Again, the deformation accumulates during annealing, and the membranes attained the second buckling mode after the first and second heating cy-

cle. However, both the tri-layer membranes (4 membranes) and bi-layer membranes (60 membranes) failed when they are heated up to $\sim 650^{\circ}\text{C}$. The failure happened due to high stresses in the center of the film after buckling occurred, as predicted by the in-plane stress analysis with von Karman plate theory.

The fuel cell stack tri-layer (Pt-YSZ/YSZ/PT-YSZ) membranes (14 membranes) and the bi-layer (YSZ/PT-YSZ) membranes (242 membranes) with 250-nm thick electrolyte layer failed when heated up to $\sim 600^{\circ}\text{C}$ and beyond. All the tri-layers were observed to crack from the membrane center as shown in Figure 5-9. The behaviors of the bi-layer (YSZ layer deposited on Pt-YSZ layer, but not capped with the top Pt-YSZ) are also presented in Figure 5-9. Without the top Pt-YSZ, microcracks in the YSZ layers were observed, and the cracks did not pass through the membrane center as with the symmetric tri-layer. Although the patterns seem similar to grains, these patterns are not grains since grains are smaller, and not visible under microscopes. This result of broken or cracked membranes deviated from the in-plane stress analysis of YSZ with 250-nm thickness previously performed. This difference is possibly due to the anode and cathode layers of Pt-YSZ, which were not considered in the stress estimation. The actual tri-layer is thicker ($\sim 750\ \mu\text{m}$), and this thickness increase changes the estimated in-plane stress state as shown in Figure 5-10. First, the stress magnitude at the plateau after buckling increases by $\sim 500\ \text{MPa}$. Second, the stress magnitude peak shifts towards larger thickness. In addition, the resultant fuel cell stack sidelength was $\sim 180\ \mu\text{m}$, closer to the maximum stress peak by $\sim 20\ \mu\text{m}$ than desired. Thus, the membranes with $180\text{-}\mu\text{m}$ sidelength and 250-nm thickness experienced higher stresses than estimated in Chapter 4 (4.4.4), and these stresses were likely higher than the failure stresses.

Overall, the membranes showed a very clear structural behavior according to each specific temperature and membrane geometry. The important trend observed from this annealing test was that all 20 tri-layer and 172 bi-layer membranes with 150-nm thick electrolyte (450 nm, and 300 nm total thickness, respectively) of both $\sim 80\text{-}\mu\text{m}$ and $\sim 180\text{-}\mu\text{m}$ sidelengths survived two annealing cycles up to 625°C . With smaller thicknesses, membranes are easier to buckle or deflect in out-of-plane direction to

relieve stresses. Tri-layers with ~ 450 -nm thickness were employed for the power test sample fabrication.

5.3 Power Test

The fabricated fuel cell device was tested to measure power production. Hydrogen gas fuel flowed on the anode side while the cathode side was left open to the air for oxygen source, and current and voltage were measured from the electric connection pads. The major problem encountered was sealing between the die and the tube, which was successfully solved by a correct choice of bonding. Very preliminary data verified that the fuel cell stack can produce power. However, more improvement on the electric connection and sealing in the test fixture will be necessary to obtain further power test results.

5.3.1 Test Setup and Calibration

This section describes power test setup prepared at Ying's lab at MIT in the Department of Chemical Engineering. The requirements of the test fixture were as follows: first, the device needs to supply oxygen on cathode side and hydrogen on anode side, and these two gas flows need to be separated. Second, the test fixture should acquire electric output from the power generated from the fuel cells. Third, the test fixture should heat the sample to high temperature (500–1000°C), and it should function at high temperature without failure. With these considerations, the following test device was designed and built by Cui from Ying's group [6]. The schematic of the test device is shown in Figure 5-11.

Test Setup

Test setup consisted of several tubes for gas flow supply, and a fixture and wires for electric connections, and a thermocouple to control temperature. As illustrated in Figure 5-11, the most inner Quartz tube supplied the gas, and was contained in a slightly larger Mullite (composite of silica and alumina) tube that supported the

die and the fixture. In addition, the most outer Quartz tube with largest diameter capped these two tubes and supplied oxygen (air) to the die.

Gas flow supply was accomplished as follows: the hydrogen was supplied through the most inner Quartz tube underneath the die with 5% of Hydrogen (H_2) balanced in Helium (He). The diluted hydrogen was used for safety purposes in the electrical test. The gas flow rate range was 40–90 ml/min. with a resolution of 0.1 ml/min., and was set to be 30ml/min. for the power test purpose. The initial gas burst was carefully avoided with a gas escape tube. The gas flowed to the backside of the die (anode side), and then outflowed through the Mullite tube. The outermost Quartz tube was built for oxygen supply, but was left to be open to the air. These two gas flows were designed to be separated by test samples bonded to the Mullite tube. The outlet gas component was analyzed by a gas chromatography (GC) equipped with a thermal conductivity detector (TCD). The sampling interval was set at 25 mins. The O_2 and N_2 signals, if any, were recorded. These signals were used to assess leakage through the bonding between dies and the Mullite tube, or to observe gas consumption as the electrochemical reactions progress. The GC data were synchronized with the temperature history by the time.

Good bonding between the testing die and the Mullite tube was critical to avoid mixing of the two gases. The die and the tube were carefully sealed with a ceramic bonding called 618N from AREMCO. This ceramic bonding is based on silica, and shows strong adhesion to the silicon. The only concern was that the CTE of this bonding is significantly smaller ($0.59\mu/^\circ C$) than those of silicon ($2.7\text{--}4.3\mu/^\circ C$) or Mullite ($5\text{--}5.3\mu/^\circ C$). Originally, the bonding was done between a silicon die and an inner gas supply tube made of Quartz, but the tube did not survive stresses caused by the CTE difference at high temperature and kept breaking. Thus, the inner tube was replaced with a Mullite tube, which has a similar CTE with silicon, and is stiff enough to survive high stresses. Other bonding attempted such as Pyrex powder, glass-lead mixture powder, or alumina bonding were unsuccessful. All are not recommended for this test for each specific reason. Pyrex 7740 powder's softening point was higher ($\sim 800^\circ C$) than the maximum temperature that membranes can be thermome-

mechanically stable. Glass powder with lower softening point was also available, and these powder were mixed with other components such as lead and zirconia to reduce the softening point to 400–500°C. SCB-1 from SEM COM Company (Toledo, OH) was tried, but the bonding components evaporated during the first curing cycle, and adhered to the bottom of working fuel cell membranes, causing breakage or blocking of the membranes. In addition, the working temperature range of these bonds was rather low, and cannot survive desirable operation temperature. Alumina bonding, Ceramabond 552 and 569 from AREMCO (Valley Cottage, NY), was also tested. However, they were not gas-tight. Other than the glue bonding, O-ring sealing, or localized heating using an on-chip heater were also considered as options to separate the gas flows at high temperature. Such O-rings that work at high temperature are made of metals that require high load to keep sealing. On-chip heaters require another metal layer deposition on the testing dies. But, increasing the deposition area might again cause the shortage problem. Thus, the silica-based bonding was the best initial choice above all mentioned. Before application of the silica bonding, the die was cleaned with alcohols. The Mullite tube was sanded to rough the surface for bonding application, and dried. A thin layer of bond was applied to the Mullite tube cross sectional surface. After drying the bond in room temperature for 3–4 hours, the setup was loaded into a furnace, and bonding was cured under the following recipe. The temperature was increased at a heating rate of <2 °C/min, and held at 93, 269, and 371 °C each for two hours. After curing, the temperature was decreased down to room temperature at a similar rate. During curing cycle, pure He was supplied instead of H₂ balanced in He.

The Macor fixture was capped on top of the die attached to the Mullite tube. As briefly mentioned in the previous section, this fixture was equipped with Au contact pads for the electric signals from the two sets of anode (Pt contact pad) and cathode (top Pt-YSZ layer). The gold wires were extended out of the furnace, and connected with a Solartron SI 1287 electrochemical interface, which can measure voltage and current. The anode layer was set as working electrode, and the cathode layer was set as reference. The voltage and the current from the power test dies were measured and

controlled by the SI 1287 with a resolution of at least 1 nA. To regulate the voltage for power extraction and to measure impedance through the tri-layer, software called Corrware and Zplot were used. With these devices, three different measurements were taken at each desired operation temperature. After allowing enough time (~ 25 min.) to stabilize the temperature and reactions once the temperature reached the designated value, three parameters were measured sequentially: impedance, open circuit voltage (OCV), and power output. Estimation of these three can be made by the area specific resistance of the YSZ layer, which was measured as a function of temperature with electrochemical tests by Hertz [101]. The resistance decreased with increasing temperature as $100 \text{ } \Omega/\text{cm}^2$ at 433°C , $10 \text{ } \Omega/\text{cm}^2$ at 511°C , and $1 \text{ } \Omega/\text{cm}^2$ at 608°C . The OCV is normally material specific, and was observed to be $\sim 1.1 \text{ V}$ again with electrochemical tests by Hertz [101]. The power output at 600°C was estimated as $0.25 \text{ W}/\text{cm}^2$ with the values above assuming the maximum power is produced at half the OCV.

A thermocouple was located next to the testing die. After the bonding was cured, the dies were heated up to the operation temperature range for the power test. With a ramp rate of $\sim < 3^\circ\text{C}/\text{min.}$, the dies were heated up to 300°C , where the first power test measurement was taken. Subsequent measurement was performed at every 50°C rise up to 600°C . The 40-minute time span was allowed at every temperature stop to stabilize reactions and perform the three power test measurements. After the last measurement was taken at 600°C , the system was cooled down to the room temperature at the similar slow rate.

Calibration and Gas Leakage Characterization

The GC was calibrated to obtain gas flow rate from the integrated peak value by flowing a calibration gas with its composition known ($3\% \text{O}_2$, $3\% \text{N}_2$ balanced in He) to the GC at the known flow rate. With the calibrated GC, the gas leakage of the seal was characterized. With perfect sealing, the gas sent to the GC from the He gas outflow tube should not contain either oxygen or nitrogen. However, both signals were observed in GC because the leakage through the bonding is small, but

exists. A dummy die without any patterns were used to seal the tube with the silica-based bonding to ensure that the gas leakage measured is through the bonding. The leakage through other parts, such as tube connections, was found to be very small and negligible [6]. The history of nitrogen and oxygen signals during the first curing cycle of the bonding is shown in Figure 5-12. The nitrogen leakage rate with the signal of ~ 300 was calibrated as $\sim 1\%$ of the supplied gas. Similar leakage range was observed for the power test dies with the membranes. The leakage within this range was considered acceptable to perform the power test. As a reference, leakage with as large as ~ 1000 signal showed air bubbles coming out through the bonding when the tube bonded with the die was put inside water.

5.3.2 Results

The power test was performed on the tri-layer with each thickness of ~ 150 nm (~ 450 nm-thick fuel cell stack membrane). The area of the working fuel cell membrane was $6847\mu\text{m}^2$. The power output from this sample at temperature from 350°C to 500°C is shown in Figure 5-13. The largest power output was ~ 0.1 mW/cm² at 500°C . The data at 300°C was not presented because the sample produced negligible power. The data at 550°C and 600°C were also eliminated because the bottom Pt contact pad delaminated at these high temperatures.

The positive part of this result is that power was generated with the fabricated fuel cell stack. The reaction was confirmed by the sudden oxygen reduction observed in the outflow gas around at 300°C as shown in Figure 5-14, and by steam trace on the outer Quartz tube indicating the sign of water fabrication. However, this preliminary power test had some features that were different from expectations or that were hard to interpret. First, the OCV (0.01 – 0.18 V) was significantly smaller, roughly one-tenth, than the expected OCV (1.1 V). Thus, the power output (0.005 – 0.1 mW/cm²) was lower by a factor of more than a hundred than the estimated value (0.25 W/cm²). Various causes for this low power output can be considered. Fuel supply to the membranes might not have been sufficient to continue electrochemical reactions to produce power. The hydrogen supply could have been low with the low concentration

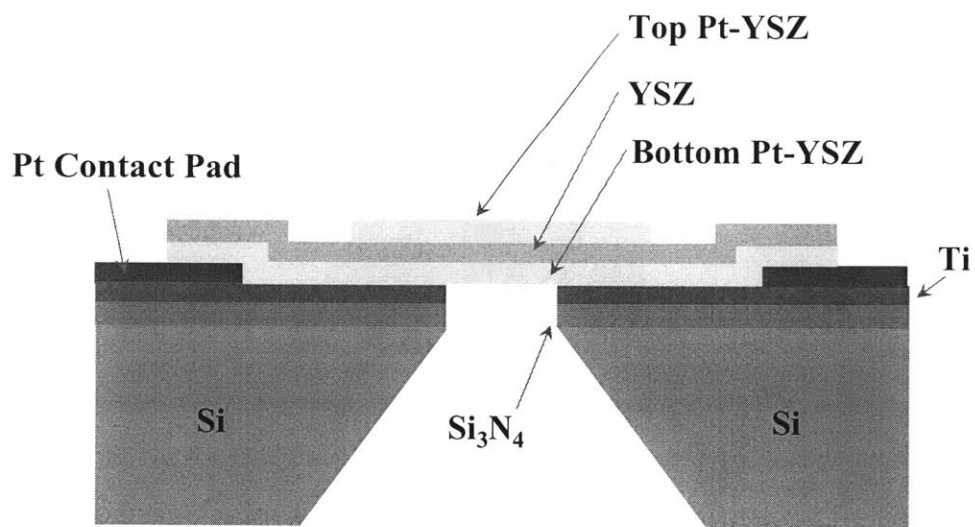
gas flow. The oxygen supply could have not been diffused well by the air stagnated in the Quartz tube. Suzuki et al. observed the OCV increase with increasing gas flow rate [102], and Haart et al. measured the OCVs varying with fuels with various compositions [103]. In addition, gas leakage might have physically transferred oxygen across the membranes rather than electrochemically. Electric shortage might have been another cause. With electric shortage, the power will be sent to outside, for example through volt meters, or will be dissipated internally by the electrolyte resistance [104]. Another possible cause of low voltage is that the silicon nitride and Ti layers, the underlying layers that were necessary in fabrication processes, were not completely removed, and were blocking membranes. In addition to the low power values, the power outputs did not necessarily increase with the temperature, which result is against the decreasing area specific impedance with temperature. For example, power output at 400°C (0.008 mW/cm²) was larger than that of 450°C (0.005 mW/cm²). One possible explanation for this unexpected behavior is that flow rate or leakage rate are non-linear functions of temperature.

The fabricated membranes have also been tested electrochemically at high temperatures by applying voltages to induce oxygen ionic conduction. The data is still being compiled at the time of writing this thesis [73].

5.3.3 Conclusions

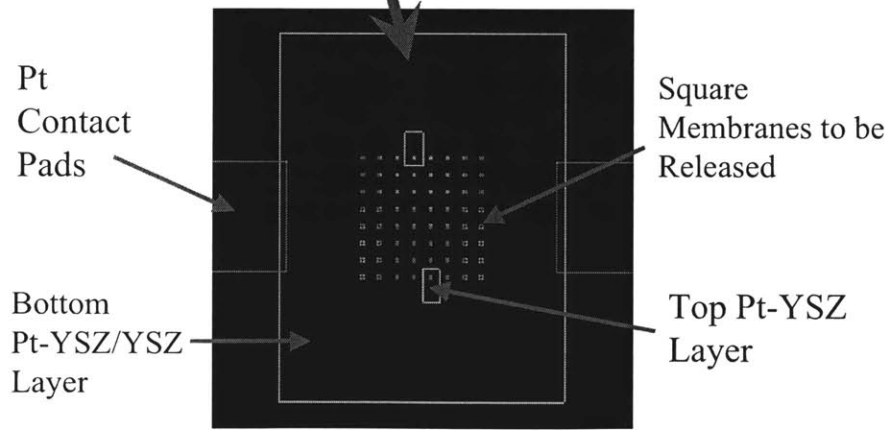
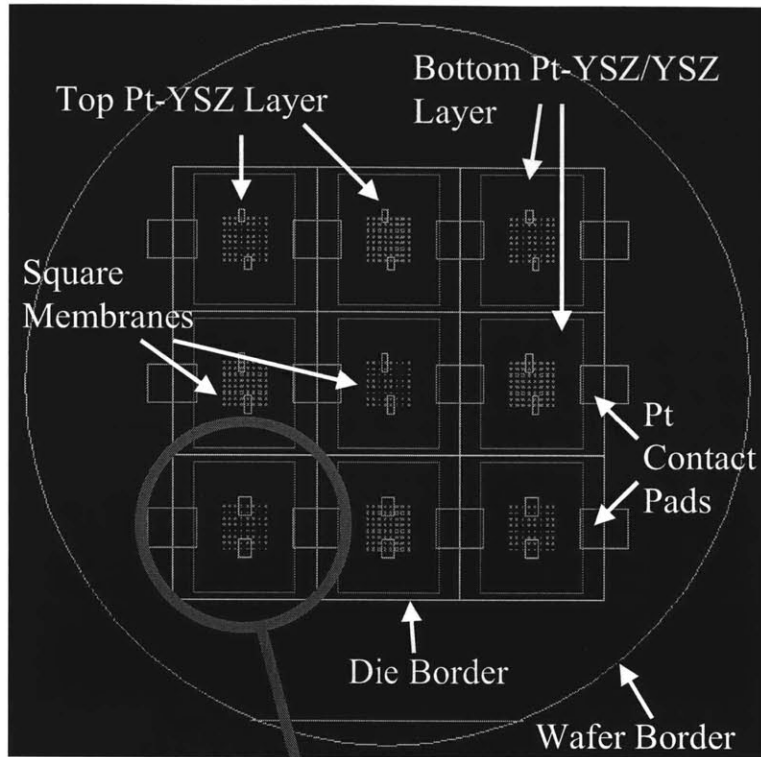
Power test samples were designed based on the material properties and in-plane stress analysis developed in the previous chapter. In addition to the factors that determine structural stability and functionality of a working SOFC, the design procedure required compensation for shorting due to dust in the sputtering environment. Working SOFC membranes with 150-nm thick electrolyte layer were successfully released. These membranes were thermally stable during and after two thermocycles up to 625°C. Power tests were conducted on these membranes. Observed power was significantly lower than expected due to low OCV. The factors causing this low output was investigated by comparing with other SOFC tests with YSZ electrolytes available in the literature. Among various causes, lack of fuel to continue reaction seemed to be a

major cause. This can be easily confirmed by adjusting the gas flow rate. The power test setup and samples still involve with many malfunctions, such as gas leakage, electric leakage, electrical contact issues at high temperature, and others. The test setup needs to be improved to check the device's functionality and to optimize the power output. The suggested work to be done will be discussed in the next chapter.



[Not to scale]

Figure 5-1: Cross sectional view of the fuel cell device with electrical outputs (top Pt-YSZ and Pt contact pad).



Enlarged View of a Die

Figure 5-2: Layer layout of the fuel cell device and the die layout on a wafer.

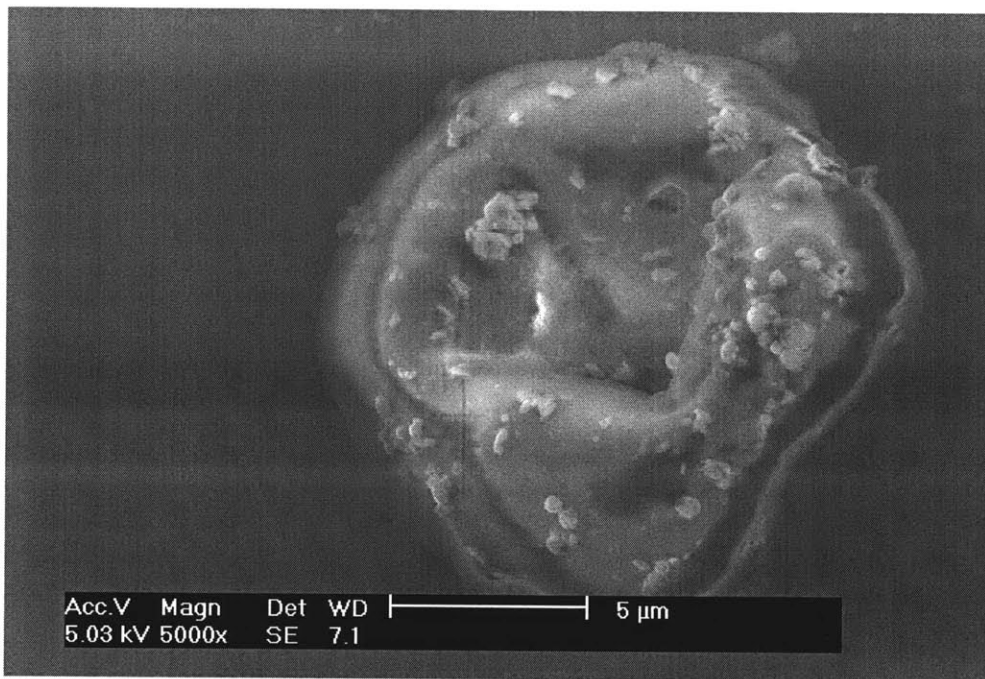


Figure 5-3: Typical dust defect in the electrolyte YSZ layer observed with SEM.

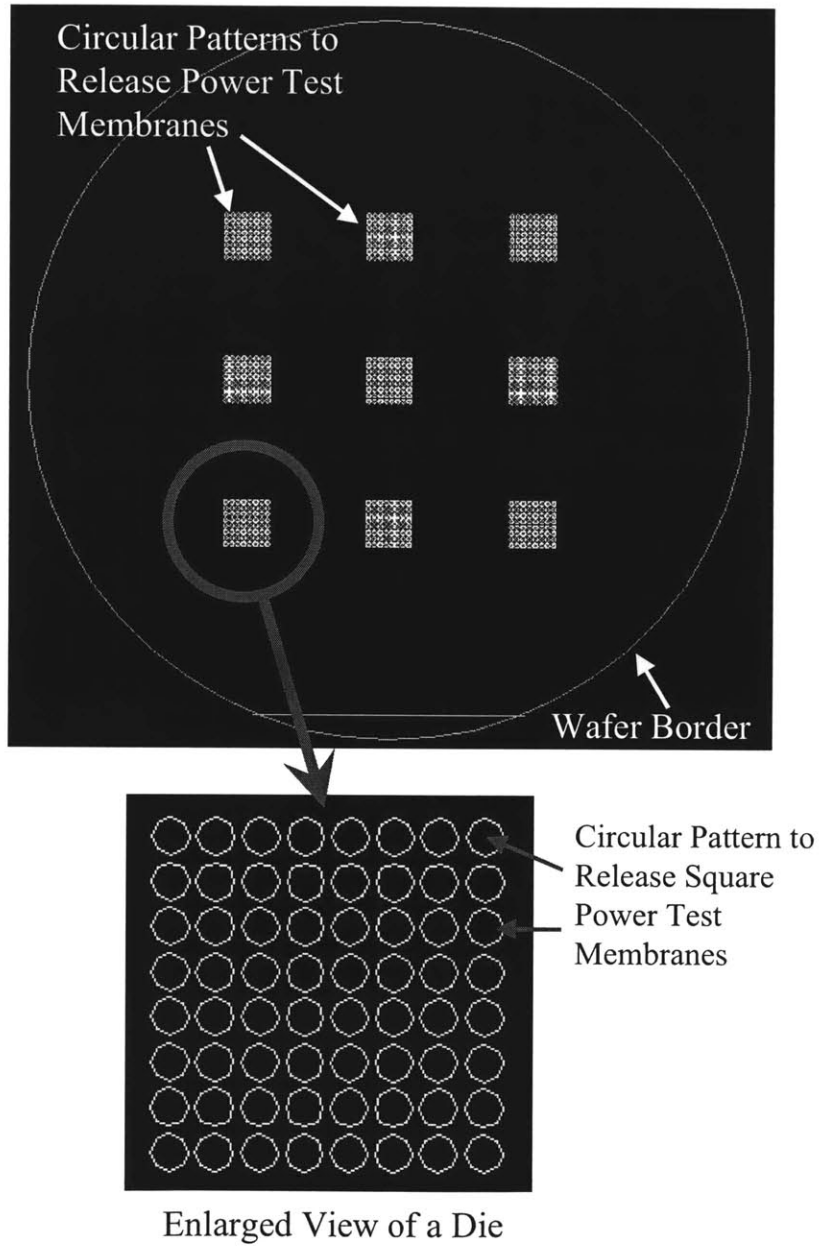


Figure 5-4: Chrome mask design to pattern silicon nitride to release fuel cell tri-layer membranes; wafer view (*top*) and enlarged die view (*bottom*).

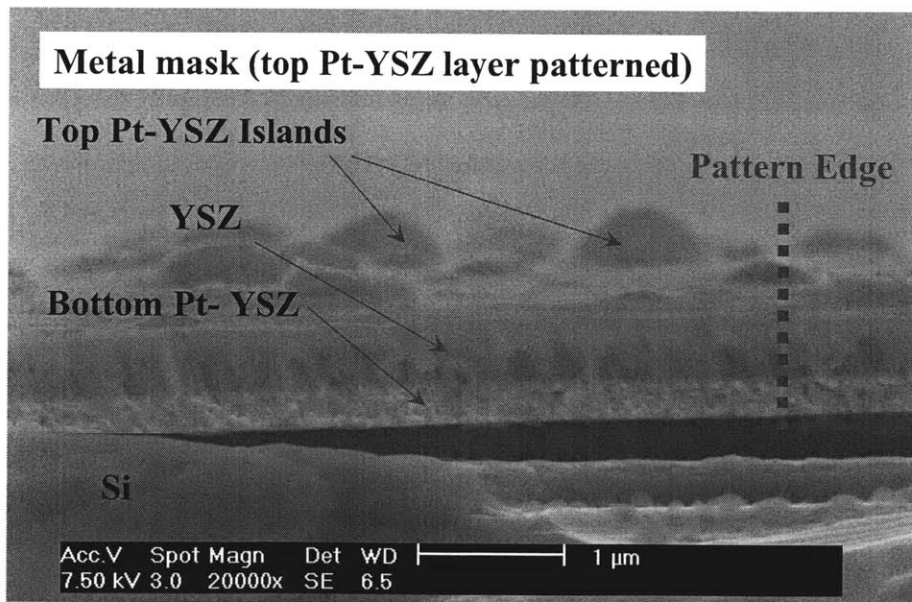
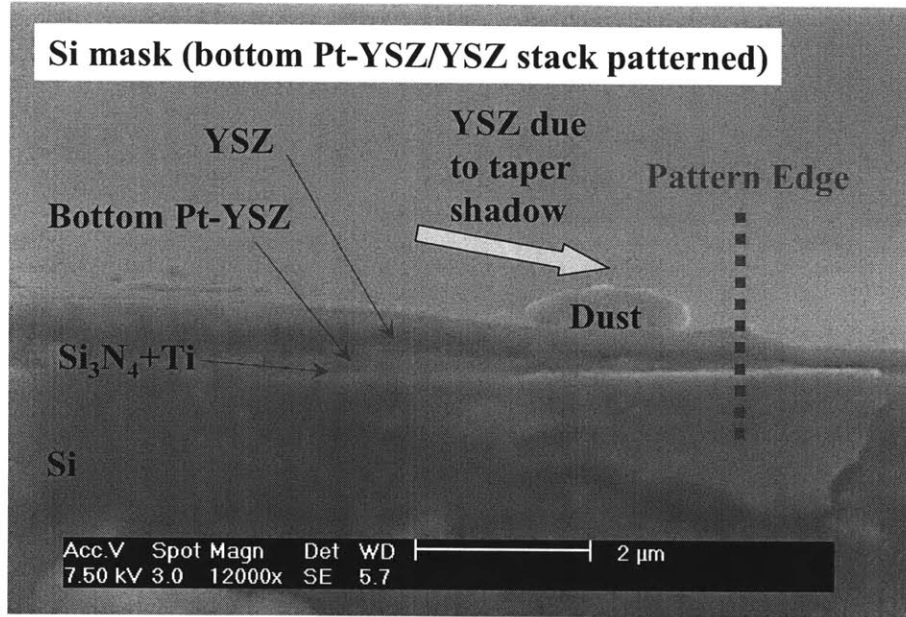


Figure 5-5: Edges of the films deposited through a silicon shadow mask (*top*) and a metal shadow mask (*bottom*) by SEM.

X-ray Signals of Materials on a Fuel Cell Stack After Plasma Etch

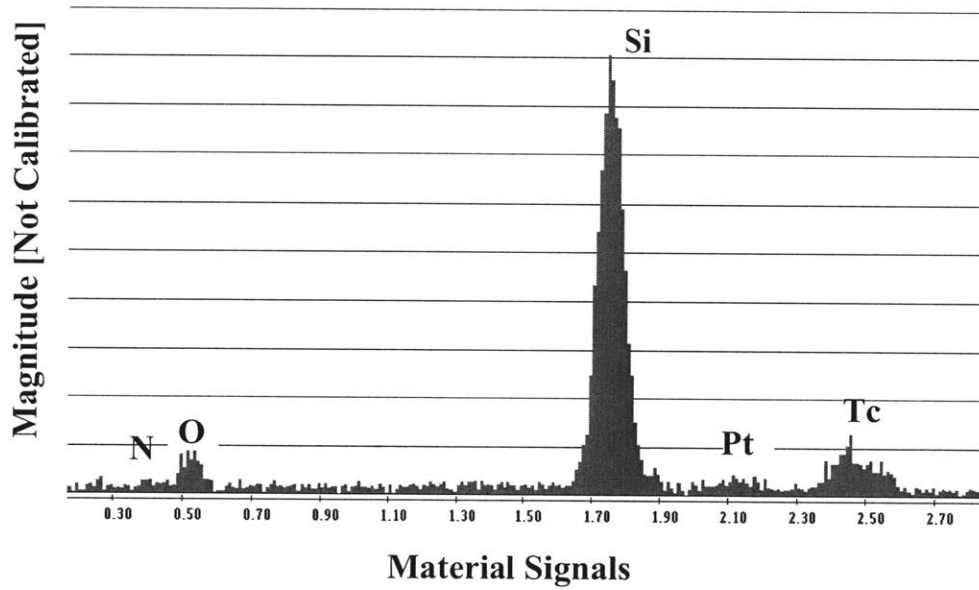


Figure 5-6: XRD SEM signals on a fuel cell tri-layer membrane on the KOH etch side after plasma etching

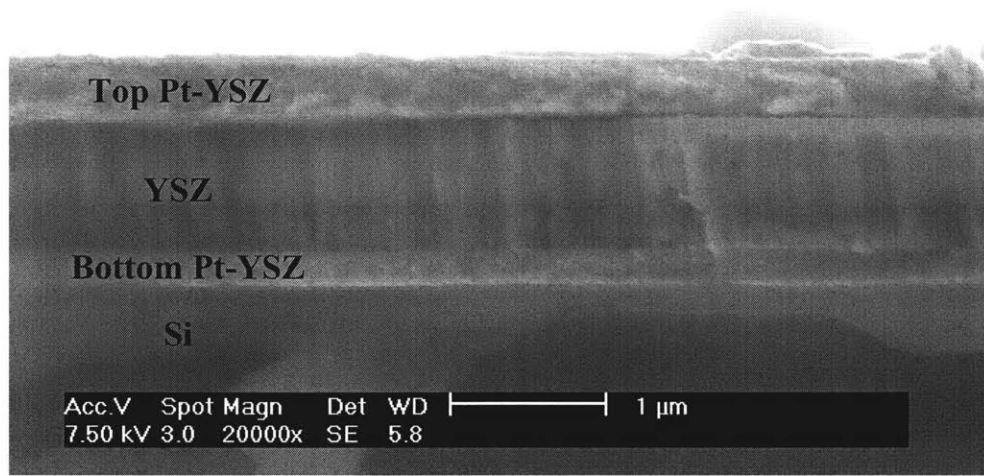


Figure 5-7: Diesawed cross section of the tri-layer stack (Pt-YSZ/YSZ/Pt-YSZ) inspected by SEM with thicker YSZ ($\sim 1\mu\text{m}$) than in the tested fuel cell device (YSZ thickness of 150 nm).

Electrolyte thickness [nm]	As-deposited					
	Small-sized area		Middle-sized area		Large-sized area	
	Shorted	Un-shortcd	Shorted	Un-shortcd	Shorted	Un-shortcd
250	1	5	2	4	0	6
150	1	5	4	2	3	3
150	1	5	1	5	1	5
150	0	6	0	6	1	5
150	0	6	1	5	3	3
Total for 150	2	22	6	18	8	16

Electrolyte thickness [nm]	As-released after KOH etch					
	Small-sized area		Middle-sized area		Large-sized area	
	Shorted /broken	Un-shortcd	Shorted/ broken	Un-shortcd	Shorted/ broken	Un-shortcd
250	1	5	2	4	0	6
150	1	5	4	2	3	3
150	1	5	1	5	1	5
150	0	6	0	6	1	5
150	1	5	3	3	3	3
Total for 150	3	21	8	16	8	16

Electrolyte thickness [nm]	After Diesaw					
	Small-sized area		Middle-sized area		Large-sized area	
	Shorted /broken	Un-shortcd	Shorted/ broken	Un-shortcd	Shorted/ broken	Un-shortcd
250	2	4	2	4	0	6
150	1	5	4	2	3	3
150	1	5	1	5	1	5
150	0	6	0	6	1	5
150	2	4	3	3	3	3
Total for 150	4	20	8	16	8	16

Table 5.1: Statistics of electrical shortage between the anode and cathode layers on power test samples (small 1.25mm×2.5mm, middle 1.25mm×3.75mm, and large 2.5mm×3.75mm).

Electrolyte thickness/ total thickness [nm]	Square sidelength [μm]	Annealing temp [$^{\circ}\text{C}$]	1st cycle		2nd cycle	
			Number of membranes annealed	Number of membranes survived	Number of membranes annealed	Number of membranes survived
Tri-layer						
150/450	80	625	8	8	8	8
150/450	180	625	12	12	12	12
150/450	180	650	4	0		
250/750	80	600	2	0		
250/750	80	625	4	0		
250/750	180	640	8	0		
Bi-layer						
150/450	80	625	56	56	56	56
150/450	180	625	116	116	116	116
150/450	180	650	60	0		
250/750	80	600	62	0		
250/750	80	625	60	0		
250/750	180	640	120	0		

Table 5.2: Statistics of square released tri-layer (Pt-YSZ/YSZ/Pt-YSZ) and bi-layer (YSZ/Pt-YSZ) membranes that survived thermal cycles.

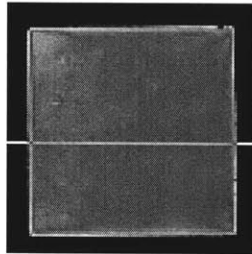
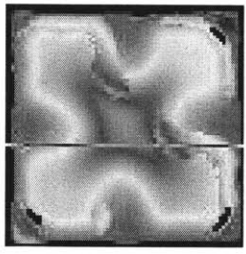
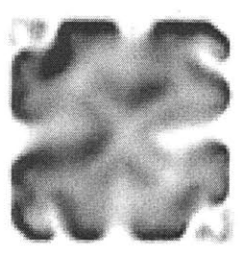
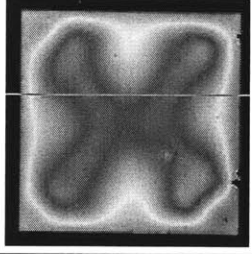
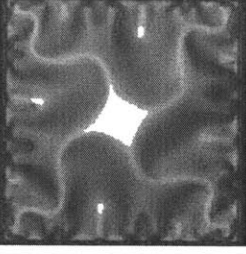
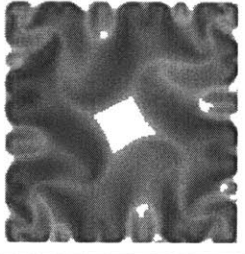
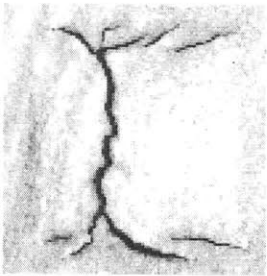
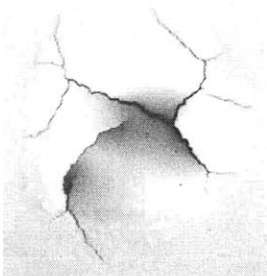
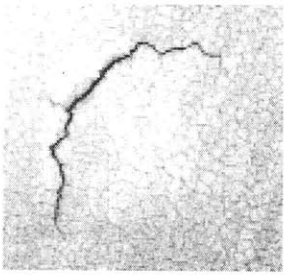
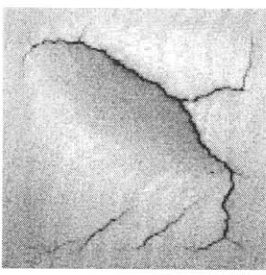
Cell Size	Before thermocycles	After 1 st heating to 625°C	After 2 nd heating to 625°C
Trilayer (~80μm)	Flat 	1 st buckling 	1 st buckling 
Trilayer (~180μm)	1 st buckling 	2 nd buckling 	2 nd buckling 

Figure 5-8: Fuel cell stack (~450-nm thick) buckling behavior under thermocycles observed with Zygo surface profiler. All images taken at room temperature.

Cell stack	After 1st heating to 625°C; Sidelength ~80μm	After 1st heating to 625°C; Sidelength ~180μm
Tri-layer		
Bi-layer		

Microcracked YSZ surface of bi-layer surface

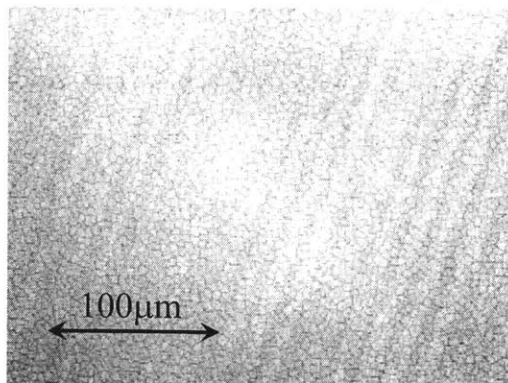


Figure 5-9: Fuel cell stack (~750-nm thick) and bi-layer (~500-nm thick) buckling behavior under thermocycles observed with Zygo surface profiler.

**Simulated Maximum and Minimum Stresses in
YSZ film ($h_f=250\text{nm}$ and 750nm) at 625°C**

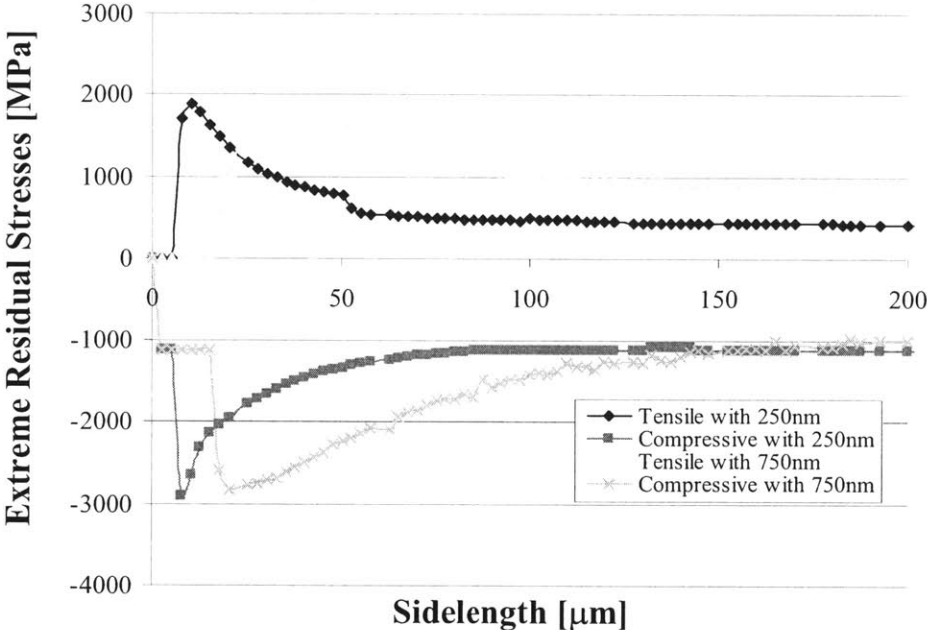


Figure 5-10: Comparison of simulated in-plane stresses with two different film thickness (250 nm and 750 nm) deposited at 500°C when annealed up to 625°C .

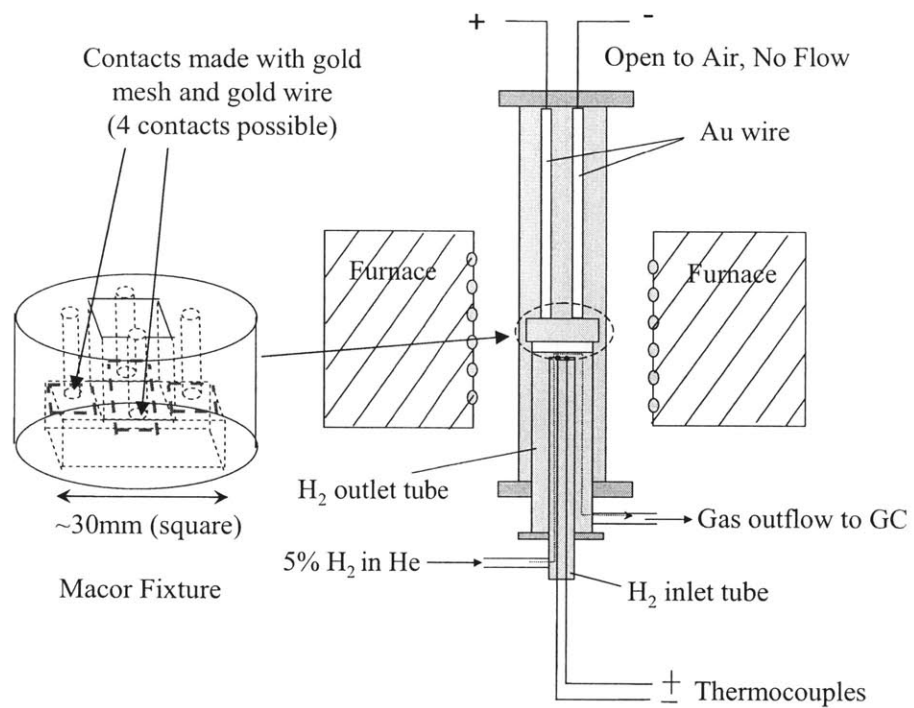


Figure 5-11: Illustration of power test fixture [6].

Nitrogen Signal in the Output Flow

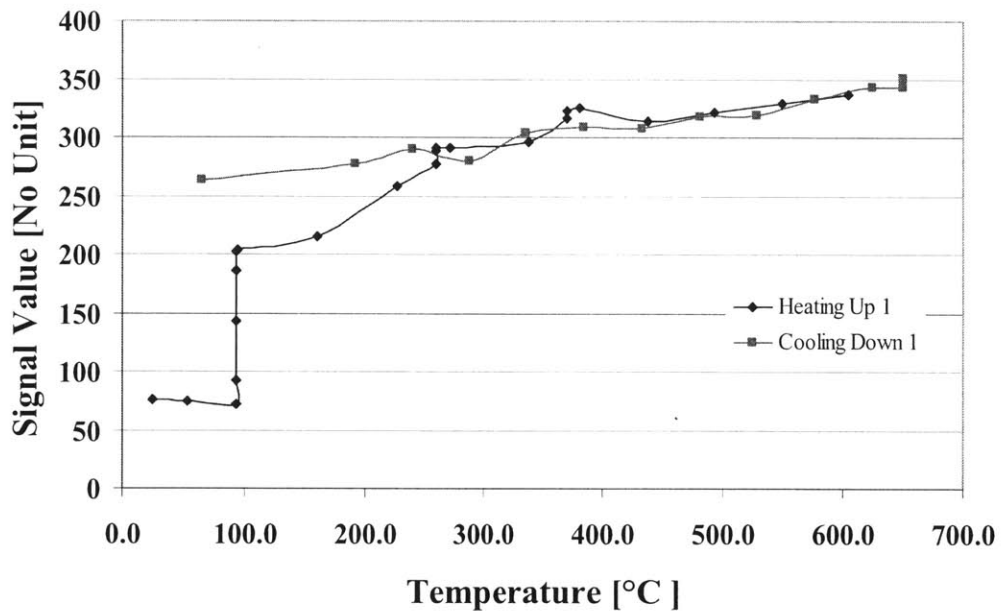


Figure 5-12: Nitrogen signal history during the first curing cycle of silica-based bonding, provided by Cui [6].

Power Test Result

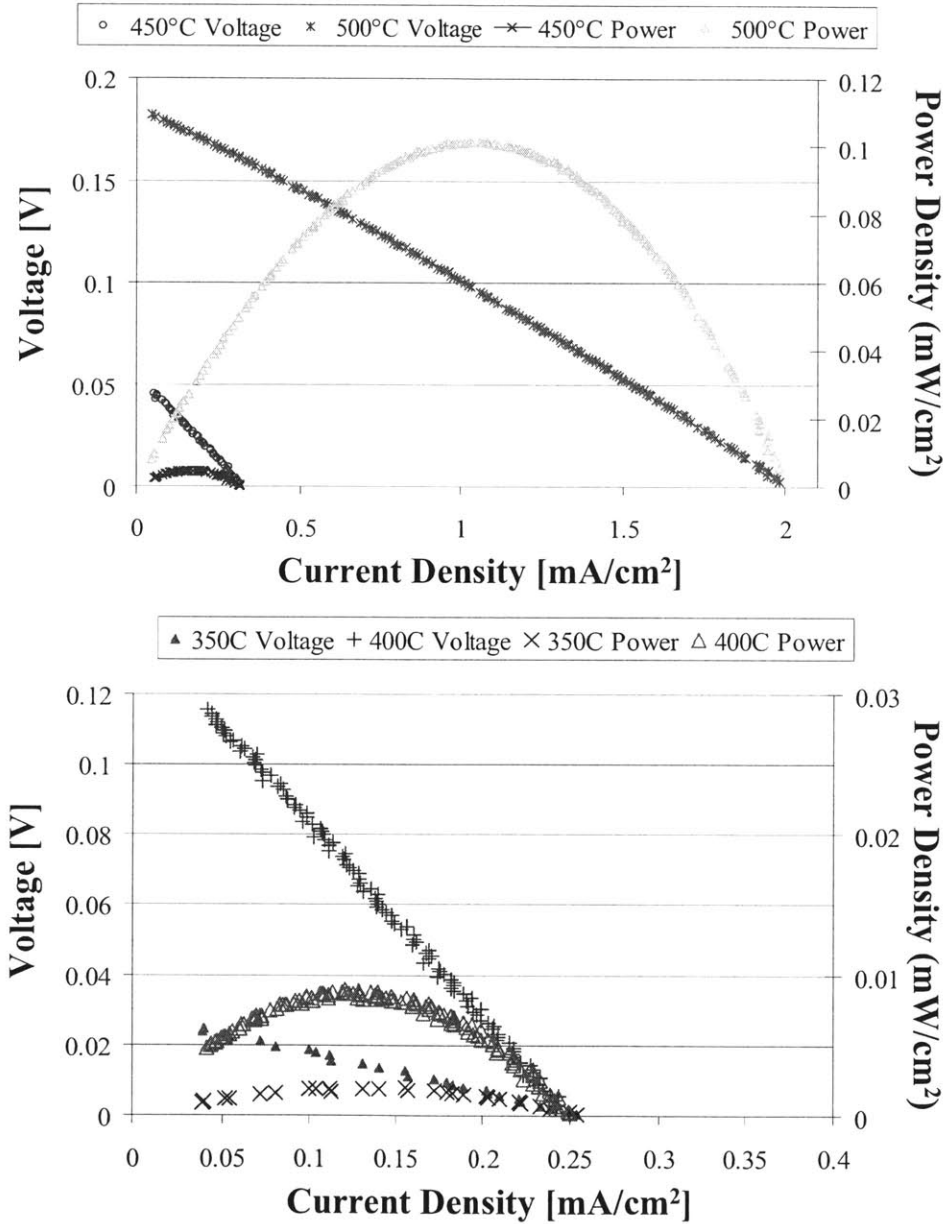


Figure 5-13: Power output from the tri-Layer (Pt-YSZ/YSZ/Pt-YSZ, each 150-nm thick) at 450°C and 500°C (*top*), and at 350°C and 400°C (*bottom*).

Nitrogen/Oxygen Signal Ratio in the Output Flow

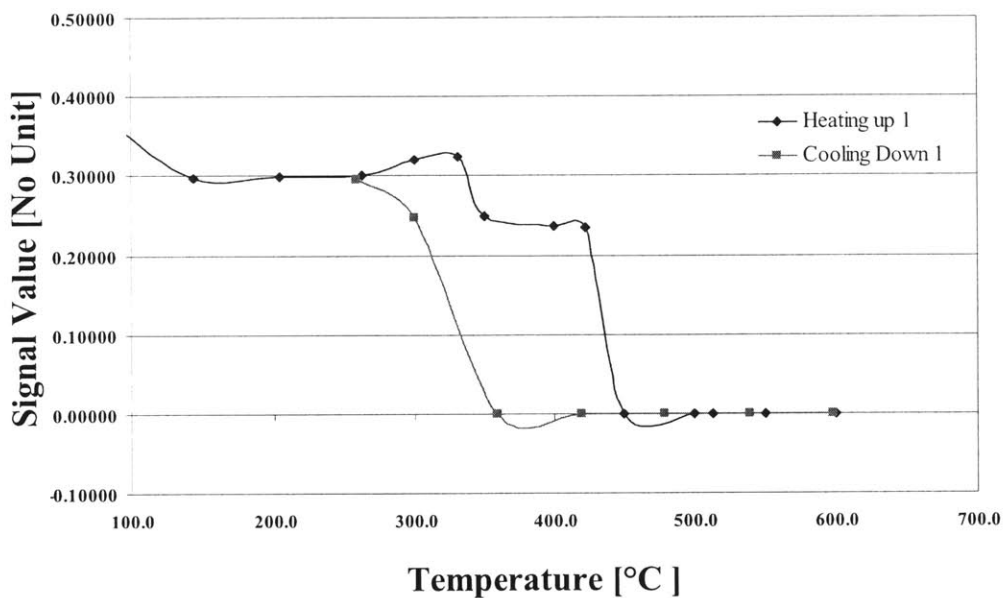


Figure 5-14: Ratio of oxygen and nitrogen signals during the thermocycle for power test.

Chapter 6

Conclusions and Recommendations for Future Work

A summary of results and contributions from this thesis work are presented in this chapter. Suggestions for future work to improve these testing results, to optimize μ SOFC structural design, and to provide tools to predict thin membrane thermomechanical stability in general will follow. Contributions from this thesis work will be listed. Their implications and the future work suggested based on the current thesis work will follow.

6.1 Summary of Results and Contributions

In this work, the following three major tasks were accomplished to achieve successful fabrication of functional μ SOFC devices. Thinning of the electrolyte (YSZ) was the key to reducing electrochemical resistance. Thermomechanical stability of this thin film structure at the SOFCs' high operation temperatures was a significant challenge. First, mechanical characterization of YSZ in thin film form was performed. The properties in micro scale are highly dependent on their fabrication methods, and thus were not known. It was critical to characterize YSZ films sputter-deposited with the recipe to be used in actual μ SOFC fabrication of our design. Sputtering conditions were designed so that deposited films have appropriate microstructure for good ionic

conductivity. Three thermomechanical properties (residual stress, biaxial modulus, and CTE) were characterized with a suitable combination of characterization methods (wafer curvature measurement, center deflection measurement of buckled square membranes, and bulge test). Second, although the modulus data had relatively large error ranges for the buckling tests, a preliminary structure for a μ SOFC was designed based on these obtained properties. Third, working μ SOFC stack membranes were fabricated with this design. Thermomechanical stability and power generation of these fabricated membranes were tested to validate functionality of the fabricated μ SOFC devices. The major contributions achieved through this thesis work are as follows:

1. Material property characterization of sputter-deposited thin YSZ films:

- A series of characterization methods (wafer curvature measurement, center height measurement of buckled square membranes, and bulge test) was selected for thin film materials, under either tensile or compressive residual stress. These three characterization methods can provide properties necessary to predict structural behavior of thin membranes under thermocycles. The test structures were simple and very similar to those of actual μ SOFC structures, and thus required no additional fabrication steps, and produced material properties in the appropriate orientation.
- Residual stresses of sputter-deposited YSZ thin films were experimentally studied by wafer curvature measurement. The films were deposited with various parameters including thickness (~ 70 – ~ 600 nm), substrate (silicon, or silicon nitride covered silicon), and deposition temperature (25°C , 500°C , and 600°C). All the wafers were thermally cycled after deposition up to 500°C .
 - Residual stresses of YSZ films deposited at room temperature increased towards tensile with increasing thickness from ~ -600 MPa compressive at ~ 70 nm until the stresses reach a plateau of ~ -100 MPa compressive near a thickness of ~ 200 nm. Post-deposition an-

nealing shifted the residual stresses towards tensile. Final residual stresses were $\sim 380\text{MPa} \pm 100\text{MPa}$ tensile regardless of thickness or substrate. These trends were explained by the compressive stress mechanism of lattice distortions (atomic peening) and tensile stress evolution mechanisms due to grain growth.

- Residual stresses of YSZ films deposited at high temperatures (500°C, and 600°C) increased towards tensile with increasing thickness from ~ -700 MPa compressive for ~ 100 nm-thick films until the stresses reach a plateau of ~ -400 MPa compressive at ~ 300 -nm thickness. The overall residual stress state was more compressive than those of films deposited at room temperature. This stress evolution with thickness and deviation from stresses of films deposited at room temperature can again be explained by compressive stress mechanism of lattice distortions (atomic peening) and tensile stress evolution mechanisms due to grain growth. Post-deposition annealing shifted the residual stresses towards tensile. Final residual stresses were $\sim -100\text{MPa} \pm 100\text{MPa}$ regardless of thickness.
- The effect of substrate on residual stresses of YSZ films was studied. YSZ films were deposited on two different substrates, silicon and silicon nitride covered silicon substrates. No significant effect was observed.
- The effect of target wear was confirmed by comparing the residual stresses of films deposited with a newer target with a flatter surface in this work and those of films deposited with an old target with a worn-out surface studied by Quinn [1]. The stress state in this work was more compressive by $\sim 300\text{MPa}$ because the flatter target, and a new holder for wafers with 150-mm diameter, reduced the working distance, and thus decreased the number of collisions between sputtered atoms, allowing them to retain compressive energy.
- "Modulus-CTE" products (see section 4.3) of YSZ were obtained by mea-

suring curvatures of thermocycled YSZ films on silicon substrates. Effects of deposition temperatures (25°C, 500°C, and 600°C) and substrates (silicon, silicon nitride covered silicon) were examined.

- The effect of temperature on the modulus-CTE product was studied. Films deposited at high temperature gave larger products (−0.8~−1.2 MPa/°C) due to more crystalline phase developed than films deposited at room temperature (−0.4~−0.5 MPa/°C).
 - The effect of substrate on modulus-CTE products was studied. Films deposited on single crystalline silicon gave larger products (−0.5 MPa/°C) than films deposited on amorphous silicon nitride covered on silicon (−0.3 MPa/°C). Microstructural orientation is the most likely cause of this difference, but was not confirmed with XRD.
 - The measured modulus-CTE products (−0.3~−1.2 MPa/°C) were significantly lower than the products calculated for bulk YSZ (~−1.9 MPa/°C). This difference was attributed to an amorphous phase in the microstructure and columnar grains.
- Young’s moduli of YSZ films with slightly compressive stress were obtained by center height measurement of buckled square membranes. Two films of ~600-nm thick were deposited at 500°C on two different substrates (silicon and silicon nitride covered silicon). One film was deposited at room temperature on silicon nitride covered silicon. Appropriate data selection performed for better data interpretation. Large error ranges were calculated which can be somewhat overcome with large data sets generated via microfabrication.
 - The deposition temperature effect on Young’s moduli obtained from square buckling test was studied. Films deposited at high temperature exhibited higher moduli (65–105 GPa) than films deposited at room temperature (24 GPa), which was attributed to increasing crystallography in the films deposited at high temperature.

- The substrate effect on Young’s moduli obtained from square buckling test was studied. Films deposited on single crystal silicon exhibited higher modulus (105 GPa) than films deposited on amorphous silicon nitride covered silicon (65 GPa). Microstructural orientation is the most likely cause of this difference, but was again not confirmed with XRD.
- CTEs were estimated from the ”modulus-CTE” product obtained from wafer curvature measurement and Young’s moduli obtained from square buckling tests. The CTEs were relatively constant as 9.8 to $11.4 \times 10^{-6}/^{\circ}\text{C}$ regardless of deposition conditions.
- Young’s modulus of YSZ films with tensile stress was studied with bulge test. The film (125-nm) was deposited at room temperature, and the obtained Young’s modulus was 168 GPa. Although this value is much higher than the square buckling test results (24 GPa), the result indicates lower Young’s modulus compared to the bulk modulus. However, this result is also a single data point with significant error that needs further testing for corroboration.

2. Design and Fabrication of μ SOFC samples:

- In-plane stresses of YSZ films were estimated with energy minimization method based on displacements calculated using von Karman plate non-linear theory. The extreme stresses (compressive and tensile) were particularly obtained for a failure criterion. The material properties of films deposited at high temperature, and film thickness of 150 nm and 250 nm, were used in the analysis. Over the sidelength of $0.5\text{--}200 \mu\text{m}$ for a constant applied temperature change of 600°C , the stresses showed three regions: a regime before buckling with only compressive stresses, a regime just after buckling with high extreme stresses (~ 2 GPa for tensile, ~ -3 GPa for compressive), and a regime after buckling with stresses relieved by out-of-plane displacements (~ 500 MPa).

- Geometrical configuration of membranes was determined based on the material properties and in-plane stress estimations obtained from above. The YSZ film thickness (150 nm and 250 nm) and sidelength (100 μm and 200 μm) were set to avoid high in-plane stresses. Deposition condition was at high temperature on silicon nitride covered substrate so that fabricated membranes have suitable crystalline structure for high ionic conductivity and so that membranes can be released through silicon nitride patterns.
- The fabricated tri-layer fuel cell membranes were thermocycled up to $>600^\circ\text{C}$. Thinner tri-layer and bi-layer membranes with 150-nm thick electrolyte buckled but survived thermocycles, while thicker tri-layer and bi-layer membranes with 250-nm thick electrolyte cracked and structurally failed. The resultant high in-plane stress in the thicker film (750 nm total thickness) was validated by additional stress estimation using nonlinear plate theory.
- Shorting between the cathode and anode layers was solved by decreasing the top Pt-YSZ layer areas. Shorting was mainly due to asperities in the film deposited on a surface contaminated with dust in the non-cleanroom sputtering facility. The top Pt-YSZ shorts with the bottom through the asperities. Experimentally, probability of shortage was confirmed to decrease with decreasing top Pt-YSZ areas.

3. μSOFC Testing

- Power produced by the designed die was estimated by electrochemical test by Hertz [101]. The area specific resistances were measured to decrease with increasing temperature ($1 \Omega/\text{cm}^2$ at 608°C), and the power was estimated as $0.25 \text{ W}/\text{cm}^2$.
- Power production of the fabricated tri-layer samples was tested. An existing experimental set-up that can control fuel gas flows, voltage across the tri-layer, and temperature was utilized. The preliminary result confirmed

power production of the designed thin tri-layer fuel cell stack, but the obtained power was much lower ($0.005\text{--}0.1\text{ mW/cm}^2$) than the estimated power based on the electrochemical test (0.25 W/cm^2). This low power production was attributed to low fuel supply, gas leakage, electric leakage, or membrane blocking by silicon nitride, Ti, or other layer residues, but none have been confirmed.

6.2 Implications

The experimental portion of this thesis work suggested some facts about thin film characteristics and their possible contribution to design of thermomechanically stable thin membranes.

First, stiffness properties of thin films were clearly dependent on fabrication processes. Thus, characterization of films with respect to each fabrication condition is critical to obtain accurate properties. Second, thin and dense films of YSZ can be obtained with sputtering down to $\sim 80\text{-nm}$ thickness with low in-plane stiffness. Thin, compliant membranes easily buckle and relieve in-plane stresses with out-of-plane deflections. Considering that the buckled membranes were experimentally confirmed to be thermomechanically stable under thermocycles up to high temperature (625°C), the post-buckling regime, which was eliminated in the design process before, can now be considered in the design space so that larger-area membranes can be fabricated. Third, related to this, further optimization of μSOFC membrane structure should be very feasible with more accurate material property extraction. In this thesis work, properties were estimated but have large error ranges, and the in-plane stress analysis calculation from the plate buckling used limited trial displacement functions. Yet, preliminary μSOFC membranes designed based on these studies were confirmed to be structurally stable and electrochemically functional. With more accurate properties and stress analysis, further optimization or expansion of design parameters (larger area, smaller thickness, and different shapes) should be fairly practical.

6.3 Recommendations for Future Work

As this thesis work progressed, several aspects were observed for improvement in terms of experimental procedures or design criteria. These points are listed in the following.

1. Material property characterization:

- Increase film thickness uniformity by decreasing wafer size or by adjusting working distance in the sputtering chamber. Thickness uniformity is critical to extract precise and accurate material properties.
- Improve fabrication processes to reduce asperities across one wafer and to prevent membrane failure during handling.
- Obtain material properties of Pt-YSZ (cathode/anode material), and yielding or failure stresses both in tension and compression of YSZ and Pt-YSZ layers to optimize μ SOFCs' tri-layer structural design.
- Establish bulge test setup using Zygo profilometer that can detect smaller deflection and thus does not require large-area released membranes. With smaller areas, fabrication and testing of single-layer membranes (without supporting layer) will be possible, which improves the accuracy.

2. Design of μ SOFC membranes:

- Expand the in-plane stress analysis from the current one-layer structure to the tri-layer structure based on material properties of YSZ and Pt-YSZ for better prediction of μ SOFC structural behavior.
- Improve the accuracy of the in-plane stress analysis with more deflection trial functions. Perform finite element analyses to validate the results by the energy minimization method.
- Optimize thin membrane structural design that are thermomechanically stable with smaller thickness for ionic conductivity and with larger area for more power output.

3. μ SOFC test:

- Identify the source of electric leakage and gas leakage in the test setup. Modify the current setup or build another setup to solve these problems.
- Modify the gas flow conditions to supply sufficient fuels to working membranes during power generation tests.
- Add more pre-test checks to confirm the functionality of the test sample and the setup (such as electric connection check or impedance check) before the power test run.
- Run more power tests on μ SOFC devices to well characterize their power production ability as a function of temperature, and to asses their life.

This thesis work has provided a preliminary set of material properties for YSZ sputter-deposited in thin film form. Based on these material properties, stacks of working YSZ electrolyte sandwiched by cathode and anode (Pt-YSZ) layers was designed, fabricated, and tested to be structurally and electrochemically functional at high operation temperature. These contributions are an excellent starting point for structural design of a variety of stable fuel cells and other thin film devices. Further optimization of the μ SOFC structural design for better efficiency and ionic conductivity is now feasible based on the contributions from this work.

Bibliography

- [1] D. J. Quinn. Microstructure, Residual Stress, and Mechanical Properties of Thin Film Materials for a Microfabricated Solid Oxide Fuel Cell. Master's thesis, Department of Mechanical Engineering, Massachusetts Institute of Technology, 2006.
- [2] C. V. Thompson. Structure Development in Thin Films. Lecture notes in Course 3.48 at MIT, 2005.
- [3] S. M. Rossnagel. Sputter deposition for semiconductor manufacturing. *IBM Journal of Research and Development*, 43:163–179, 1999.
- [4] Tencor FLX 2320 User Manual.
- [5] Y. Xiang, X. Chen, and J. J. Vlassak. Plane-strain bulge test for thin films. *Journal of Materials Research*, 20:2360–2370, 2005.
- [6] J. Cui. Personal Communications, 2005.
- [7] M. F. Ashby. *Materials Selection in Mechanical Design*. Oxford, 1999.
- [8] Y. Okada and Y. Tokumaru. Precise determination of lattice parameter and thermal expansion coefficient of silicon between 300 and 1500 K. *Journal of Applied Physics*, 56(2):314–320, 1984.
- [9] W. A. Brantley. Calculated elastic constants for stress problems associated with semiconductor devices. *Journal of Applied Physics*, 44:534–535, 1973.
- [10] R. Roberts. *The Primary Battery*, chapter 7. Wiley, 1971.

- [11] A. J. Appleby and F.R. Foulkes. *Fuel Cell Handbook*. Krieger Publishing Company, 1993.
- [12] B. Sorensen. *Hydrogen and Fuel Cells:Emerging Technologies and Applications*. Elsevier Academic Press, 2005.
- [13] S.Singhal and K. Kendall. *High Temperature Solid Oxide Fuel Cells: Fundamentals, Design and Applications*. Elsevier, 2003.
- [14] V. T. Srikar, K. T. Turner, T. Y. A. Ie, and M. S. Spearing. Structural design considerations for micromachined solid-oxid fuel cells. *Journal of Power Sources*, 125:62–69, 2004.
- [15] B. C. H. Steele and A. Heinzl. Materials for fuel-cell technologies. *Nature*, 414:345–352, 2001.
- [16] C. D. Baertsch, K. F. Jensen, J. L. Hertz, H. L. Tuller, S. T. Vengallatore, S. M. Spearing, and M. A. Schmidt. Fabrication and structural characterization of self-supporting electrolyte membranes for a micro solid-oxide fuel cell. *Journal of Materials Research*, 19(9):2604–2615, 2004.
- [17] V. T. Srikar and S. M. Spearing. A critical review of microscale mechanical testing methods used in the design of microelectromechanical systmes. *Experimental Mechanics*, 43(3):238–247, 2003.
- [18] X. Zhang, K. S.Chen, and S. M. Spearing. Residual stress and fracture of thick dielectric films for power MEMS applications. *Proceedings of the Fifteenth IEEE International Conference on Micro Electro Mechanical Systems(MEMS)*, pages 164–167, 2002.
- [19] W. N. Sharpe Jr., K. T. Turner, and R. L. Edwards. Tensile testing of polysilicon. *Experimental Mechanics*, 39(3):162–170, 1999.
- [20] M. A. Haque and M. T. A. Saif. In-situ tensile testing of nano-scale specimens in SEM and TEM. *Experimental Mechanics*, 42(1):123–128, 2002.

- [21] L. M. Zhang, D. Uttamchandani, B. Culshaw, and P. Dobson. Measurement of Young's modulus and internal stress in silicon microresonators using a resonant frequency technique. *Measurement Science and Technology*, 1(12):1343–1346, 1990.
- [22] R. Saha and W. D. Nix. Effects of the substrate on the determination of thin film mechanical properties by nanoindentation. *Acta Materialia*, 50:2338, 2002.
- [23] L. Lin, A. P. Pisano, and R. T. Howe. A micro strain gauge with mechanical amplifier. *Journal of Microelectromechanical Systems*, 6(4):313–321, 1997.
- [24] B. L. Wardle. Mechanical Characterization of Materials for MEMS. Lecture notes in Course 3.48 at MIT, 2005.
- [25] C. Friesen and C. V. Thompson. Reversible Stress Relaxation during Precoalescence Interruptions of Volmer-Weber Thin Film Growth. *Physical Review Letters*, 89(12):126103, 2002.
- [26] C. Friesen and C. V. Thompson. Correlation of Stress and Atomic-Scale Surface Roughness Evolution during Intermittent Homoepitaxial Growth of (111)-Oriented Ag and Cu. *Physical Review Letters*, 93(5):056104, 2004.
- [27] Z. Q. Ji, J. A. Haynes, E. Voelkl, and J. M. Rigsbee. Phase formation and stability in reactively sputter deposited yttria-stabilized zirconia coatings. *Journal of the American Ceramic Society*, 84(5):929–936, 2001.
- [28] E. C. Subbarao. *Advances in Ceramics*, volume 3, chapter Zirconia An Overview, page 124. American Ceramic Society, 1981.
- [29] P. Gao, L. J. Meng, M. P. dos Santos, V. Teixeira, and M. Andritschky. Study of $\text{ZrO}_2\text{Y}_2\text{O}_3$ films prepared by RF magnetron reactive sputtering. *Thin Solid Films*, 377-378:32–36, 2000.
- [30] B. Y. Liaw, R. E. Rocheleau, and Q. H. Gao. Thin-film yttria-stabilized tetragonal zirconia. *Solid State Ionics*, 92(1-2):85–89, 1996.

- [31] D. E. Ruddell, B. R. Stoner, and J. Y. Thompson. The effect of deposition parameters on the properties of yttria-stabilized zirconia thin films. *Thin Solid Films*, 445(1):14–19, 2003.
- [32] J. Will, A. Mitterdorfer, C. Kleinogel, D. Perednis, and L. J. Gauckler. Fabrication of thin electrolytes for second-generation solid oxide fuel cells. *Solid State Ionics*, 131(1-2):79–96, 2000.
- [33] R. W. Knoll and E. R. Bradley. Correlation between the stress and microstructure in bias-sputtered $\text{ZrO}_2\text{-Y}_2\text{O}_3$ films. *Thin Solid Films*, 117(3):201–210, 1984.
- [34] D. E. Ruddell, B. R. Stoner, and J. Y. Thompson. Effect of deposition interruption and substrate bias on the structure of sputter-deposited yttria-stabilized zirconia thin films. *Journal of Vacuum Science and Technology A*, 20(5):1744–1748, 2002.
- [35] Z. Q. Ji and J.M. Rigsbee. Growth of tetragonal zirconia coatings by reactive sputter deposition. *Journal of the American Ceramic Society*, 84(12):2841–2844, 2001.
- [36] W. T. Pawlewicz and D. D. Hays. Microstructure control for sputter-deposited ZrO_2 , ZrO_2CaO and $\text{ZrO}_2\text{Y}_2\text{O}_3$. *Thin Solid Films*, 94(1):31–45, 1982.
- [37] R. W. Knoll and E. R. Bradley. Microstructure and phase composition of sputter-deposited zirconia-yttria films. *Materials Research Society symposium Proceedings*, 30:235–243, 1984.
- [38] R. C. Garvie, R. H. Hannink, and R. T. Pascoe. Ceramic steel? *Nature*, 258(5537):703–704, 1975.
- [39] R. C. Garvie. Stabilization of the tetragonal structure in zirconia microcrystals. *Journal of Physical Chemistry*, 82(2):218 – 224, 1978.
- [40] H. Windischmann. Intrinsic stress in sputter-deposited thin films. *Critical Reviews in Solid State and Materials Science*, 17:547, 1992.

- [41] L. B. Freund and S. Suresh. *Thin Film Materials : Stress, Defect Formation, and Surface Evolution*. Cambridge University Press, 2003.
- [42] D. W. Hoffman. Perspective on stresses in magnetron-sputtered thin films. *Journal of Vacuum Science and Technology A*, 12(4):953–961, 1994.
- [43] M. F. Doerner and W. Nix. Stresses and deformation processes in thin films on substrates. *Critical Reviews in Solid State and Materials Science*, 14(13):225–268, 1988.
- [44] F. A. Doljack and R. W. Hoffman. The origins of stress in thin nickel films. *Thin Solid Films*, 12(1):71–74, 1972.
- [45] W. D. Nix and B. M. Clemens. Crystallite coalescence: a mechanism for intrinsic tensile stresses in thin films. *Journal of Materials Research*, 14(8):3467–3473, 1999.
- [46] L. B. Freund and E. Chason. Model for stress generated upon contact of neighboring islands on the surface of a substrate. *Journal of Applied Physics*, 89(9):4866–4873, May 2001.
- [47] P. Chaudhari. Grain growth and stress relief in thin films. *Journal of Vacuum Science and Technology*, 9(1):520–522, 1972.
- [48] C. V. Thompson and R. Carel. Stress and grain growth in thin films. *Journal of the Mechanics and Physics of Solids*, 44(5):657–673, May 1996.
- [49] R. Abermann, R. Kramer and J. Mäser. Structure and internal stress in ultra-thin silver films deposited on MgF_2 and SiO substrates. *Thin Solid Films*, 52(2):215–229, 1978.
- [50] R. C. Cammarata, T. M. Trimble, and D. J. Srolovitz. Surface stress model for intrinsic stresses in thin films. *Journal of Materials Research*, 15(11):2468–2474, 2000.

- [51] J. A. Floro, S. J. Hearne, J. A. Hunter, P. Kotula, E. Chason, S. C. Seel, and C. V. Thompson. The dynamic competition between stress generation and relaxation mechanisms during coalescence of Volmer-Weber thin films. *Journal of Applied Physics*, 89(9):4886–4897, May 2001.
- [52] J. A. Floro, E. Chason, R. C. Cammarata, and D. J. Srolovitz. Physical origins of intrinsic stresses in Volmer-Weber thin films. *MRS Bulletin*, 27(1), 2002.
- [53] J. A. Thornton, J. Tabock, and D. W. Hoffman. Internal stresses in metallic films deposited by cylindrical magnetron sputtering. *Thin Solid Films*, 64(1):111–119, 1979.
- [54] T. J. Chung, H. Song, G. H. Kim, and D. Y. Kim. Microstructure and phase stability of yttria-doped tetragonal zirconia polycrystals heat treated in nitrogen atmosphere. *Journal of the American Ceramic Society*, 80(10):2607–2612, 1997.
- [55] M. Härtling, T.P. Ntsoane, and R. Bucher. Influence of annealing on the residual stress in sputter-deposited platinum films. *Advanced Engineering Materials*, 4(8):607–609, 2002.
- [56] Y. Estrin, G. Gottstein, E. Rabkin, and L. S. Shvindlerman. Grain growth in thin metallic films. *Acta Materialia*, 49(4):673–681, 2001.
- [57] W. N. Sharpe Jr., K. M. Jackson, K. J. Hemker, and Z. Xie. Effect of specimen size on Young’s modulus and fracture strength of polysilicon. *Journal of Microelectromechanical Systems*, 10(3):317–326, 2001.
- [58] R. P. Ingel and D. Lewis. Lattice parameters and density for Y_2O_3 -stabilized ZrO_2 . *Journal of the American Ceramic Society*, 69(4):325–332, 1986.
- [59] R. P. Ingel and D. Lewis. Errors in elastic constant measurements in single crystals. *Journal of the American Ceramic Society*, 71(4):265–271, 1988.
- [60] M. Kandil, J. D. Greiner, and J. F. Smith. Single-crystal elastic constants of yttria-stabilized zirconia in the range 20 to 700°C. *Journal of the American Ceramic Society*, 67:341–346, 1984.

- [61] J. F. Nye. *Physical Properties of Crystals*. Oxford Science Publications, 1957.
- [62] E. Arzt. Size effects in materials due to microstructural and dimensional constraints: a comparative review. *Acta Materialia*, 46(16):5611–5626, 1998.
- [63] A. Jankowski, J. P. Hayes, R. T. Graff, and J. D. Morse. Micro-fabricated thin-film fuel cells for portable power requirements. *Materials Research Society Symposium Processings*, 730, 2002.
- [64] S.d. Souza, S. J. Visco, and L. C. D. Jonghe. Thin-film solid oxide fuel cell with high performance at low-temperature. *Solid State Ionics*, 98:57–61, 1997.
- [65] J. H. Koh, Y. S. Yoo, J. W. Park, and H. C. Lim. Carbon deposition and cell performance of Ni-YSZ anode support SOFC with methane fuel. *Solid State Ionics*, 149:157–166, 2002.
- [66] X. Chen, N. J. Wu, L. Smith., and A. Ignatiev. Thin-film heterostructure solid oxide fuel cells. *Applied Physics Letters*, 84(14):2700–2702, 2004.
- [67] Z. Shao, S. M. Haile, P. Ronney J. Ahn, Z. Zhan, and S. Barnett. A thermally self-sustained micro solid-oxide fuel-cell stack with high power density. *Nature*, 435:795–798, 2005.
- [68] J. D. Morse, A. F. Jankowski, R. T. Graff, and J. P. Hayes. Novel proton exchange membrane thin-film fuel cell for microscale energy conversion. *Journal of Vacuum Science and Technology A*, 18(4):2003–2005, 2000.
- [69] Y. Tang, K. Stanley, J. Wu, D. Ghosh, and J. Zhang. Design consideration of micro thin film solid-oxide fuel cells. *Journal of Micromechanics and Micro-engineering*, 15:S185–S192, 2005.
- [70] J. Hopwood. *Handbook of Nanophase Materials*, chapter Plasma-assisted deposition, pages 141–197. Marcel Dekker Inc., 1997.
- [71] M. Madou. *Microfabrication*. Boca Raton:CRC Press, 2002.

- [72] M. Ohring. *Materials Science of Thin Films*. Academic Press, 2002.
- [73] J. Hertz. Personal Communications, 2005.
- [74] P. Nieva, H. Tada, P. Zavracky, G. Adams, I. Miaoulis, and P. Wong. Mechanical and thermophysical properties of silicon nitride thin films at high temperatures using in-situ MEMS temperature sensors. *Materials Research Society Symposium Proceedings*, 546:97–102, 1999.
- [75] V. Ziebart, O. Paul, and H. Baltes. Extraction of the coefficient of thermal expansion of thin films from buckled membranes. *Materials Research Society Symposium Proceedings*, 546:103–108, 1999.
- [76] G. G. Stoney. The tension of metallic films deposited by electrolysis. *Proceedings of the Royal Society of London. Series A*, 82:172–175, 1909.
- [77] A. J. Rosakis, R. P. Singh, Y. Tsuji, E. Kolawa, and N. R. Moore Jr. Full field measurements of curvature using coherent gradient sensing: application to thin film characterization. *Thin Solid Films*, 325:42–54, 1998.
- [78] J. W. Hutchinson and Z. Suo. Mixed mode cracking in layered materials. *Advances in Applied Mechanics*, 29:63–191, 1992.
- [79] M. W. Moon, J. M. Jensen, J. W. Hutchinson, K. H. Oh, and A. G. Evans. The characterization of telephone cord buckling of compressed thin films on substrates. *Journal of Mechanics and Physics of Solids*, 50:2355–2377, 2002.
- [80] M. D. Thouless. Combined buckling and cracking of films. *Journal of American Ceramic Society*, 76:2936–2938, 1993.
- [81] J. H. Zhang, X. G. Li, and N. B. Ming. Film orientation effects on the structural, magnetic and transport properties of LaMnO_y thin films. *Journal of Physics D: Applied Physics*, 35:1301–1304, 2002.
- [82] H. W. Kim and N. H. Kim. Influence of the substrate on the structural properties of sputter-deposited ZnO films. *Physica Status Solidi*, 201:235–238, 2004.

- [83] N. H. Kim J. H. Myung and H. W. Kim. Structural properties of sputter-deposited ZnO thin films depending on the substrate materials. *Materials Science Forum*, 475-479:1825–1828, 2005.
- [84] V. Ziebart, O. Paul, and H. Baltes. Strongly buckled square micromachined membranes. *Journal of Microelectromechanical Systems*, 8:423–432, 1999.
- [85] S. Timoshenko and J. M. Gere. *Theory of Elastic Stability*. McGraw-Hill, 1961.
- [86] MetroPro Reference Guide OMP-347G, 1992.
- [87] S. C. Mehta and D. A. Smith. Grain boundaries in nanophase materials and conventional polycrystals - are they distinct? *Materials Research Society Symposium Proceedings*, 351:337–342, 1994.
- [88] C. Wan, Y. Motohashi, and S. Harjo. Effect of Superplastic Deformation on Thermal Expansion Behavior of Tetragonal Zirconia Polycrystals. *Materials Transactions*, 44:1053–1056, 2003.
- [89] P. D. Persans and A. F. Ruppert. Thermal expansion of hydrogenated amorphous germanium thin films. *Journal of Applied Physics*, 59:271–273, 1986.
- [90] K. Takimoto, A. Fukuta, N. Yoshida, T. Itoh, and D. Nonomura. Linear thermal expansion coefficients of amorphous and microcrystalline silicon films. *Journal of Non-Crystalline Solids*, 299-302:314–317, 2002.
- [91] Z. X. Chen and P. W. McMillan. Microstructure and properties of MgO-ZnO₂-SiO₂ alkali-free glass-ceramics. *Journal of Materials Science*, 20:3428–3438, 1985.
- [92] R. Hill. The elastic behavior of a crystalline aggregate. *Proceedings of the Physical Society of London Sect. A*, 65:439–454, 1952.
- [93] N. Wicks. Personal Communications, 2004.
- [94] J. W. Beams. *Structure and Properties of Thin Films*, page 183. JohnWiley and Sons, 1959.

- [95] W. D. Nix J. J. Vlassak. A new bulge test technique for the determination of Young's modulus and Poisson's ratio of thin films. *Journal of Materials Research*, 7:3242–3249, 1992.
- [96] O. Tabata, K. Kawahata, S. Sugiyama, and I. Igarashi. Mechanical-property measurements of thin-films using load-deflection of composite-rectangular membranes. *Sensors and Actuators*, 20:135–141, 1989.
- [97] S. Timoshenko and S. Woinowsky-Kreiger. *Theory of Plates and Shells*. McGraw-Hill, 1959.
- [98] M. K. Small and W. D. Nix. Analysis of the accuracy of the bulge test in determining the mechanical properties of thin films. *Journal of Materials Research*, 7:1553, 1992.
- [99] Y. Xiang and J. J. Vlassak. Bauschinger effect in thin metal films. *Scripta Materialia*, 53:177–182, 2005.
- [100] D. J. Quinn. Personal Communications, 2005.
- [101] J. L. Hertz. *Microfabrication Methods to Improve the Kinetics of the Yttria Stabilized Zirconia Platinum Oxygen Electrode*. PhD thesis, Department of Materials Science and Engineering, Massachusetts Institute of Technology, 2006.
- [102] T. Suzuki, P. Jasinski, V. Petrovsky, H. U. Anderson, and F. Dogan. Performance of a porous electrolyte in sSingle-chamber SOFCs. *Journal of The Electrochemical Society*, 152:A527–A53, 2005.
- [103] L. G. J. d. Haart, K. Mayer, U. Stimming, and I. C. Vinke. Operation of anode-supported thin electrolyte film solid oxide fuel cells at 800°C and below. *Journal of Power Sources*, 71:302–305, 1998.
- [104] S. Weiss. Personal Communications, 2005.